

I: Solid Materials for Low Temperature Thermochemical Water Splitting

II: Structure-Property Relationships on the Zeolite Catalyzed Conversion of
Methanol to Light Olefins

Thesis by

Yashodhan Bhawe

In Partial Fulfillment of the Requirements for the

Degree of

Doctor of Philosophy

CALIFORNIA INSTITUTE OF TECHNOLOGY

Pasadena, California

2013

(Defended 14 December 2012)

© 2012

Yashodhan Bhawe

All Rights Reserved

ACKNOWLEDGEMENTS

Never has an extensive undertaking such as a PhD been completed with the sole effort of one person. *Going* through each and every person I owe gratitude to would be impractical. *To* begin with chronologically, I would like to thank my parents. *Give* me their support through the years, they did. *You* always need inspiration to embark on such an extensive effort. *Up* until I joined the lab of Prof Alex Katz at UC Berkeley and worked with Dr Andrew Solovyov, I had not had the pleasure of working in an academic lab, and they instilled the curiosity I needed to pursue a PhD. I would like to express my thanks to Prof Davis for providing funding for my work, and his knowledge and insight on the fields of zeolite synthesis and catalysis. I would also like to thank Dr Stacey Zones for tips and assistance with the organic and inorganic syntheses involved in my projects, in addition to the tips for good restaurants to try in both Los Angeles, and San Francisco. Dr Labinger for his clarification of my fundamental understanding of various aspects of my results, and Prof Flagan for his insight on various pieces of equipment and various materials. I would like to thank the lab members who helped me get started in the lab – Manuel, Heather and John McKeen for teaching me synthesis, Yuriy, and John Carpenter for teaching me how to set up flow reaction systems. I was happy to have been able to interact with Dr Liu, Dr Malek and Dr Lunn at the Dow Chemical company, and for their help in collecting some of the data presented here. I would also like to thank my current labmates who I have been involved in projects with – Bingjun, Raj and Mark. Dr Sonjong Hwang helped immensely by teaching me the finer details of MAS NMR work and labmates who were willing to listen to what I had to say – Mark, Joel, Josh and Ricardo. I also want to thank my friends for the help and entertainment over the years – Larry, Jon Zuckerman, Devin, Nick, Amy. Special thanks to Han for hearing me out and for her invaluable advice during trying times. Last but not least, all the people (both real and fictional) who made my day to day life pleasant ... Kathy,

Martha, Suresh, Karen, Ernie, the knights of the Jedi Academy, Jules Winnfield, Vincent Vega, Bullet-tooth-Tony, and so on...

ABSTRACT

This thesis describes two separate projects. The first part of the thesis involves the synthesis of materials for enabling thermochemical water splitting at temperatures below 1000°C, while the second part focuses on the structure-property relationships for the catalytic conversion of methanol-to-olefins.

In the first project, metal oxide clusters are impregnated in a silica support and tested as catalysts for the thermochemical splitting of water at temperatures below 1000°C. These supported catalysts are able to do either the oxidation or reduction half cycle, but not both. Thermodynamic analyses reveal that for most common metal / metal oxide pairs, a thermochemical water splitting cycle can not occur in two steps below 1000°C. Thus, a multi-step thermochemical cycle is developed using Mn_3O_4 and Na_2CO_3 . This new cycle can be closed at temperatures that do not exceed 850°C. Additionally, three metal spinels (Mn, Fe and Co based) are investigated with three alkali metal carbonates (Li, Na and K) for both thermochemical water splitting and thermochemical CO_2 reduction. The manganese, sodium system is found to be the optimal combination for water splitting.

The second project explores the effects that zeolite structure has on the product selectivity in the methanol-to-olefins (MTO) reaction. After first ensuring that literature results on the more common MTO catalysts could be reproduced, the effects of several zeolite structure features on product selectivity are elucidated. Structural features such as channel width and channel eccentricity, cage size (tested on the LEV, CHA and AFX frameworks) and framework composition (tested on the LEV, AEI, CHA and AFX frameworks) are explored. It is found that the product selectivity does not have a strong correlation with channel width and eccentricity. Ethylene selectivity did increase with a reduction in cage size, while propylene selectivity is a maximum with the CHA cage. The most consistent theme noted is that between the aluminosilicates (zeolites) and the

silicoaluminophosphates (SAPOs), the effect of temperature on the $C_{3=}/C_{2=}$ is the same (if the aluminosilicate shows an increase in $C_{3=}/C_{2=}$ with an increase in temperature, so does the silicoaluminophosphate, etc.).

<u>FRONT MATTER</u>	<u>iii</u>
Acknowledgements	iii
Abstract	v
Table of Contents	vii
List of Figures and Tables	xii
 <u>CHAPTER 1 OVERVIEW OF THESIS</u>	 <u>2</u>
1.1 Overall Summary	2
1.2 Materials for Thermochemical Water Splitting	2
1.3 Structure-property relations in the zeolite catalyzed conversion of methanol to light olefins	3
 <u>PART I: MATERIALS FOR LOW TEMPERATURE THERMOCHEMICAL WATER SPLITTING</u>	 <u>5</u>
 <u>CHAPTER 2 INTRODUCTION TO THERMOCHEMICAL SPLITTING OF WATER</u>	 <u>5</u>
2.1 Motivation for thermal water splitting	5
2.2 Known processes for thermochemical splitting of water	5
2.2.1 SULFUR – IODINE CYCLE & RELATED CYCLES	6
2.2.2 METAL OXIDE & MIXED METAL OXIDE CYCLES	8
2.3 Shortcomings of known cycles and objective for part (I) of thesis	9
2.4 General approach for this part of the thesis	10
2.5 Bibliography	11
 <u>CHAPTER 3 PARTICLE SIZE CHANGES AS A MEANS FOR LOWERING REDUCTION TEMPERATURE</u>	 <u>13</u>
3.1 Introduction	13
3.2 Objective	13
3.3 Synthetic strategy	14
3.4 CuO impregnated in Si-*BEA	15

3.5	FeO impregnated in Si-*BEA	20
3.6	Bibliography	21

CHAPTER 4 MIXED METAL OXIDE CLUSTERS AS A MEANS FOR LOWERING

REDUCTION TEMPERATURE 23

4.1	Objective	23
4.2	Strategies for obtaining mixed-metal oxides	24
4.3	Tests on mixed metal oxides	25
4.4	Conclusions from mixed metal oxide testing	28
4.5	Bibliography	28

CHAPTER 5 THERMODYNAMIC ANALYSIS OF 2-STEP WATER SPLITTING CYCLES 29

5.1	Objective	29
5.2	Base model for thermodynamic analysis	29
5.3	Correcting state variables for partial pressure changes	34
5.4	Conclusion	36
5.5	Bibliography	36

CHAPTER 6 MN₃O₄ BASED THERMOCHEMICAL CYCLE 38

6.1	Introduction	38
6.2	Step by step analysis of Mn ₃ O ₄ thermochemical cycle	39
6.3	Recyclability of the Mn ₃ O ₄ cycle	47
6.4	Conclusions	48
6.5	Bibliography	49

CHAPTER 7 OTHER SPINEL STRUCTURES 51

7.1	Introduction	51
7.2	Materials & Methods	52
7.3	Reaction results	54

7.4	Conclusions	70
7.5	Bibliography	70

CHAPTER 8 CONCLUSIONS FROM MATERIALS FOR THERMOCHEMICAL CYCLES 72

8.1	Conclusions from impregnated clusters	72
8.2	Conclusions from spinel structures	72
8.3	Recommendations for future work	73

PART II: STRUCTURE-PROPERTY RELATIONS FOR THE ZEOLITE CATALYZED CONVERSION OF METHANOL TO LIGHT OLEFINS 80

CHAPTER 9 INTRODUCTION TO THE METHANOL-TO-OLEFINS (MTO) REACTION

		74
9.1	Motivation for the MTO reaction	74
9.2	Zeotype materials	76
9.3	Mechanisms for the Methanol-to-Hydrocarbons reaction	80
9.4	MTH reaction testing unit	83
9.5	Commercialized Methanol-to-Hydrocarbons (MTH) catalysts	85
9.5.1	HZSM-5	86
9.5.2	HSAPO-34	93
9.6	Objectives for project & layout of this section	96
9.7	Bibliography	99

CHAPTER 10 EFFECT OF CHANNEL SIZE AND SHAPE ON MTO REACTION 102

10.1	Methods & Materials	105
10.2	Effects of channel size & channel eccentricity	107
10.3	Conclusions	110
10.4	Bibliography	110

<u>CHAPTER 11</u>	<u>EFFECT OF CAGE SIZE VARIATION</u>	<u>112</u>
11.1	Introduction	112
11.2	Materials & Methods	115
11.3	Results	116
11.4	Si/Al variation study	124
11.5	Bibliography	126
<u>CHAPTER 12</u>	<u>EFFECT OF FRAMEWORK COMPOSITION VARIATIONS</u>	<u>127</u>
12.1	Objective	127
12.2	CHA	128
12.2.1	OTHER SILICATE FORMS OF CHA	130
12.3	LEV	134
12.4	AFX	136
12.5	AEI	137
12.6	Conclusions	139
12.7	Bibliography	141
<u>CHAPTER 13</u>	<u>SUMMARY OF FRAMEWORKS STUDIED</u>	<u>143</u>
13.1	Objective	143
13.2	Summary of materials Table	144
13.3	Excerpts from study of structures	144
13.3.1	RTH	145
13.3.2	ITE-RTH	146
13.4	Summary of Reaction Data	148
13.5	Conclusion	150
13.6	Bibliography	153

<u>CHAPTER 14</u>	<u>CONCLUSIONS & FUTURE DIRECTIONS FOR STRUCTURE EFFECTS ON</u>	
<u>MTO REACTION</u>		<u>154</u>
14.1	Conclusions	154
14.2	Future Work	155

List of Figures

Figure 2-1 Process flowsheet for General Atomics sulfur-iodine cycle	7
Figure 2-2 Proposed schematic for 2-step thermochemical water splitting cycle	11
Figure 3-1 Electron micrographs of Copper (II) containing particles of various sizes. (a) Bulk CuO, (b) Copper (II) silicate, (c) CuO impregnated in Si-*BEA (by TEM)	17
Figure 3-2 Thermal reduction profiles for different particle sizes	18
Figure 3-3 Thermal reduction profile comparison over consecutive runs for (left) impregnated Cu^{2+} (left), antlerite particles(center) and bulk Cu^{2+} (right)	19
Figure 3-4 Water Oxidation Pulses on (left) Bulk Fe particles, (right) impregnated Fe particles	21
Figure 4-1 Proposed strategy to complete water splitting cycle	23
Figure 4-2 Successive thermal treatments to Fe-Cu oxide particles on Si-*BEA	25
Figure 4-3 Successive thermal reduction profiles on Ni-Cu on Si-*BEA	26
Figure 4-4 Entrained oxygen in bubbler seen in O_2 trace of water pulses	27
Figure 5-5-1 Thermodynamically feasible region for two-step thermochemical water splitting, and some cycles reported in literature.	33
Figure 5-5-2 Isentropic and Isenthalpic lines with partial pressure corrections	36
Figure 6-6-1 Overview of Mn_3O_4 based thermochemical water splitting cycle	39
Figure 6-6-2 Addition of sodium carbonate is essential for low temperature water decomposition on Mn_3O_4 . (A) Thermodynamic estimates show Na_2CO_3 enables oxidation of Mn_3O_4 by H_2O . ΔG for $\alpha\text{-NaMnO}_2$ is adopted from Azad et al. ⁷ , remainder of thermodynamic data are taken from the CRC handbook ⁸ . (B) Production of D_2 and CO_2 in the oxidation of Mn_3O_4 to form $\alpha\text{-NaMnO}_2$ by D_2O in the presence of Na_2CO_3 at 850°C	40

Figure 6-6-3 Powder X-ray diffraction patterns used to identify solids phases in hydrogen evolution steps. (i) Solid collected after the hydrogen evolution step (after step 2); (ii) solid collected after reacting Mn_3O_4 with Na_2CO_3 at 850°C (after step 1); (iii) sample from (ii) hydrolyzed in an aqueous suspension in the presence of CO_2 at 80°C for 3h; and (iv) sample from (iii) annealed 180°C in Ar for 1h.....42

Figure 6-6-4 Powder X-ray diffraction patterns used to identify intermediate phases in hydrolysis of $\alpha\text{-NaMnO}_2$. (i) Hydrolysis of $\alpha\text{-NaMnO}_2$ in an aqueous suspension at 80°C for 3h; (ii) hydrolysis of $\alpha\text{-NaMnO}_2$ in an aqueous suspension at 80°C for 3h with bubbling CO_2 and (iii) hydrolysis of $\alpha\text{-NaMnO}_2$ in water vapor and CO_2 under hydrothermal condition at 140°C for 5h.43

Figure 6-6-5 Thermal reduction of Na^+ extracted $\alpha\text{-NaMnO}_2$. (A) X-ray diffraction patterns of: (i) Na^+ extracted $\alpha\text{-NaMnO}_2$, and (i) after annealing at (ii) 180°C , (iii) 300°C , (iv) 400°C , (v) 500°C , (vi) 600°C , (vii) 700°C and (viii) 850°C in Ar for 1h. (B) Temperature programmed reaction of: (i) MnO_2 , (ii) and (iii) Na^+ extracted $\alpha\text{-NaMnO}_2$ and (iv) MnCO_345

Figure 6-6 Multiple cycles of the Mn-based thermochemical water splitting system.47

Figure 7-1 (a) Reaction of Mn_3O_4 with Li_2CO_3 (top trace), Na_2CO_3 (middle trace) and K_2CO_3 (bottom trace) in the absence of water. (b) Solids after the thermal treatment at 850°C in (a) were cooled down to 200°C , before D_2O was introduced. The samples were then subjected to a temperature ramp-and-hold treatment to 850°C in $\text{D}_2\text{O}/\text{Ar}$ (5%/95%). (i, ii) D_2 and CO_2 traces for $\text{Mn}_3\text{O}_4/\text{Li}_2\text{CO}_3$; (iii, iv) D_2 and CO_2 traces for $\text{Mn}_3\text{O}_4/\text{Na}_2\text{CO}_3$; and (v, iv) D_2 and CO_2 traces for $\text{Mn}_3\text{O}_4/\text{K}_2\text{CO}_3$55

Figure 7-2 Powder X-ray diffraction (XRD) patterns identify intermediate phases in reaction of Mn_3O_4 with alkali carbonates (molar ratio 2:3) under various conditions. (a) Mixture of Mn_3O_4 and Li_2CO_3 heated to 850°C before (bottom trace) and after (middle trace) the

introduction of water. The top trace shows the diffraction pattern of the solid recovered after hydrolyzing LiMnO_2 in an aqueous suspension at 80°C with CO_2 bubbling through for 3h. (b) Physical mixture of Mn_3O_4 and Li_2CO_3 at room temperature (bottom trace) and heated to 850°C prior (middle trace) and after (top trace) the introduction of water.55

Figure 7-3 Mass fragmentation analysis shows CO_2 is reduced to CO when reacting with Mn_3O_4 and Li_2CO_357

Figure 7-4 Reaction of Fe_3O_4 with $\text{Na}_2^{13}\text{CO}_3$ confirms reduction of $^{13}\text{CO}_2$ to ^{13}CO prior to the introduction of water.....58

Figure 7-5 Percentage of CO of the reduction products (H_2 and CO) and total amount of H_2 and CO formed when the physical mixture of $\text{Fe}_3\text{O}_4/\text{Na}_2\text{CO}_3$ (molar ratio 2:3) reacts i) at 850°C with 2% CO_2 in the carrier gas (Ar); ii) at 850°C in Ar; iii) at 750°C in Ar; and iv) at 650°C in Ar. D_2O was introduced in ii), iii) and iv) after the completion of CO_2 evolution from the decomposition of Na_2CO_3 to oxidize the remaining Fe(II) species to Fe(III) . The dashed line shows the theoretical maximum amount of H_2 and CO can be formed per mole of Mn.59

Figure 7-6 CO_2 reduction with $\text{Fe}_3\text{O}_4/\text{Na}_2^{13}\text{CO}_3$ in the presence (i), ii) and iii)) and absence (iv)) of $^{12}\text{CO}_2$ in the feed.60

Figure 7-7 Water pulse experiments show the relative concentration of CO_2 and water controls the contribution of hydrogen evolution and CO_2 reduction over Fe_3O_4 and Na_2CO_3 . The part of the data enclosed in the box is used to for the product distribution analysis.....61

Figure 7-8 Reactions of Fe_3O_4 with Li_2CO_3 and K_2CO_3 show both CO_2 reduction and hydrogen evolution.62

Figure 7-9 X-ray diffraction patterns of solids collected after reacting the physical mixture of Fe_3O_4 and alkali carbonates in the absence and presence of D_2O at 850°C	63
Figure 7-10 Powder X-ray diffraction patterns of the solid collected after reacting Co_3O_4 with Li_2CO_3 , Na_2CO_3 and K_2CO_3 at 850°C in the absence (i), iii) and v), respectively) and presence (ii), iv) and vi), respectively) of water.	64
Figure 7-11 Reaction of Co_3O_4 with Li_2CO_3 (i) and ii)), Na_2CO_3 (iii) and iv)) and K_2CO_3 (v) and vi)) during the temperature ramp and hold procedure to 850°C in Ar. vii) shows the control experiment of thermal reduction of Co_3O_4 to CoO , releasing O_2	65
Figure 7-12 Thermal reduction of a) Co_3O_4 , b) Na ion extracted Mn_2O_3 and c) Na ion extracted Fe_2O_3	66
Figure 7-13 Summary of the combinations of spinel metal oxides and alkali carbonates for hydrogen evolution reaction at 850°C	67
Figure 7-14 Summary of the combinations of spinel metal oxides and alkali carbonates for CO_2 reduction reaction at 850°C	68
Figure 7-15 Summary of alkali ion extraction from the alkali metal salts formed in the hydrogen evolution reaction in an aqueous suspension at 80°C in the presence of CO_2	69
Figure 9-1 Overall scheme of alternative conversions	75
Figure 9-2 Examples of Zeotype Frameworks, *BEA (Left) and CHA (Right) ¹⁴	77
Figure 9-3 Schematic showing framework charge and balancing cation	78
Figure 9-4 Straight Channel in MFI-type framework with tetrahedral atoms highlighted	79
Figure 9-5 Schematic mechanism for methanol-to-hydrocarbons chemistry	80
Figure 9-6 Schematic of structures that only contain channels (top) and structures that contain channels that open into cavities ¹⁴² (bottom)	82
Figure 9-7 MTO reactor piping diagram	84

Figure 9-8 Framework of H-ZSM-5, MFI ¹⁴	86
Figure 9-9 Calcination temperature profile.....	88
Figure 9-10 Reaction profile of H-ZSM-5	89
Figure 9-11 Effect of Si/Al on selectivities to light olefins	92
Figure 9-12 CHA cage in CHA framework ¹⁴	94
Figure 9-13 Fluidized bed circulation data for HSAPO-34	95
Figure 9-14 Selectivity and conversion over HSAPO-34 in packed bed reactor	96
Figure 10-1 Caricature of toluene intermediate in channels of different sizes	103
Figure 10-2 Caricature of toluene intermediate in channels of different eccentricities	104
Figure 10-3 Maximum Selectivities to ethylene and propylene plotted against channel dimensions.	109
Figure 10-4 Maximum selectivities to C ₃₌ and C ₂₌ for channels of varying eccentricity	109
Figure 11-1 Aluminosilicate CHA of varying crystal aggregate sizes	113
Figure 11-2 Cages in Zeolite framework study, dimensions obtained from IZA website	115
Figure 11-3 Powder XRD patterns from obtained zeolite materials.....	117
Figure 11-4 SEM images of the aggregates of the LEV(left panel), CHA (middle panel) and AFX (right panel).....	117
Figure 11-5 Time profiles for the MTO reaction on the LEV (A), CHA (B), and AFX (C) frameworks	119
Figure 11-6 Thermogravimetric analysis of deactivated catalysts. Mass loss under 250°C was attributed to water removal, while mass loss above 250°C was attributed to organic removal.	121
Figure 11-7 GC-MS data of occluded organic analyses of partially and completely deactivated catalysts for LEV (A), CHA (B), and AFX(C).....	123

Figure 11-8 Primary crystallite sizes as a function of crystal Si/Al for LEV and CHA. The linear fits have R^2 values of 0.98 for LEV and 0.88 for CHA	125
Figure 11-9 Ethylene and propylene selectivities for LEV, CHA and AFX for various crystal Si/Al ratios	125
Figure 12-1 Reaction data from 180 mins TOS for SSZ-13 and SAPO-34 for Ethylene (left) and Propylene (right)	128
Figure 12-2 Time profile of MTO reaction on SSZ-13	129
Figure 12-3 $C_3=C_2$ ratio for SSZ-13 and SAPO-34 at various reaction temperatures	130
Figure 12-4 Reaction profile for Ga-CHA at 350°C	132
Figure 12-5 $C_3=C_2$ ratio for Ga-CHA at various reaction temperatures	133
Figure 12-6 $C_3=C_2$ ratio for LEV at various reaction temperatures	135
Figure 12-7 $C_3=C_2$ ratio for LEV at various reaction temperatures	137
Figure 12-8 Caricature of AEI cage ¹¹	138
Figure 12-9 $C_3=C_2$ ratio for AEI at various reaction temperatures	139
Figure 13-1 Powder XRD pattern for RTH material	145
Figure 13-2 Reaction profile over RTH material at 400°C	146
Figure 13-3 Time profile of MTO reaction over SSZ-36 at 400°C	147

List of Tables

Table 5-1 Thermodynamic properties of hydrogen, oxygen and water ²	32
Table 10-1: Materials selected to study effect of channel size on the MTO reaction	106
Table 10-2 MTO Reaction data over select 1-D aluminosilicate zeolites at 400°C ..	108
Table 11-1 Reaction data from Aluminosilicate CHA of varying aggregate sizes....	114
Table 11-2 Characterization and results summary for the three materials	120

Chapter 1 Overview of Thesis

1.1 Overall Summary

This thesis is a summary of some of the work I did while in the ME Davis group at Caltech. It can most generally be classified as attempts to synthesize various materials with the objective of being able to direct chemical reactivity in a certain way. Not all the materials presented in this thesis work are truly catalytic as they do not exhibit catalytic turnovers, but rather, conduct cyclic stoichiometric reactions. As with a large body of research being conducted today, the reactions being studied can be broadly classified as having the end goal of finding alternatives to fossil fuels. However, this is where the similarities between the projects that I did ends, and this first chapter is meant to serve as a guide for how the rest of this document is laid out.

The thesis is separated into two parts. Part I details my attempts at creating materials that will split water with thermal energy as the only energy input. Part II of this thesis looks at my attempts to understand structure-property relations for the zeolite catalyzed conversion of Methanol to light olefins. In chapters 1.2 and 1.3, I will briefly summarize how each of these parts of the thesis are organized.

1.2 Materials for Thermochemical Water Splitting

Part I of the thesis looks at materials made for thermochemical water splitting. Chapter 2 provides an introduction to the field of thermochemical water splitting. It also includes a brief summary of some of the drawbacks of existing systems that have been explored in the literature to conduct this process. Two specific examples from the literature are analyzed, the sulfur-iodine cycle and a metal / metal oxide cycle.

Chapters 3 and 4 look at active nanoparticles impregnated on a hydrophilic pure silicon zeolite *BEA support. Chapter 3 provides a proof of concept of why this approach was studied

in order to tackle the problem in question in this part of the thesis. It looks at two examples of oxidation by water, and thermal reduction, and the impact that impregnation has on the minimum temperature required for these reactions. Chapter 4 then looks at combining this approach with multiple metal nanoparticles in an attempt to synthesize particles with oxygen atoms bridging multiple metal centers that would possess the reduction and oxidation properties that were an intermediate between the individual metals.

Chapter 5 then presents a thermodynamic analysis of a generic 2-step water-splitting cycle. Given that chapters 2-4 present multiple approaches that were attempted but failed, chapter 5 looks at whether the 2-step cycle is even thermodynamically feasible.

Given that chapter 5 shows why a two-step water splitting cycle is not thermodynamically feasible, chapters 6-7 then present an analysis of several thermochemical cycles that were successful in splitting water, and CO₂. The first cycle that satisfied the criteria is described in chapter 6 in thorough detail. Chapter 7 then looks at other cycles obtained through variations of the metals involved in the first cycle.

Finally, Chapter 8 concludes this part of the thesis, by looking at the main conclusions drawn from the work done thus far, and offering suggestions for directions for future research that seem promising. It looks at some of the shortcomings of the cycle presented in chapter 6, and suggests possible routes to improve this cycle.

1.3 Structure-property relations in the zeolite catalyzed conversion of methanol to light olefins

As with the first chapter of Part I of the thesis, the first chapter of this part of the thesis, chapter 9 provides an introduction to the field of methanol-to-olefins chemistry. It looks at the motivation for studying this reaction in light of the need to find replacements for fossil fuels. Then it provides a brief background of what has been done in the field, and the postulated mechanism for this reaction and some of the commercialized catalysts for this process.

There were three main studies conducted on how the methanol to olefins reaction is affected by structures in the catalyst framework. These were the effect of changing channel shape (chapter 10), effect of changing cage size (chapter 11) and effect of changing framework composition (chapter 12) respectively. Chapter 11 also provides a quick look at how changing the acid site concentration differently affects the 3 different structures studied.

Chapter 13 is a survey of the effect of ion exchange treatments on the catalytic activity of the zeolitic material. Ion exchange is a common post-synthetic treatment that is employed in order to get the catalyst into its active protonic state. This chapter looks at the effect that this treatment has on both some of the characterizations performed on the zeolites and on the catalytic activity.

While the surveys presented in chapters 10-12 provide more cohesive studies of effects of different zeolite structures on product selectivities in the methanol to olefins reaction, there was a much larger body of zeolite structures that was studied. The structures that could not be grouped into cohesive studies are presented in Chapter 14.

Finally, chapter 15 concludes this part of the thesis by summarizing the key findings from the various studies that were conducted. This chapter also provides some suggestions about future directions in the area of understanding structure-property relations.

Chapter 2 Introduction to Thermochemical Splitting of Water

2.1 Motivation for thermal water splitting

Thermochemical water splitting is the splitting of water into hydrogen and oxygen with heat as the only input energy. This process would thus allow heat energy (either waste heat or otherwise) to be captured and stored as hydrogen. Hydrogen can then be used in a multitude of ways – from an energy carrier to later be used as fuel cells, to a chemical reagent required in chemical processes. A large body of research literature has gone into hydrogen as an alternative energy carrier and ways to generate hydrogen¹⁻³. Thermochemical water splitting provides a route to utilize heat from sources of heat, ranging from high temperature heat sources like solar concentrators to low temperature heat sources like waste heat from steam turbines.

2.2 Known processes for thermochemical splitting of water

Research on thermochemical water splitting catalysts has been carried out since the 1970s. The initial paradigm was to couple water splitting plants to nuclear power stations to utilize the waste heat from these power stations to generate hydrogen^{4,5}. With the growing push for carbon neutral fuels, there is again a renewed interest in these reactions to supply hydrogen as an alternative fuel. While these reactions do not provide the most thermodynamically efficient method of generating a fuel, they rely on waste heat, making it an advantageous process.

This section of this work summarizes the cycles that have been used for thermochemical water splitting. One example each of cycles that operate at low temperature and cycles that operate at high temperature will be explored in detail before elaborating on the shortcomings of these cycles. Finally a proposed strategy as well as the goals for Part I of this thesis shall be detailed.

2.2.1 Sulfur – Iodine Cycle & related cycles

The sulfur-iodine cycle was the first cycle to demonstrate that a thermochemical water splitting cycle can be closed at low temperature. In this case, the maximum temperature required is 800°C⁶. The converting species involved in this cycle are iodine (I₂) and sulfur dioxide (SO₂). The cycle can be represented by the 3 reactions given below:

Water Splitting:	$2\text{H}_2\text{O} + \text{SO}_2 + \text{I}_2 = \text{H}_2\text{SO}_4 + 2\text{HI}$	120°C
H ₂ Evolution:	$2\text{HI} = \text{H}_2 + \text{I}_2$	450°C
O ₂ Evolution:	$\text{H}_2\text{SO}_4 = \text{H}_2\text{O} + \text{SO}_2 + 0.5\text{O}_2$	800°C
Nett	$\text{H}_2\text{O} = \text{H}_2 + 0.5\text{O}_2$	

This cycle proceeds through a 3-step process. The first step splits the water between the iodine and the sulfur dioxide. In this step, the sulfur is oxidized to sulfur dioxide, while the iodine is reduced to hydrogen iodide. In the subsequent two steps, the products of the first step are decomposed to yield hydrogen, oxygen, sulfur dioxide and iodine. This completes the cycle by regenerating the initial species and hydrogen and oxygen as the only products.

There are several challenges that need to be overcome in order to employ this cycle on a commercial scale. The chemicals involved as reaction intermediates are not only highly corrosive (such as sulfuric acid at 800°C) but also highly miscible and form complex equilibria. In a paper by Davis and Conger⁷, it was reported that the first step is carried out at lower temperatures and at higher pressures such that the reaction occurs in the liquid phase.

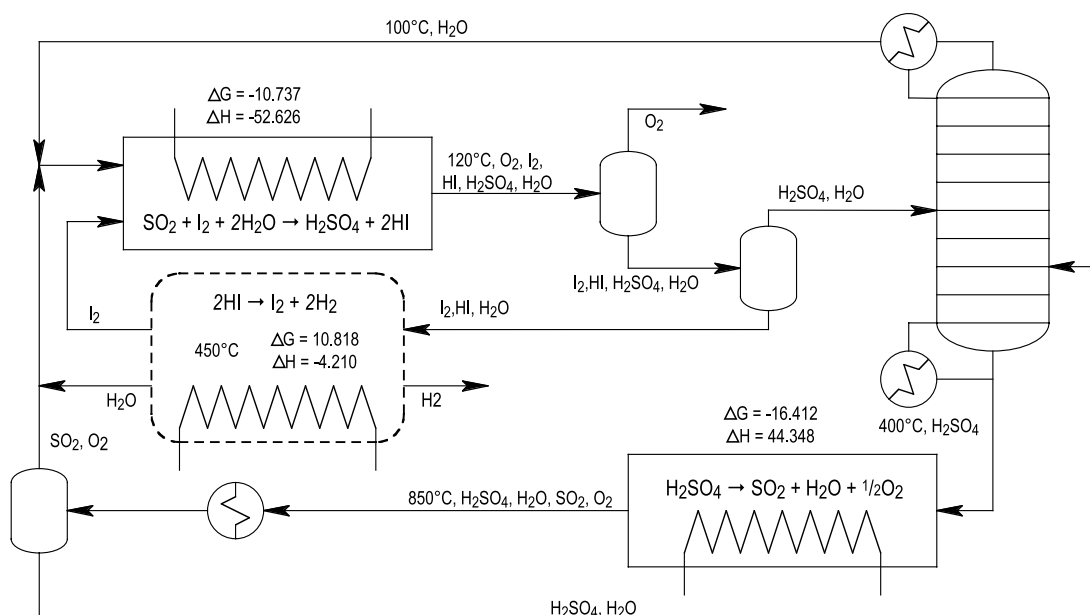


Figure 2-1 Process flowsheet for General Atomics sulfur-iodine cycle

Figure 2-1⁸ shows the process flowsheet from General Atomics for a proposed thermochemical water splitting plant to be coupled to a nuclear reactor. As seen from this setup, a lot of steps are required to separate the homogeneous mixture of HI, I₂, and sulfuric acid. The separation of the mixture requires multiple flash drums to form condensed phases as well as a distillation tower. The fact that the fluids in concern are highly acidic makes it all the more challenging for materials selection, as the reactor vessels would have to be lined with inert, thermostable coatings.

Thus, while SO₂ and I₂ do achieve splitting of water into hydrogen and oxygen below the target temperature, the industrial application of this process is made difficult by the highly corrosive homogeneous mixture after the water splitting step. This example highlights one of the main goals of this part of this work; to synthesize water-splitting materials that are largely phase separated, and non-corrosive.

2.2.2 Metal Oxide & Mixed Metal Oxide cycles

Metal oxide cycles hope to achieve this reaction by having a condensed phase metal in contact with a vapor phase containing water. This would make for easier separation as the solid phase would be retained in the reactor bed, while the excess water and the product Hydrogen and Oxygen would be in the vapor phase. There are many cycles that fall into the category⁹⁻¹², most of which proceed by the following two steps:



The first step is a thermal reduction step (that usually occurs at a higher temperature), in which heat is used to break down a metal oxide into either an oxide with a lower oxidation state, or down to the metal itself. The second step involves flushing the reduced metal (or metal oxide) with water vapor at a moderate temperature to generate the Hydrogen, and recover the original metal oxide. One example of this cycle is the Zinc / Zinc oxide cycle.

Zinc Oxide cycle

This cycle largely follows the general metal oxide cycle mechanism described above. This cycle is an example of the case where the metal oxide is thermally reduced to the metal.



In order to allow the thermal reduction of Zinc (II) Oxide to proceed at a reasonable rate, the temperature required is so high that the product zinc is in a vapor phase.^{13,14} The vapor formed presents an engineering challenge to prevent zinc precipitation in the reactor tubes.

Further, in order to achieve these high temperatures, the reaction is carried out atop a solar concentrator¹⁰. In order to handle the phase changes that occur in the thermal reduction step, a “vortex reactor” has to be used¹⁰. This is essentially a large screw conveyor with a window for focused solar radiation input. A reactor utilizing this process was set up by the group of Prof Steinfeld from ETH Zurich in a solar reactor in Spain. They were able to successfully demonstrate a water splitting cycle in this reactor, however due to the immense energy required for the moving parts of the reactor and the zinc flow path, they were only able to achieve an overall efficiency of 4%.

This system does not involve corrosive materials as the Sulfur – Iodine cycle does, however the high temperatures involved present several disadvantages. First, the high temperatures require a significant source of heat, which, to be environmentally sustainable can only come from a solar reactor. Further, the phase change of zinc during the cycle presents a huge engineering challenge in preventing condensation in unwanted regions. The high temperatures involved further present a challenge in preventing net heat (and energy) loss to the environment.

2.3 Shortcomings of known cycles and objective for part (I) of thesis

From the above two sections of this work, the shortcomings of the two types of thermal water splitting cycles are apparent. These shortcomings result in severe engineering challenges that hinder the implementation of these cycles for commercial hydrogen production. The high temperature cycles require a lower limit for the high temperature step that cannot be attained by most heat sources. For instance, apart from solar concentrators, very few heat sources would be able to provide the 1600-1800°C required for the Zn/ZnO thermochemical water splitting cycle. Similar thermal reduction temperatures are required for the other metal / metal oxide cycles. The low temperature cycles tend to form corrosive acids, and in particular acids that have

complex disproportionation chemistry. This was highlighted with the sulfur-iodine cycle in section 2.2.1.

For part (I) of this thesis, the objective was to develop thermochemical water splitting cycles that would overcome the problems described above. First, the cycle should operate entirely below 800°C. This temperature allows the utilization of heat from a large variety of waste heat sources, such as excess heat from a thermal power plant or waste heat from metal foundries. This also reduces the engineering challenges of operating at exceedingly high temperatures. Second, the materials used in thermal water splitting should not contain any corrosive species, nor should they form complex mixtures that require extensive separation post reaction. Finally, the materials used in the thermal water splitting cycle should be phase separated from the reactant and the product species, that is, solid materials employed for vapor phase conversions.

2.4 General approach for this part of the thesis

The approach for this section of the thesis is focused on studying how to reduce the energetic requirements of the metal oxide cycle by learning lessons from the multiple-step low temperature cycles. Studying the metal oxide thermochemical cycles from literature, it is apparent that the largest energy uptake lies in the thermal reduction. This is evidenced by the reaction temperatures required for thermal reduction to proceed. First, attempts to lower the temperature required for the thermal reduction will be detailed. Second, attempts will be made to try to obtain a working system where the reduction temperature has been lowered while maintaining the water reduction ability. A schematic of this reaction cycle is shown below in figure 2-2.

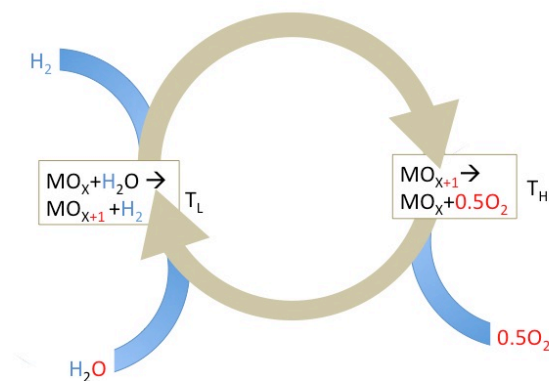


Figure 2-2 Proposed schematic for 2-step thermochemical water splitting cycle

In this schematic, the reduced and oxidized species doing the thermochemical cycle are represented by a generic species, M, for convenience. In order to achieve a complete closed cycle, this species M can either be representative of a single element, or representative of multiple elements, the bridging oxygen between them being the easily removed / added oxygen atom to complete the cycle. Ideally, a two-step cycle would be preferred as it reduces the necessity for separation of reactions and products between the various stages. However, if such a two-step cycle cannot be closed, then multiple-step cycles must be considered in order to achieve the desired cycle.

All proposed materials were tested using an Altamira AMI-200 catalyst characterization system. Effluent gases were analyzed by a Dycor Dymaxion D2000 mass spectrometer. Water was introduced by flowing inert through a water bubbler filled with either D₂O or H₂O held at 30°C. The furnace for the AMI was set up to allow thermal treatments up to 1200°C.

2.5 Bibliography

- (1) Turner, J.; et al. *International Journal of Energy Research* **2008**, 32, 379–407.
- (2) Steinfeld, A. *Solar Energy* **2005**, 78, 603–615.
- (3) Rosen, M. A. *Energy* **2010**, 35, 1068–1076.
- (4) Funk, J. E.; Reinstrom, R. M. *Industrial & Engineering Chemistry Process Design and Development* **1966**, 5, 336–342.

- (5) Funk, J. E. *International Journal of Hydrogen Energy* **1976**, *1*, 33–43.
- (6) Beghi, G. *International Journal of Hydrogen Energy* **1986**, *11*, 761–771.
- (7) Davis, M.; Conger, W. *International Journal of Hydrogen Energy* **1980**, *5*, 475–485.
- (8) Brown, L.; et al. American Nuclear Society, 555 North Kensington Avenue, La Grange Park, IL 60526 (United States): Hollywood, FL, 2002.
- (9) Abanades, S. et al. *International Journal of Hydrogen Energy* **2008**, *33*, 6021–6030.
- (10) Steinfeld, A. *International Journal of Hydrogen Energy* **2002**, *27*, 611–619.
- (11) Kasai, P.; Bishop, R. *The Journal of Physical Chemistry* **2002**, *81*, 1527–1529.
- (12) Charvin, P. et al. *Energy & Fuels* **2007**, *21*, 2919–2928.
- (13) Stamatiou, A.; Loutzenhiser, P. G.; Steinfeld, A. *Chemistry of Materials* **2010**, *22*, 851–859.
- (14) Schunk, L. O.; Steinfeld, A. *AIChE J.* **2009**, *55*, 1497–1504.

Chapter 3 Particle size changes as a means for lowering reduction temperature

3.1 Introduction

The largest obstacle in achieving the target for this part of the thesis is the high temperature required to do break down the oxidized material. One possible means to achieve this is through the lowering of particle sizes. During the reduction and oxidation of a metal or a metal oxide, one of the major components in the energy required to change the oxidation state is the energy required to change the lattice structure of the metal / metal oxide, and to move oxygen into and out of these lattice coordinates in bulk. Thus, if this lattice energy component is reduced, the energy requirement for reduction and oxidation reactions could be reduced significantly as well. One possible approach to reduce these lattice associated contributions is to reduce the size of the cluster of atoms being oxidized and reduced^{1,2}. This approach will be examined here.

3.2 Objective

The aim of this section is to study the effect of reducing cluster size on the temperature of the oxidation and reduction half cycles for a thermochemical water splitting cycle. Here temperature is being used as a proxy for the energy requirement for the oxidation / reduction half cycles. Starting with the base case of a bulk metal oxide particle, particles of smaller sizes will be synthesized to test the hypothesis, and to understand where the effects of particle size changes on the temperature required for the oxidation and reduction half cycles.

One strategy to attempt to achieve a reduced particle size is impregnating these metal oxide particles in the channels of a zeolite. Metal impregnation into zeolites has previously

been employed to reduce active metal particle sizes for hydrocarbon reactions³. A similar approach can be taken by using reducible metal oxide species. Here, as a proof of concept, particles of CuO and FeO will be synthesized as occluded species in the channels of a hydrophilic pure silica zeolite beta⁴. This material was chosen as a support because it would be inert to the redox reactions occurring at the metal active centers, while providing a size limit to the metal clusters that can form within the pores of the zeolite. The zeolite has channels that have Van der Waal's pore radii of between 5Å and 7.5Å. At most 12Å clusters can be formed at the channel intersections. These correspond to clusters with at most 6 metal atoms across in a MⁿO type metal oxide.

3.3 Synthetic strategy

Based on work by the Nørskov group, the cluster size has to be below 5Å¹ to start seeing truly dramatic changes in energies and turnover frequencies for oxygen reduction. In order to exploit this, comparisons between the bulk metal oxides and their clusters impregnated on inert supports had to be studied. In particular, impregnation into zeolite pores ensures that the metal oxide clusters are of the same sizes that would start to exhibit these dramatic changes in energies in the theoretical study. In order to allow aqueous impregnation on an inert support that had minimal diffusion limitations, hydrophilic Si-*BEA was chosen to act as a support. The *BEA zeolite framework has a 3-dimensional network of pores that are larger than 5Å, but less than 7Å.

MO_x/Si-*BEA was synthesized by post synthetic treatment on CIT-6. Fresh CIT-6 was made from the known literature recipe for CIT-6.⁵ The occluded TEA⁺ organic species were removed by calcining the as-made material to 580°C in medical grade air. Due to the harsh conditions of the calcination the framework zinc of CIT-6 is removed to form extraframework, intracrystalline ZnO clusters. These clusters must be removed from the material in order to get a clean material for the impregnation of the metal oxide. These clusters are removed through an

acetic acid extraction treatment similar to what was reported by Andy & Davis ³: 3 sequential extractions with fresh 50 mass % solutions of glacial acetic acid in water.

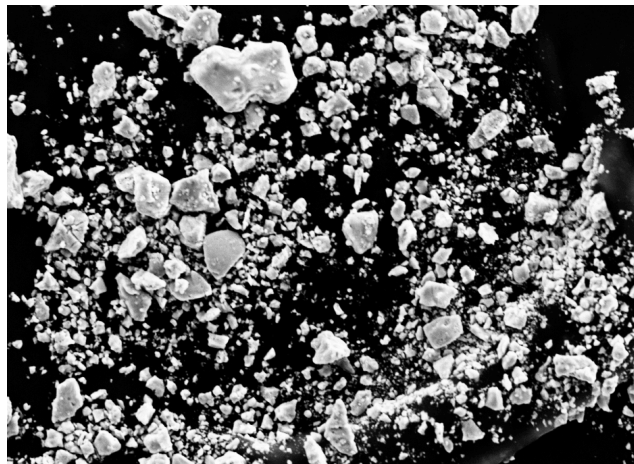
After zinc removal was confirmed by EDS, the pure Si-*BEA was impregnated by incipient wetness. Typically 10 ml of a metal nitrate solution was used per gram of zeolite. The amount of metal nitrate was calculated to yield 5 wt % of oxide upon completion of the treatment. After leaving the solution in contact with the zeolite for a period of 12h, the water was dried from the slurry by heating the slurry to 100°C. At this point, there should be clusters of metal nitrates occluded in the pores of the pure silica zeolite. In order to convert the nitrate clusters into clusters of metal oxides of the desired oxidation state, a calcination treatment under Ar was conducted. This treatment was conducted in situ in the reactor prior to the conducting reactivity tests listed below. Even though these experiments were carried out to show that independently the size reduction principle could be used for both the thermal reduction and oxidation half-cycles, the other half reaction was also tested on each of the catalysts.

3.4 CuO impregnated in Si-*BEA

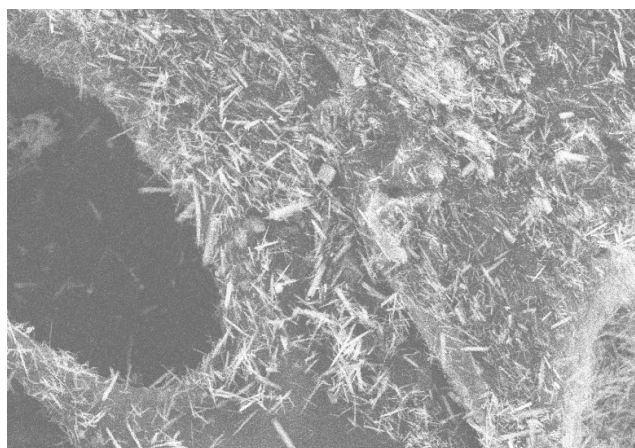
CuO was used as the metal oxide to prove that for the thermal reduction step, particle size changes affect the thermodynamics of the thermal reduction step. As the two bookends for the sizes of CuO particles synthesized, CuO on Si-*BEA (made using the synthesis protocol described above) In addition to bulk CuO and CuO impregnated on Si-*BEA, a third size of particles was also studied. These particles were synthesized by accident due to harsh exchange conditions while exchanging Cu^{2+} onto Al-*BEA. XRD characterization revealed that they were a Copper II – silicate phase known as Antlerite.

The sizes of these particles were characterized by electron microscopy. The sizes of the copper silicate and bulk copper oxide phases were determined by SEM, the size of the occluded copper species were found by TEM studies on sectioned zeolite crystals. The electron

micrographs from these analyses are shown below in figure 3-1. This set of particles span 3 orders of magnitude. However, the copper (II) silicates that are shown in figure 3-1 (b) have a very high aspect ratio, making it difficult to determine which the critical dimension is.



a) Mag = 1.43 K X 10μm EHT = 20.00 kV Signal A = SE2 Date :17 Mar 2010
WD = 13 mm Photo No. = 8636 Time :18:28:14



b) 20μm EHT = 20.00 kV Signal A = SE2 Date :19 Nov 2009
WD = 12 mm Photo No. = 4300 Time :19:12:43

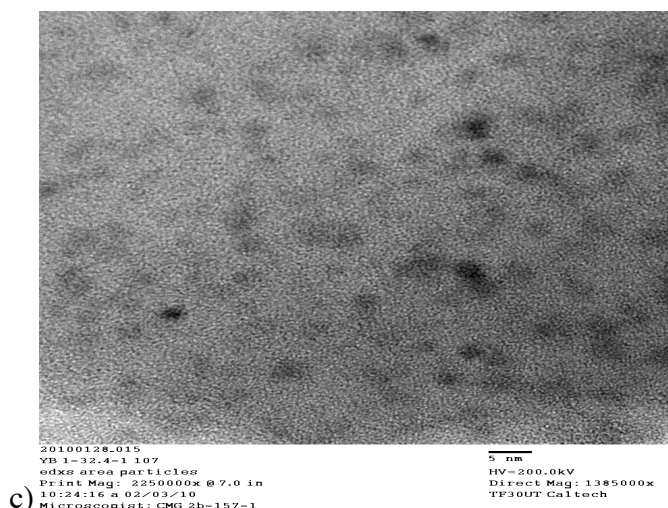


Figure 3-1 Electron micrographs of Copper (II) containing particles of various sizes. (a) Bulk CuO, (b) Copper (II) silicate, (c) CuO impregnated in Si-*BEA (by TEM)

The following procedure was followed for the thermal reduction: the reactor tube was loaded and the material was heated in Ar to 350°C at 10°C /min, and held at 350°C for 1 hour. This was all done under a 50 cm³/min gas flow. This ensured that the particles being tested were in the copper (II) oxide state. After the hold, the solid was cooled back down to 50°C. The sample was then ramped at 5°C/min under the same flow to 975°C, and then held for 1 hour at that temperature before cooling it down to 50°C.

The thermal reduction profiles are provided in figure 3-2. The reduction temperature for the bulk copper oxide is 80°C higher than the CuO impregnated zeolite beta. It is about 70°C higher than the antlerite particles. The reduction temperature decreases with decreasing particle size. Further, it is seen that the intensities for the impregnated particles are two orders of magnitude higher than the bulk particles on a per mole of copper basis.

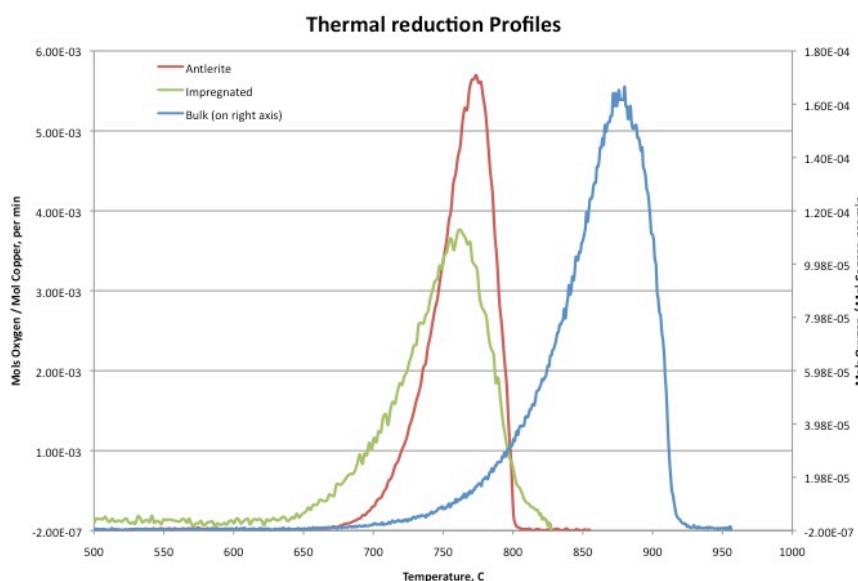


Figure 3-2 Thermal reduction profiles for different particle sizes

The thermal reduction of copper (II) oxide to copper (I) oxide should yield the same amount of oxygen per mole of copper: 0.25 mol. However, different amounts of oxygen are evolved due to incomplete oxidation-reduction within the temperature range studied. The limited temperature range would only reduce the surface species. Thus, where smaller amounts of oxygen are evolved, the energy barrier for bulk reduction has yet to be overcome. For the optimal species, the surface area would be maximized and this would present the lowest energetic barrier for reduction.

The anomaly in this result is the intensity of the antlerite particle reduction. This might be because of the shape of the formed crystals. The initial crystals formed were rod like and had a very narrow diameter. Thus, the exposed surface area may be very high. Further, the antlerite particles were likely made of very dispersed copper ions with coordinated silica and sulfate groups. This dispersion may have formed an even more reducible species than copper (ii) oxide nanoclusters.

The second observation made was the consistency of the reduction temperature over consecutive runs on the same loaded material. Over consecutive runs, it was noted that the maximum thermal reduction occurred within an error bound of 10 °C for the impregnated

particles. However, both the bulk oxide and the antlerite particles show larger changes in the thermal reduction temperature. There is an especially pronounced decrease in peak reduction temperature between the first reduction and the second reduction for the bulk material (80°C). A comparison of the reduction profiles for all 3 materials is shown in figure 3-3.

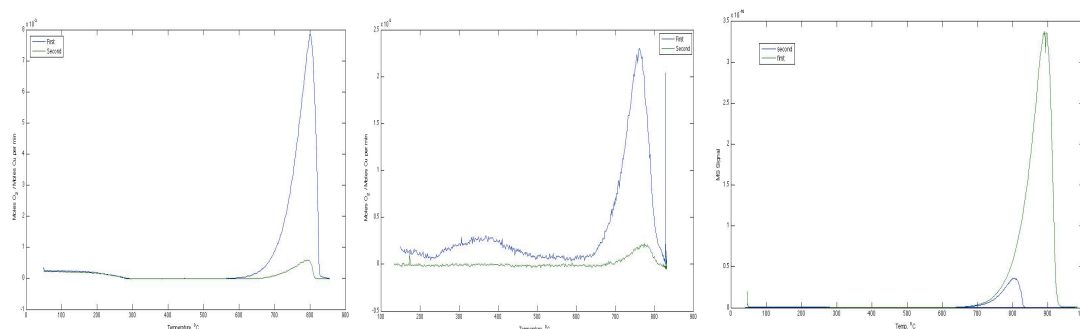


Figure 3-3 Thermal reduction profile comparison over consecutive runs for (left) impregnated Cu^{2+} (left), antlerite particles (center) and bulk Cu^{2+} (right)

Another observation from this figure is that the intensity of desorption changes over different runs. This is seen across the 3 different sized particles. While expected for the two larger particle sizes, it is not expected for the impregnated material. This is because sintering is a possibility in the antlerite particles and the bulk material due to contact between different particles. However, the particles in the impregnated material are isolated, and as such cannot move and coalesce.

Both the intensity of the desorption peak and the temperature at which this happens can be explained by the sintering of copper oxide particles. Literature evidence⁶ suggests that sintering is prominent if the temperature is raised to above 50% of the absolute melting temperature of the compound. The temperature reached during the reduction is at least 1123 K during the studies while the temperature at which sintering would become significant is 737K. Since sintering is occurring, it could be postulated that the particles go past a critical particle diameter where the reduction thermodynamics change. This phenomenon was observed in a study by Niklasson et al.⁷ They postulated that as the particles go into the nanoparticle regime,

the diffusivity into the bulk material becomes more nonlinear, speeding up the oxidation process. Though the results on the paper are for kinetic studies, an argument based on the energetic requirements of a larger crystal lattice can be made as well.

Through this series of experiments, it was shown that impregnated nanoclusters of Copper (II) Oxide inside zeolites are more active than the bulk material of the same composition. This higher activity could be used to engineer a catalyst that reacts at a lower temperature than the known heterogeneous catalysts.

3.5 FeO impregnated in Si-*BEA

FeO on Si-*BEA was prepared in a manner similar to what was described for synthesizing CuO on Si-*BEA. A solution of $\text{Fe}(\text{NO}_3)_2$ was impregnated onto a hydrophilic Si-*BEA sample that was prepared in the manner described above. However, unlike the case with Cu, for Fe, only the bulk material and the impregnated material were tested for their reaction temperature. In a very similar protocol to what was done with Cu, the impregnated material was dried, and heated to 350°C under Ar to allow decomposition of the nitrate anion to the oxide. Upon decomposition, the oxide was cooled again to 50°C to start the water oxidation experiment.

The results from water oxidation experiments are presented in figure 3-4. In both figures, the water traces on the mass spec are shown in green, the hydrogen traces are in pink. The temperature profile is in blue, and on the left axis. While the total hydrogen evolved is greatly different between the two samples, the key observation is the temperature for the first pulse where hydrogen is observed. For the impregnated material, hydrogen evolution starts as low as 130°C, while for the bulk iron particles, a temperature of 190°C is required for the hydrogen evolution to be observed.

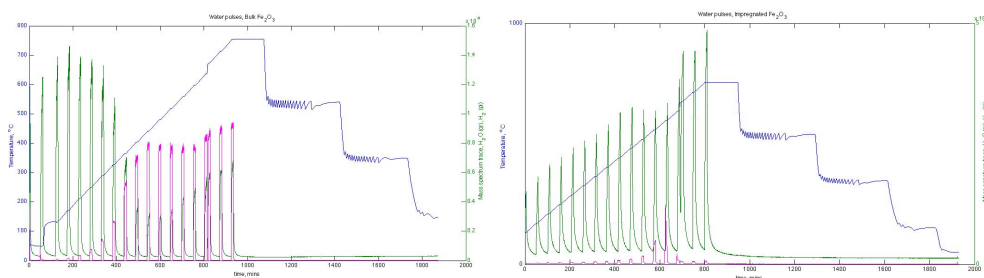


Figure 3-4 Water Oxidation Pulses on (left) Bulk Fe particles, (right) impregnated Fe particles

While this is not as significant a change as what was seen with the CuO reduction, it still serves as a second proof of concept for being able to reduce the temperature required for the oxidation state change through this technique. While both of these examples do prove the concept, they also show that this alone is insufficient in being able to complete the entire water splitting cycle.

Upon testing the copper material for water oxidation, and the iron oxide for thermal reduction, both materials were unsuccessful in doing the other half of the cycle. In order to test this, upon completion of their respective half-cycles (reduction for Cu, oxidation for Fe), the materials were cooled down to 50°C, and the other half cycle was started. For the reduced Cu species, the solid was heated under argon to the maximum temperature the reactor could sustain (1200°C) while pulsing water over the catalyst. For the oxidized Fe species, the solid was heated under argon to 1200°C again, but without water pulses. In both cases, no reaction was observed. Thus, there needs to be a combination of the size reduction strategy with other strategies in order to close the cycle under the target temperature of 1000°C.

3.6 Bibliography

- (1) Greeley, J.; et al. *Zeitschrift für Physikalische Chemie* **2007**, 221, 1209–1220.
- (2) Navrotsky, A.; Ma, C.; Lilova, K. *Science* **2010**, 330, 199-201
- (3) Andy, P.; Davis, M. *Industrial & Engineering Chemistry Research* **2004**, 43, 2922–2928.

- (4) Jones, C. W. et al. *Micropor Mesopor Mat* **2001**, 48, 57–64.
- (5) Takewaki, T.; Beck, L.; Davis, M. *Journal of Physical Chemistry B* **1999**, 103, 2674–2679.
- (6) German, R. M. *Sintering theory and practice*; 1996.
- (7) Niklasson, G.; Karmhag, R. *Surface Science* **2003**, 532, 324–327.

Chapter 4 Mixed metal oxide clusters as a means for lowering reduction temperature

4.1 Objective

The objective of this section of this work is to attempt to exploit oxygen atoms with multiple metal coordinations in addition to reduced particle size to attempt to complete a water splitting cycle under the target temperature. In the previous section of this work, reducing the particle size as a means to lower reaction temperature for the two independent half reactions was demonstrated with metal particles of two different metals, copper and iron.

The schematic of the proposed strategy is demonstrated below in figure 4-1. A summary of the previous section is shown in the first two columns, with cartoons of the structures being oxidized or reduced. The rightmost column shows one possible proposed structure for this section of the work. In it, the oxygen atoms that are bound to both iron and copper centers may have chemical behavior that is a combination of both of the oxygen atoms in the two left most structures. The intended effect is similar to atoms of gold in contact with titania in Au/TiO₂ catalysts¹.

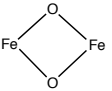
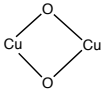
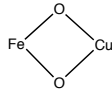
			
Water splitting	Under target temperature	Not observed under target	Possibly combine the
Thermal Reduction	Not observed under target	Under target temperature	behaviour of both Fe & Cu

Figure 4-1 Proposed strategy to complete water splitting cycle

In addition to the Iron-Copper mixed metal oxide, Nickel-Copper was also attempted. Nickel exhibited similar behavior to iron, in that it was able to split water to yield hydrogen, but it did not thermally reduce under the target temperature. In the following section, the data from tests conducted on both of these mixed metal oxides are presented.

4.2 Strategies for obtaining mixed-metal oxides

The synthesis of the single metal oxide clusters was a straightforward exercise in incipient wetness impregnation, similar to what was done previously^{2,3}. However, creating a mixed metal oxide cluster is a more challenging procedure³. This is because of the challenge of creating colocalized metal oxides of the two different metals.

Sequential impregnation of the two metals would not be a satisfactory solution because the deposition of particles of the first metal would result in pore blockage, restricting deposition of the second metal. In light of this, a mixed solution of metal acetates was chosen as the impregnation medium. The drying and activation procedure was identical to what was described in chapter 3 for the single metal clusters.

As mentioned above, it is critical that the two metal species be adjacent to one another, with shared oxygen atoms. This is analogous to the ideal way to characterize colocalization of mixed metal oxides would be through transmission electron microscopy. However, due to difficulty in processing zeolitic materials for TEM analysis, a direct chemical analysis approach was taken in trying to ascertain if the metal particles were colocalized. The samples were directly analyzed for their activity in a full cycle, and their activity was compared to separately impregnated single metal particles. In order to evaluate the mixed metal oxide for the full thermochemical cycle, as the individual metal particles would allow both halves to occur independently. Only a regeneration to the original state would prove a complete cycle can occur.

The main drawback of this approach is that a negative answer could imply a failure both in synthesis of colocalized nanoparticles or the failure of the synthesized particles to conduct the entire cycle. However, given the lack of a method to independently verify the colocalization, this was the way used to judge whether this method can be used to make

materials that can be used for thermochemical, be it due to inability to synthesize the right materials, or due to the inability of the materials to conduct the whole cycle.

4.3 Tests on mixed metal oxides

The key data from the Fe-Cu system are shown in figure 4-2, and the Ni-Cu system are shown in figure 4-3. In summary, neither of these mixed metal oxides are able to complete the two half reactions such that the cycle would be complete. The mixed metal clusters behave like independently impregnated clusters, and the hypothesis of being able to synthesize clusters where the shared oxygen atoms have properties of both the oxidizable metal and the reducible metal proved to be incorrect.

In figure 4-2, the first and second thermal treatment on Fe-Cu on Si-*BEA is shown. Between the two thermal treatments, the material was pulsed with water on a temperature ramp starting at 150°C, and reaching 1000°C. During the water splitting step, water splitting behavior analogous to what was seen in section 3.4 was observed. As seen here, the second thermal treatment under inert yielded no peaks associated with oxygen, suggesting that the water pulses did not reoxidize the species responsible for the oxygen evolution in the first thermal treatment. That is, the Fe-Cu system, synthesized this way, was incapable of completing a water splitting cycle.

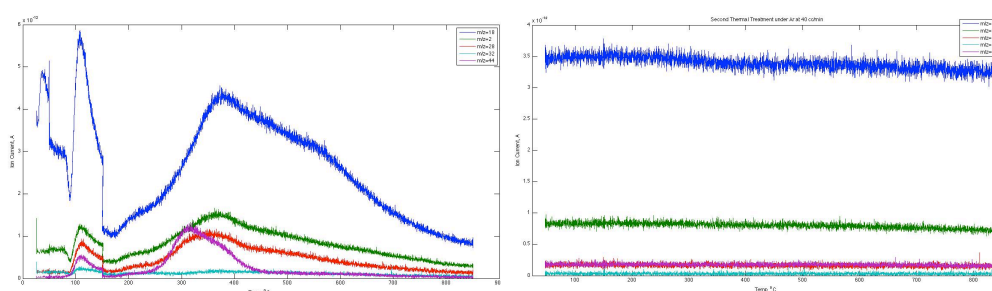


Figure 4-2 Successive thermal treatments to Fe-Cu oxide particles on Si-*BEA

Figure 4-3 shows the mass spectrometer data from the Ni-Cu particles impregnated on Si-*BEA. There are several interesting points from these successive thermal reduction profiles.

Again, as with the Fe-Cu system, between the successive thermal treatments, an oxidation treatment that involved water pulses on a temperature ramp up to 1000°C was conducted.

The first point of note is that in all 3 thermal reduction profiles, there is O₂ being evolved. Thus, it would seem that the material can be oxidized by the water pulsing treatment. Second, the temperature at which the thermal reduction occurs is shifted by 150°C between the first and the second thermal reduction. This suggests a change in the nature of the species being reduced between the first and the second thermal treatment. This is further shown by the significant reduction in the quantity of O₂ being evolved in the thermal treatment. As indicated by the units on the y-axis, there is a 10-fold reduction in the amount of oxygen being generated from the first reduction to the second reduction. However, after that, the second and third thermal reductions yield an almost identical temperature profile.

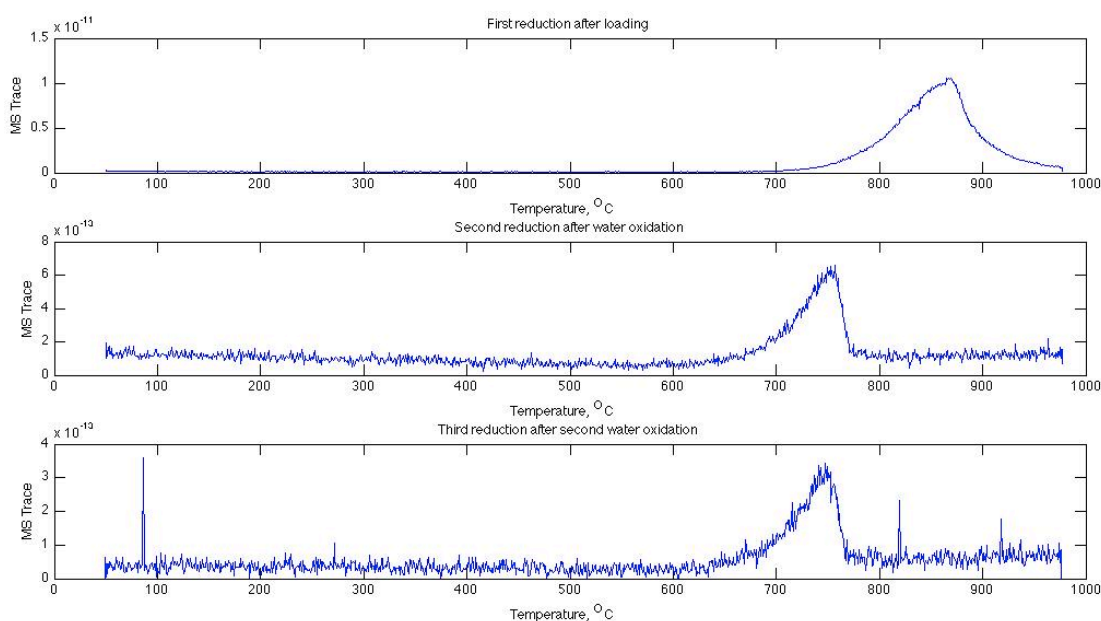


Figure 4-3 Successive thermal reduction profiles on Ni-Cu on Si-*BEA

These data, as a whole, suggest that the water splitting cycle might be completed by the Ni-Cu species impregnated in Si-*BEA. It also suggests that the oxygen in the original species (first reduction) was more tightly bound to the metal structure than the subsequent removed

oxygen. However, closer examination of the water pluses revealed negligible H_2 formation. Thus, there was a question of the source of oxygen used to oxidise the metals in order to generate reducible oxygen. Upon further evaluation of all the traces during the water pulses, it was seen that water pulse carried along with it entrained oxygen (see figure 4-4). Given that the oxygen is a stronger oxidizing agent than the water that was carried by the inert, it was hypothesized that the entrained oxygen was in fact what caused the oxidation, and the ability to “complete” the cycle shown above.

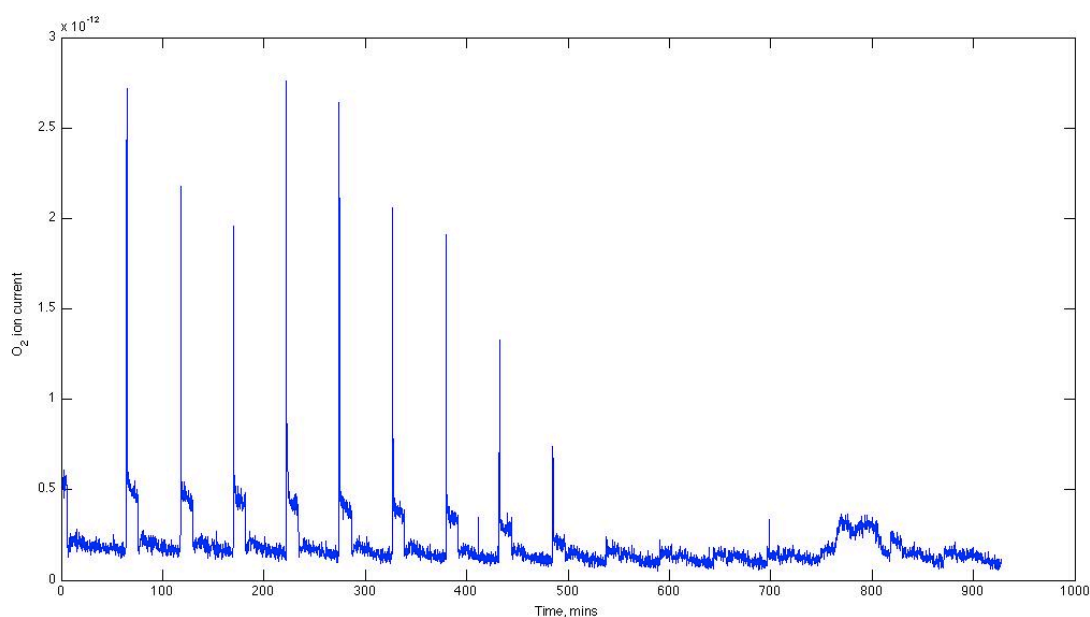


Figure 4-4 Entrained oxygen in bubbler seen in O_2 trace of water pulses

In order to confirm this, a control experiment was first conducted to quantify the amount of entrained oxygen that is evolved through the pulses. This test was conducted with no catalyst present in the reactor u-tube, and the temperature and pulse profile identical to the run shown above in 4-4. The area under the $m/z=32$ curve was integrated, and this number was compared to the integrals seen above in figure 4-4. Any unaccounted for oxygen species can be assumed to have reacted with the solid present in the reactor. The total integral of the unaccounted oxygen was 95% of the integral of the oxygen seen in the second and third

reduction runs in figure 4-3 above. Thus, the oxidation was caused not by the water splitting, as intended, but rather by the entrained oxygen.

4.4 Conclusions from mixed metal oxide testing

The data above show that the two attempts at mixed-metal oxide cycles were unsuccessful in yielding a system that was capable of completing a full thermochemical water splitting cycle. The metal particles behaved as independent oxides would. The only promising data was seen with the Ni-Cu system in the very first reduction, where the species showed a thermal reduction temperature that was slightly more elevated than the regular CuO reduction temperature.

At this point, an essentially infinite number of combinations between various transition metals can be envisioned and tested, and to test such a large combination of metals would be beyond the scope and timeline for this thesis work. Before investigating in further detail the possibility of recreating a Ni-Cu species that would give rise to the first thermal reduction peak seen in figure 4-3, or other combinations of transition metals that would yield more promise in being able to close the cycle, a thermodynamic analysis of the entire thermochemical water splitting cycle needs to be conducted.

4.5 Bibliography

- (1) Rodriguez, J. A., et al. *J Am Chem Soc* **2002**, *124*, 5242–5250.
- (2) Blomsma, E.; Martens, J. A.; Jacobs, P. A. *Journal of Catalysis* **1997**, *165*, 241–248.
- (3) Andy, P.; Davis, M. *Industrial & Engineering Chemistry Research* **2004**, *43*, 2922–2928.

Chapter 5 Thermodynamic analysis of 2-step water splitting cycles[#]

5.1 Objective

In this section of this work, a thermodynamic analysis will be conducted on an arbitrary two-step water splitting cycle to determine the conditions required of the oxidized and reduced metal species in order to be able to close the cycle under 1000°C. The analysis will be conducted by assuming that the cycle is conducted on an arbitrary metal, M. Using elementary equations for the Gibbs free energy change for the reaction, expressions involving only the material properties of the metal in question will be obtained. Upon completing the analysis under standard conditions, temperature and partial pressure corrections will be applied to bring the analysis model as close to the actual reaction conditions as possible. This is similar to what was shown by Meredig & Wolverton¹. The only caveat of this approach is that it is impossible to evaluate the drop due to the approach taken in chapters 2 and 3 of this thesis. Most of the tabulated data are available for bulk metals and metal oxides.

5.2 Base model for thermodynamic analysis

As stated above, the thermodynamic analysis is conducted on a generic metal, M, which is cycling between an oxidized state, Ox, and a reduced state, Red, where $Red + \frac{1}{2} O_2 \rightarrow Ox$, through the two-step thermochemical water splitting cycle. The chemical reactions involved, and the temperatures at which they occur are given below:



[#] Originally published in PNAS DOI: 10.1073/pnas.1206407109

For each of these reactions, the overall Gibbs free energy change was calculated by $\Delta G_{rxn} = \sum_i \Delta G_{product\ i} - \sum_i \Delta G_{reactant\ i}$. These Gibbs free energy changes were then deconvoluted into enthalpic and entropic contributions by the relationship between ΔG and ΔH , $\Delta G = \Delta H - T\Delta S$:

$$\Delta G_1^{T_1} = \Delta H_{f,Ox} + \Delta H_{f,H_2} - \Delta H_{f,Red} - \Delta H_{f,H_2O} - T_1(\Delta S_{f,Ox} + \Delta S_{f,H_2} - \Delta S_{f,red} - \Delta S_{f,H_2O}) \quad (5-3)$$

$$\Delta G_2^{T_2} = \Delta H_{f,Red} + \frac{\Delta H_{f,O_2}}{2} - \Delta H_{f,ox} - T_2\left(\Delta S_{f,Red} + \frac{\Delta S_{f,O_2}}{2} - \Delta S_{f,ox}\right) \quad (5-4)$$

In the above expressions, the enthalpy and entropy values are at the temperature that the reaction is occurring at (T_1 for reaction 5-1, and T_2 for reaction 5-2). The end goal of this analysis is to find expressions such as $(\Delta H_{f,Red}^{T_0} - \Delta H_{f,Ox}^{T_0})$, where T_0 is the standard reference temperature, 298K. These values can then be compared against tabulated values available in any number of reference texts ² to determine which of the combinations of metals would provide the most ideal mixture for completing the cycle. In order to assess the thermodynamic feasibility of a cycle, it was assumed that each reaction is equilibrated at the temperature at which it is occurring, such that $\Delta G_1 = \Delta G_2 = 0$. The next step is to combine the terms so that the tabulated enthalpic and entropic expressions are the subjects of the formulae.

From 5-3:

$$\frac{1}{T_1}(\Delta H_{f,Ox}^{T_1} - \Delta H_{f,Red}^{T_1}) + \frac{1}{T_1}(\Delta H_{f,H_2}^{T_1} - \Delta H_{f,H_2O}^{T_1}) - (\Delta S_{f,H_2}^{T_1} - \Delta S_{f,H_2O}^{T_1}) = (\Delta S_{f,Ox}^{T_1} - \Delta S_{f,Red}^{T_1}) \quad (5-5)$$

From 5-4

$$\frac{1}{T_2}(\Delta H_{f,Ox}^{T_2} - \Delta H_{f,Red}^{T_2}) = \frac{1}{2T_2}\Delta H_{f,O_2}^{T_2} - \frac{1}{2}\Delta S_{f,O_2}^{T_2} - (\Delta S_{f,Red}^{T_2} - \Delta S_{f,Ox}^{T_2}) \quad (5-6)$$

However, in order to obtain single enthalpic and entropic expressions, the temperatures at which the reactions are conducted must be converted to the standard reaction temperature.

The temperature change expressions for enthalpy and entropy are given below in equations (5-7) and (5-8), assuming C_p is a weak function of temperature;

$$\Delta S^{T,P} = \Delta S^{T_0,P} + C_p \ln\left(\frac{T}{T_0}\right) \quad (5-7)$$

$$\Delta H^{T,P} = \Delta H^{T_0,P} + C_p(T - T_0) \quad (5-8)$$

Using these expressions to convert all the appropriate temperature terms in (5-5) and (5-6) into T_0 yields (5-9) and (5-10) respectively:

$$\begin{aligned} \Delta S_{f,Ox}^\theta - \Delta S_{f,Red}^\theta &= \frac{1}{T_1}(\Delta H_{f,Ox}^\theta - \Delta H_{f,Red}^\theta) + \frac{1}{T_1}(\Delta H_{f,H_2}^\theta - \Delta H_{f,H_2O}^\theta) - (\Delta S_{f,H_2}^\theta - \Delta S_{f,H_2O}^\theta) \\ &\quad + (C_p^{H_2} + C_p^{Ox} - C_p^{Red} - C_p^{H_2O})\left(\frac{T_1 - T_0}{T_1} - \ln\left(\frac{T_1}{T_0}\right)\right) \end{aligned} \quad (5-9)$$

$$\begin{aligned} \Delta H_{f,Ox}^\theta - \Delta H_{f,Red}^\theta &= \left(C_p^{Red} + \frac{C_p^{O_2}}{2} - C_p^{Ox}\right)\left(T_2 - T_0 - T_2 \ln\left(\frac{T_2}{T_0}\right)\right) + \frac{\Delta H_{f,O_2}^\theta}{2} - \frac{T_2 \Delta S_{f,O_2}^\theta}{2} \\ &\quad + T_2(\Delta S_{f,Ox}^\theta - \Delta S_{f,Red}^\theta) \end{aligned}$$

$$(5-10)$$

At this point, the two equations can be separated by inter substitution to yield one expression with only entropic terms (5-11) and another with only enthalpic terms (5-12):

$$\begin{aligned} \Delta S_{f,Red}^{\theta} - \Delta S_{f,Ox}^{\theta} &= \frac{\Delta H_{f,H_2}^{\theta} + \frac{1}{2}\Delta H_{f,O_2}^{\theta} - \Delta H_{f,H_2O}^{\theta}}{T_2 - T_1} - \frac{T_1}{T_2 - T_1} \left(\Delta S_{f,H_2}^{\theta} + \frac{T_2}{2T_1} \Delta S_{f,O_2}^{\theta} - \Delta S_{f,H_2O}^{\theta} \right) + \\ & (C_p^{Red} - C_p^{Ox}) \left[1 - \frac{T_2}{T_2 - T_1} \ln \left(\frac{T_2}{T_0} \right) + \frac{T_1}{T_2 - T_1} \ln \left(\frac{T_1}{T_0} \right) \right] + (C_p^{H_2} - C_p^{H_2O}) \left[\frac{T_1 - T_0}{T_2 - T_1} - \frac{T_1}{T_2 - T_1} \ln \left(\frac{T_1}{T_0} \right) \right] + \\ & \frac{C_p^{O_2}}{2} \left[\frac{T_2 - T_0}{T_2 - T_1} - \frac{T_2}{T_2 - T_1} \ln \left(\frac{T_2}{T_0} \right) \right] \end{aligned} \quad (5-11)$$

$$\begin{aligned} \Delta H_{f,Red}^{\theta} - \Delta H_{f,Ox}^{\theta} &= \frac{T_2}{T_2 - T_1} \left(H_{f,H_2}^{\theta} + \frac{T_1}{2T_2} \Delta H_{f,O_2}^{\theta} - \Delta H_{f,H_2O}^{\theta} \right) - \frac{T_1 T_2}{T_2 - T_1} \left(\Delta S_{f,H_2}^{\theta} + \right. \\ & \left. \frac{\Delta S_{f,O_2}^{\theta}}{2} - \Delta S_{f,H_2O}^{\theta} \right) + (C_p^{Red} - C_p^{Ox}) \left(T_0 - \frac{T_1 T_2}{T_2 - T_1} \ln \left(\frac{T_2}{T_1} \right) \right) + \frac{C_p^{O_2}}{2} \left[\frac{T_1(T_2 - T_0)}{T_2 - T_1} - \frac{T_1 T_2}{T_2 - T_1} \ln \left(\frac{T_2}{T_0} \right) \right] + \\ & (C_p^{H_2} - C_p^{H_2O}) \left[\frac{T_2(T_1 - T_0)}{T_2 - T_1} - \frac{T_1 T_2}{T_2 - T_1} \ln \left(\frac{T_1}{T_0} \right) \right] \end{aligned} \quad (5-12)$$

At this point, known thermodynamic data for water, hydrogen and oxygen can be plugged into equations (5-11) and (5-12). A summary of the necessary data is provided below in table 5-1.

Table 5-1 Thermodynamic properties of hydrogen, oxygen and water²

Molecule	Property	Value
H ₂	ΔH_f^{θ}	0
	ΔS_f^{θ}	0.1307 kJ/mol/K
	$C_p^{H_2}$	0.0288 kJ/mol/K
O ₂	ΔH_f^{θ}	0
	ΔS_f^{θ}	0.2052 kJ/mol/K
	$C_p^{O_2}$	0.0294 kJ/mol/K
H ₂ O	ΔH_f^{θ}	-241.8 kJ/mol
	ΔS_f^{θ}	0.1888 kJ/mol/K
	$C_p^{H_2O}$	0.0336 kJ/mol/K

Based on comparisons with tabulated values for $\Delta\Delta H_f^\theta = \Delta H_{f,Red}^\theta - \Delta H_{f,Ox}^\theta$ and $\Delta\Delta S_f^\theta = \Delta S_{f,Red}^\theta - \Delta S_{f,Ox}^\theta$, it was determined that 400 kJ/mol and 50 J/mol/K are conservative estimates for upper bounds for the enthalpy and entropy differences respectively. Keeping these estimates in mind, figure 5-1 shows the thermodynamically feasible region based on the expressions obtained above, and the target region for this work.

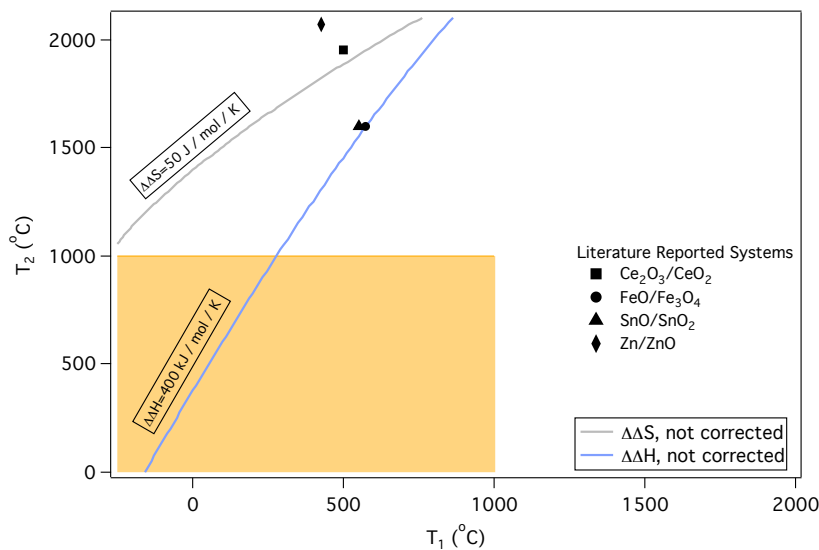


Figure 5-5-1 Thermodynamically feasible region for two-step thermochemical water splitting, and some cycles reported in literature.

The first key point of note is that based on this graph, it would be thermodynamically unfeasible to obtain a two-step thermochemical cycle that would operate under 1000°C. In figure 5-1, the region of thermodynamic feasibility is above the grey line. This is well outside the target maximum temperature of 1000°C. On this plot, other reported thermochemical cycles are also presented as a check on the accuracy of this simple model. This is where the inaccuracy of one of the assumptions is demonstrated. The literature data obtained from the SnO/SnO₂ cycle and the FeO/Fe₃O₄ cycles sits outside this “region of thermodynamic

feasibility". Thus, further corrections need to be made to this model in order to ensure that these data fit the predicted model.

In constructing this simple model, it was assumed that at each step, the solid is in equilibrium with an equilibrium partial pressure of the gaseous reactants and products. However, most of these reactions are conducted in flow systems, where the gases are not equilibrated with the solids that they are interacting with. Thus, the differing partial pressures need to be accounted for. The next section of this chapter will focus on the pressure corrections applied to the system to see if this improves the accuracy of this model.

5.3 Correcting state variables for partial pressure changes

As stated in section 5.2, the next step was to correct the equations above (5-11) and (5-12) for the deviations from equilibrium pressure. In order to do these pressure corrections, the isothermal gradients in pressure of enthalpy and entropy were used: $\left(\frac{\partial H}{\partial P}\right)_T$ and $\left(\frac{\partial S}{\partial P}\right)_T$, and the enthalpic and entropic contributions were integrated from the pressure of the reaction, down to the reference pressure. Thus, equations (5-13) and (5-14) were obtained.

$$\begin{aligned} \Delta S_{f,Red}^\theta - \Delta S_{f,Ox}^\theta &= \frac{\Delta H_{f,H_2}^\theta + \frac{1}{2}\Delta H_{f,O_2}^\theta - \Delta H_{f,H_2O}^\theta}{T_2 - T_1} - \frac{T_1}{T_2 - T_1} \left(\Delta S_{f,H_2}^\theta + \frac{T_2}{2T_1} \Delta S_{f,O_2}^\theta - \Delta S_{f,H_2O}^\theta \right) - \\ &\left(\frac{T_1}{T_2 - T_1} \right) \left(R \ln \left(\frac{P_{H_2O}}{P_{H_2}} \right) + \frac{RT_2}{2T_1} \ln \left(\frac{P_\theta}{P_{O_2}} \right) \right) + (C_p^{Red} - C_p^{Ox}) \left[1 - \frac{T_2}{T_2 - T_1} \ln \left(\frac{T_2}{T_0} \right) + \frac{T_1}{T_2 - T_1} \ln \left(\frac{T_1}{T_0} \right) \right] + \\ &(C_p^{H_2} - C_p^{H_2O}) \left[\frac{T_1 - T_0}{T_2 - T_1} - \frac{T_1}{T_2 - T_1} \ln \left(\frac{T_1}{T_0} \right) \right] + \frac{C_p^{O_2}}{2} \left[\frac{T_2 - T_0}{T_2 - T_1} - \frac{T_2}{T_2 - T_1} \ln \left(\frac{T_2}{T_0} \right) \right] \end{aligned} \quad (5-13)$$

$$\begin{aligned}
\Delta H_{f,Red}^{\theta} - \Delta H_{f,ox}^{\theta} &= \frac{T_2}{T_2-T_1} \left(H_{f,H_2}^{\theta} + \frac{T_1}{2T_2} \Delta H_{f,O_2}^{\theta} - \Delta H_{f,H_2O}^{\theta} \right) - \frac{T_1 T_2}{T_2-T_1} \left(\Delta S_{f,H_2}^{\theta} + \frac{\Delta S_{f,O_2}^{\theta}}{2} - \right. \\
&\Delta S_{f,H_2O}^{\theta} \left. \right) - \left(\frac{RT_1 T_2}{T_2-T_1} \right) \ln \left(\frac{P_{H_2O}}{P_{H_2}} \sqrt{\frac{P_{\theta}}{P_{O_2}}} \right) + (C_p^{Red} - C_p^{Ox}) \left(T_0 - \frac{T_1 T_2}{T_2-T_1} \ln \left(\frac{T_2}{T_1} \right) \right) + \frac{C_p^{O_2}}{2} \left[\frac{T_1(T_2-T_0)}{T_2-T_1} - \right. \\
&\left. \frac{T_1 T_2}{T_2-T_1} \ln \left(\frac{T_2}{T_0} \right) \right] + (C_p^{H_2} - C_p^{H_2O}) \left[\frac{T_2(T_1-T_0)}{T_2-T_1} - \frac{T_1 T_2}{T_2-T_1} \ln \left(\frac{T_1}{T_0} \right) \right] \quad (5-14)
\end{aligned}$$

Under conventional flow reaction setups, the gases formed are often swept off the surface by an inert carrier gas so that the product concentrations are much lower than 100% at 1 atm. Fig. 5-2 shows the influence of the pressure corrections on the isentropic and isenthalpic lines. Partial pressure of water is set at the saturation vapor pressure at 60°C (~0.2 atm) and the partial pressure of hydrogen is lower than that of water by a factor of 100 for Fig. 5-2. The partial pressure of oxygen in the thermal reduction step is set at 1/100 of the reference pressure (1% of oxygen and 99% of carrier gas) for Fig. 4-2. The reaction temperatures (T_1 and T_2) for the reported ceria³, iron⁴, tin⁵ and zinc⁶ systems are included in Fig. 5-2, all of which are located in the allowed region with pressure corrections. It is clear from Fig. 5-2 that lower concentrations (partial pressures) of products result in lower isentropic and isenthalpic lines, which enlarge the thermodynamically allowed region but diminish practicality.

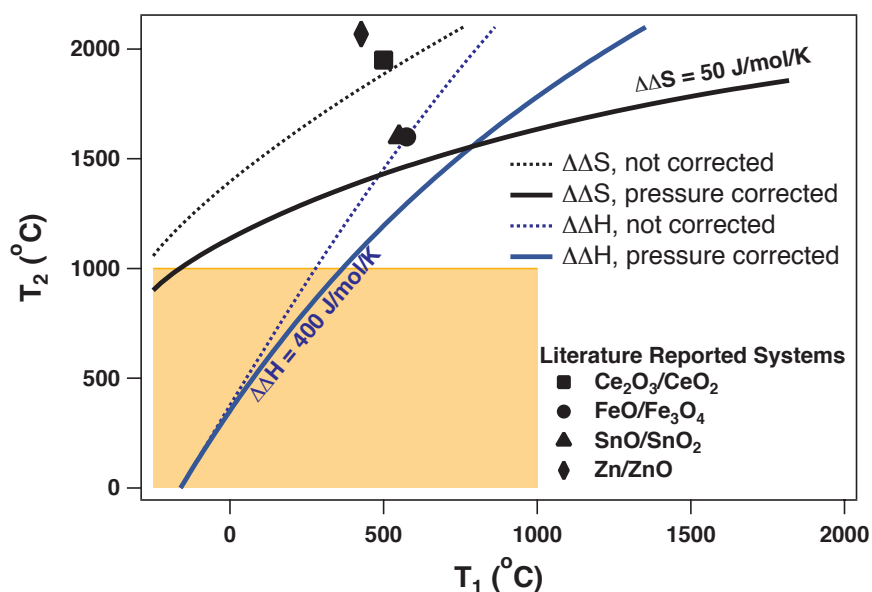


Figure 5-5-2 Isentropic and Isenthalpic lines with partial pressure corrections

5.4 Conclusion

In conclusion, the exercise of performing a thermodynamic analysis on the two step thermochemical water splitting cycle yielded a very important lesson, that the cycle cannot be completed under the target temperature in two steps. The accuracy of the thermodynamic analysis was confirmed by ensuring that the thermochemical cycles published in literature are in fact in the permissible region. The original objective of this section of the thesis was to identify possible combinations of metals that would allow the formation of clusters that would complete a thermochemical water splitting cycle. However, the exercise has instead shown, that a two step cycle cannot be closed under 1000°C. Thus, multi-step cycles must be considered for the improved feasibility of the cycle.

5.5 Bibliography

- (1) Meredig, B.; Wolverton, C. *Phys. Rev. B* **2011**, 83, 239901.
- (2) Lide DR (2008) CRC Handbook of Chemistry and Physics (CRC, New York),
- (3) Abanades, S.; Flamant, G. *Solar Energy* **2006**, 80, 1611–1623.

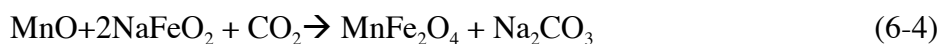
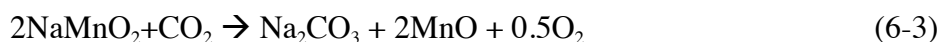
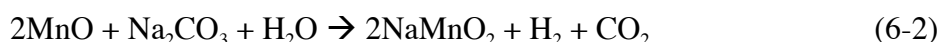
- (4) Charvin, P. et al., *Energy* **2007**, 32, 1124–1133.
- (5) Abanades, S. et al., *International Journal of Hydrogen Energy* **2008**, 33, 6021–6030.
- (6) Steinfeld, A. *International Journal of Hydrogen Energy* **2002**, 27, 611–619.

Chapter 6 Mn₃O₄ based thermochemical cycle^{##}

6.1 Introduction

Given the revelations of the thermodynamic analysis in Chapter 4, some background literature work was conducted into known multiple step thermochemical water splitting cycles that operate below 1000°C¹⁻³. Unfortunately most of the cycles reported in the literature involve corrosive materials such as strong acids and complex solution mixtures. One cycle in particular seems of interest when comparing these multi-step cycles. This is a cycle comprised of Manganese Ferrite, MnFe₂O₄, and Sodium Carbonate Na₂CO₃^{4,5}.

This cycle, while depicted in their 2011 work as two step cycle, actually proceeds via a set of 4 steps:



At face value, this set of reactions seems very promising, as it fulfills all the criteria set forth for the desired system; it does not contain any corrosive materials or complex mixtures. The highest temperature required is 800°C. However, the major drawback lies in the true closing of the cycle. There are two possible ferrite phases that can be formed, α -NaFeO₂ and β -NaFeO₂. It is difficult to control the distribution of the two phases that are formed in reaction (6-1). The major problem lies in the sodium extraction from these phases. Only the β phase allows the sodium to be extracted under the conditions of the reaction. Thus, in each cycle that the material goes through, some of the iron phase is lost as the α -NaFeO₂. And in the limit of

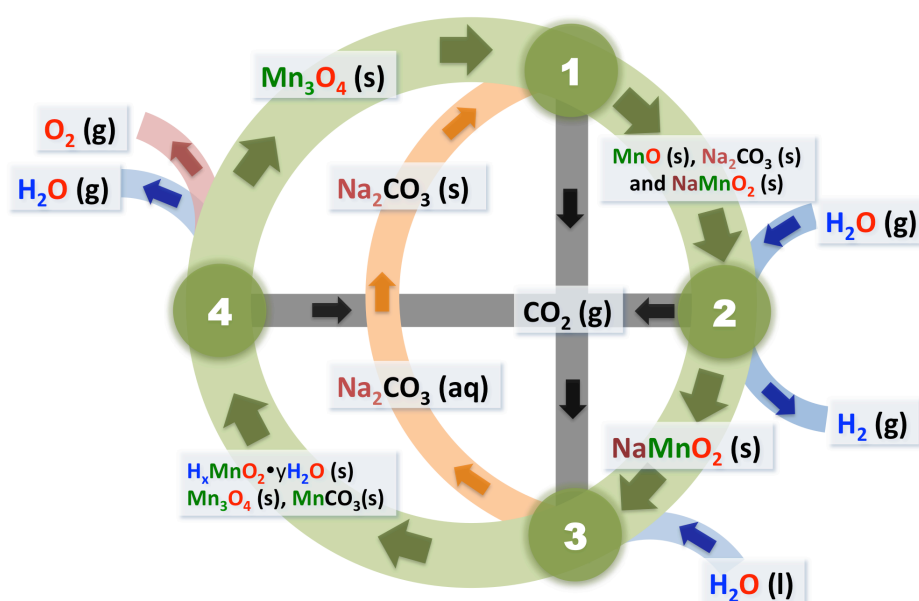
^{##} Originally published in PNAS DOI: 10.1073/pnas.1206407109

running the material through multiple cycles, there will be a loss in the total activity per gram of solid as more and more of the material gets “left” as the inactive ferrite.

Given that the metal doing the actual redox chemistry is the manganese, in order to explore this avenue as a means to create a truly cyclable material for thermochemical water splitting, the next approach was to use Mn_3O_4 as the starting material. This oxide has the same structure as MnFe_2O_4 , except the Fe^{3+} ions are replaced by Mn^{3+} ions. The remainder of this chapter looks at this oxide as a basis for thermochemical water splitting⁶.

6.2 Step by step analysis of Mn_3O_4 thermochemical cycle

Thermochemical Cycle Overview



Step	Reaction	Temp (°C)
1	$3\text{Na}_2\text{CO}_3(\text{s}) + 2\text{Mn}_3\text{O}_4(\text{s}) \rightarrow 4\text{NaMnO}_2(\text{s}) + 2\text{CO}_2(\text{g}) + 2\text{MnO}(\text{s}) + \text{Na}_2\text{CO}_3$	850
2	$2\text{MnO}(\text{s}) + \text{Na}_2\text{CO}_3(\text{s}) + \text{H}_2\text{O}(\text{g}) \rightarrow \text{H}_2(\text{g}) + \text{CO}_2(\text{g}) + 2\text{NaMnO}_2(\text{s})$	850
3	$6\text{NaMnO}_2(\text{s}) + a\text{yH}_2\text{O}(\text{l}) + (3 + b)\text{CO}_2(\text{g}) \rightarrow 3\text{Na}_2\text{CO}_3(\text{aq}) + a\text{H}_x\text{MnO}_2 \cdot \text{yH}_2\text{O}(\text{s}) + b\text{MnCO}_3(\text{s}) + c\text{Mn}_3\text{O}_4(\text{s})$	80
4	$a\text{H}_x\text{MnO}_2 \cdot \text{yH}_2\text{O}(\text{s}) + b\text{MnCO}_3 + \rightarrow (2-c)\text{Mn}_3\text{O}_4(\text{s}) + a\text{yH}_2\text{O}(\text{g}) + b\text{CO}_2(\text{g}) + 0.5\text{O}_2(\text{g})$	850
Net	$\text{H}_2\text{O}(\text{g}) \rightarrow \text{H}_2(\text{g}) + 0.5\text{O}_2(\text{g})$	

a , b and c satisfy following relations: $a + b + 3c = 6$ and $(4-x)a + 2b + 8c = 18$

Figure 6-1 Overview of Mn_3O_4 based thermochemical water splitting cycle

We have developed a Mn-based, multistep, low-temperature water splitting cycle that has a highest operating temperature of 850°C. The thermochemical cycle consists of four main

steps (Fig. 6-1): (1) thermal treatment of a physical mixture of Na_2CO_3 and Mn_3O_4 to produce MnO , CO_2 , and $\alpha\text{-NaMnO}_2$ at 850°C , (2) oxidation of MnO in the presence of Na_2CO_3 by water to produce H_2 , CO_2 and $\alpha\text{-NaMnO}_2$ at 850°C , (3) Na^+ extraction from $\alpha\text{-NaMnO}_2$ by its suspension in aqueous solutions in the presence of bubbling CO_2 at 80°C , and (4) recovery of Mn_3O_4 by thermally reducing the sodium ion extracted solid produced in step (3) at 850°C . The net reaction is the stoichiometric splitting of water to hydrogen and oxygen without any by-product. The incorporation and extraction of Na^+ into and out of the manganese oxides are the critical steps in lowering the temperature required for both the hydrogen evolution and the thermal reduction steps (*vide infra*).

Steps 1 and 2: Hydrogen evolution on $\text{Mn}_3\text{O}_4/\text{Na}_2\text{CO}_3$

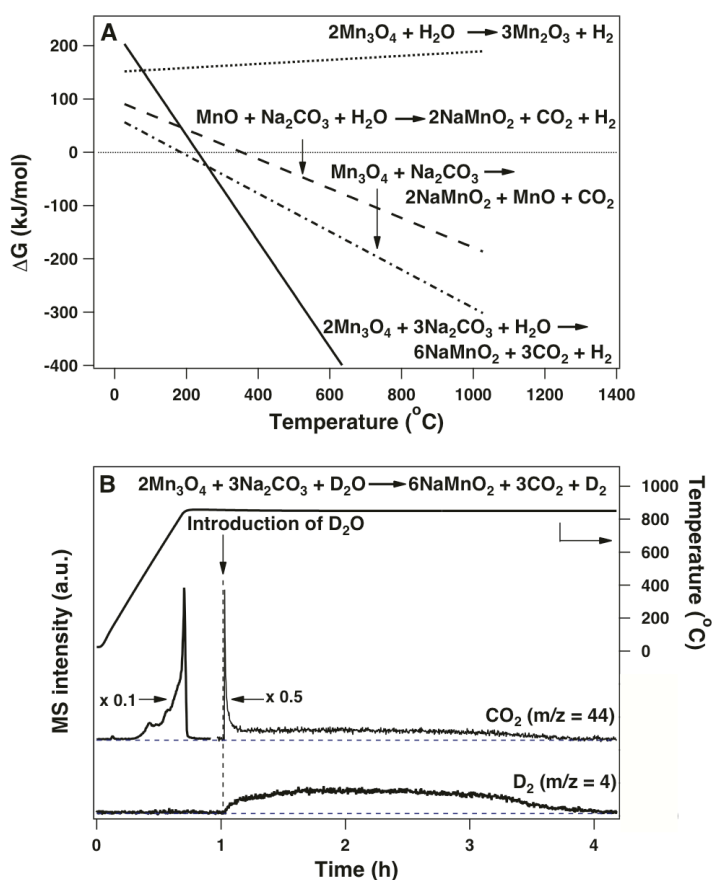


Figure 6-2 Addition of sodium carbonate is essential for low temperature water decomposition on Mn_3O_4 . (A) Thermodynamic estimates show Na_2CO_3 enables oxidation of Mn_3O_4 by

H₂O. ΔG for α -NaMnO₂ is adopted from Azad et al. ⁷, remainder of thermodynamic data are taken from the CRC handbook ⁸. (B) Production of D₂ and CO₂ in the oxidation of Mn₃O₄ to form α -NaMnO₂ by D₂O in the presence of Na₂CO₃ at 850°C.

The presence of Na⁺ enables the oxidation of Mn²⁺ in Mn₃O₄ to Mn³⁺ by water, leading to the formation of α -NaMnO₂, CO₂ and H₂. In the absence of Na₂CO₃, oxidation of Mn₃O₄ to Mn₂O₃ is always thermodynamically unfavorable ($\Delta G > 0$) (Fig. 6-2A, top dotted line)¹. The introduction of Na₂CO₃ drastically changes the thermodynamics of the oxidation reaction; the ΔG of reaction decreases with increasing temperature and becomes negative around 250°C (Fig. 6-2A, solid line). These thermodynamic estimates are consistent with our experimental observations in that water does not react with Mn₃O₄ in the absence of Na₂CO₃ at 850°C, and the amount of D₂ obtained by reacting D₂O (D₂O is used instead of H₂O to enhance the signal-to-noise ratio in the product detection and quantification) with the Mn₃O₄/Na₂CO₃ mixture at 850°C is equivalent to the amount that would be expected when Mn²⁺ is totally converted into Mn³⁺ (Fig. 6-2B).

We hypothesize that Na₂CO₃ extracts the Mn³⁺ from Mn₃O₄ at 500-850°C to form α -NaMnO₂, CO₂ and MnO (Fig. 6-1, step 1; note that CO₂ is observed while heating the Mn₃O₄/Na₂CO₃ mixture prior to exposure of water (Fig. 6-2B)). Hydrogen is then formed from the water oxidation of MnO at 850°C in the presence of Na₂CO₃ (Fig. 6-1, step 2). We confirmed that this step can occur independently at 850°C. The ΔG for both steps decrease with increasing temperature and become energetically favorable above 400°C, (Fig. 6-2A). Upon the introduction of D₂O, a sharp peak indicating the release of CO₂ is observed. In contrast, the rate of D₂ evolution increases slowly after the D₂O introduction, and reached a plateau after ~30 min. The drastically different kinetics for the evolution of CO₂ and D₂ suggests that step 2 is not an elementary step. The stoichiometry of the proposed reaction predicts that two thirds of the α -NaMnO₂ and CO₂ should be formed via step 1 and the remaining third via step 2. These

amounts are experimentally confirmed by the 2:1 ($\pm 15\%$) ratio of the amount of CO_2 evolved before and after the introduction of D_2O (Fig. 6-2B).

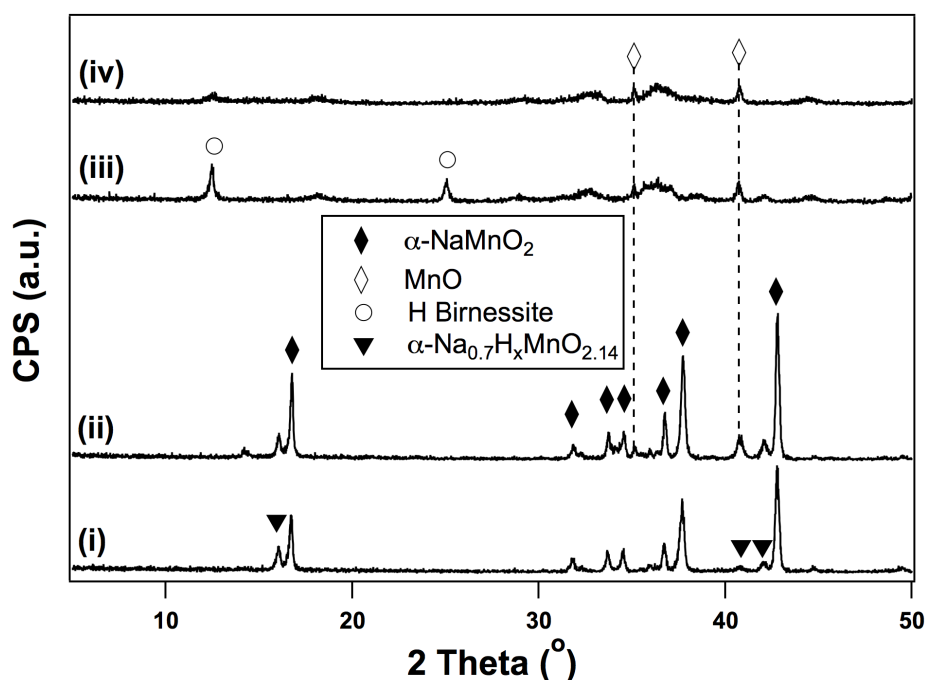


Figure 6-3 Powder X-ray diffraction patterns used to identify solids phases in hydrogen evolution steps. (i) Solid collected after the hydrogen evolution step (after step 2); (ii) solid collected after reacting Mn_3O_4 with Na_2CO_3 at 850°C (after step 1); (iii) sample from (ii) hydrolyzed in an aqueous suspension in the presence of CO_2 at 80°C for 3h; and (iv) sample from (iii) annealed 180°C in Ar for 1h.

Further support for this reaction pathway is provided by the identification of the reaction intermediate MnO by powder X-ray diffraction (XRD) measurements. The XRD pattern of the solid obtained after the hydrogen evolution reaction (steps 1 and 2 in Fig. 6-1) contains $\alpha\text{-NaMnO}_2$ and a hydrated product $\alpha\text{-Na}_{0.7}\text{MnO}_{2.14}$ (Fig. 6-3(i)); $\alpha\text{-NaMnO}_2$ can form $\alpha\text{-Na}_{0.7}\text{MnO}_{2.14}$ when exposed to water⁹). Importantly, the XRD pattern of the powder collected after step 1 clearly shows the presence of MnO , in addition to the peaks attributed to $\alpha\text{-NaMnO}_2$ and $\alpha\text{-Na}_{0.7}\text{MnO}_{2.14}$ (Fig. 6-3(ii)). The diffraction peaks corresponding to MnO persist after $\alpha\text{-NaMnO}_2$ is fully hydrolyzed in the presence of CO_2 (Fig. 6-3(iii); the hydrolysis process of $\alpha\text{-NaMnO}_2$ is discussed further below). Furthermore, after annealing the hydrolyzed sample

at 180°C in Ar, the only sharp peaks are those from MnO (Fig. 6-3(iv)). The identification of the reaction intermediate MnO strongly supports our proposed reaction pathway.

Step 3: Na⁺ extraction of α -NaMnO₂

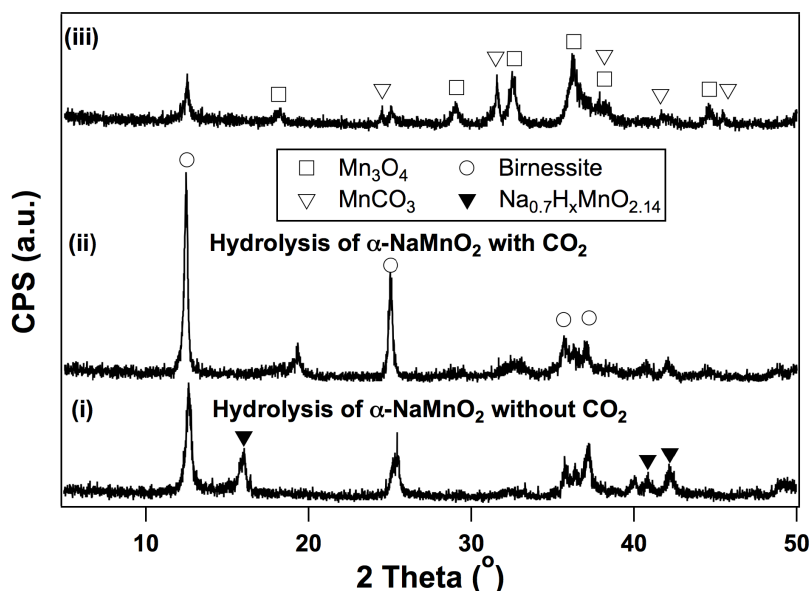


Figure 6-4 Powder X-ray diffraction patterns used to identify intermediate phases in hydrolysis of α -NaMnO₂. (i) Hydrolysis of α -NaMnO₂ in an aqueous suspension at 80°C for 3h; (ii) hydrolysis of α -NaMnO₂ in an aqueous suspension at 80°C for 3h with bubbling CO₂ and (iii) hydrolysis of α -NaMnO₂ in water vapor and CO₂ under hydrothermal condition at 140°C for 5h.

Na⁺ can be efficiently extracted from α -NaMnO₂ via hydrolysis in the presence of CO₂. Na⁺ extraction is a critical step in closing the low-temperature thermochemical cycle, since α -NaMnO₂ cannot be thermally reduced below 1000°C¹⁰. α -NaMnO₂ is a layered compound, with Na⁺ sandwiched between MnO₆ octahedral sheets¹¹. Water can intercalate into these sheets, expanding the distance between adjacent layers to form sodium birnessite (Fig. 6-4)¹¹, as evidenced by the disappearance of the diffraction peak at 16.7° in α -NaMnO₂ and the appearance of the 12.5° peak in birnessite (Fig. 6-4(i)). The mobility of Na⁺ is greatly enhanced in birnessite compared to that in α -NaMnO₂ as the MnO₆ sheets are pillared by water, and therefore can easily be exchanged by other cations including protons¹¹. Complete Na⁺ extraction from α -NaMnO₂ by hydrolysis in acidic conditions to form protonic birnessite (H⁺

birnessite) has been reported¹². Here, this conversion is achieved by bubbling CO₂ through an aqueous suspension of α -NaMnO₂ at 80°C for 3h. A disproportionation mechanism has been proposed to explain the oxidation state change of Mn in α -NaMn(III)O₂ when it converts into the birnessite phase with an average oxidation state of 3.5-3.8^{11,12}:



The Mn(IV) remains in the solid birnessite phase while Mn(II) is generally believed to dissolve in the aqueous phase^{11,12}. An insoluble Mn(II) salt or other compounds with Mn(II) are expected to form in the CO₂-assisted hydrolysis of α -NaMnO₂. Very weak and broad diffraction peaks corresponding to MnCO₃ and Mn₃O₄ phases are present in the sample collected after hydrolysis of α -NaMnO₂ with CO₂ under ambient condition (Fig. 6-4(ii)). However, characteristic diffraction peaks for MnCO₃ and Mn₃O₄ phases are observed after hydrolysis of α -NaMnO₂ with CO₂ under hydrothermal conditions (Fig. 6-4(iii)). Accelerated crystal growth under hydrothermal conditions is most likely responsible for MnCO₃ and Mn₃O₄ crystals large enough to be detected by the diffraction measurements. The presence of the MnCO₃ and Mn₃O₄ phases is strong evidence to support the disproportion mechanism (Eq. 6-5; implies the average oxidation state of Mn in all Mn-containing solid is still +3).

Step 4: Oxygen evolution by thermal reduction of solids from Na⁺ extraction of α -NaMnO₂

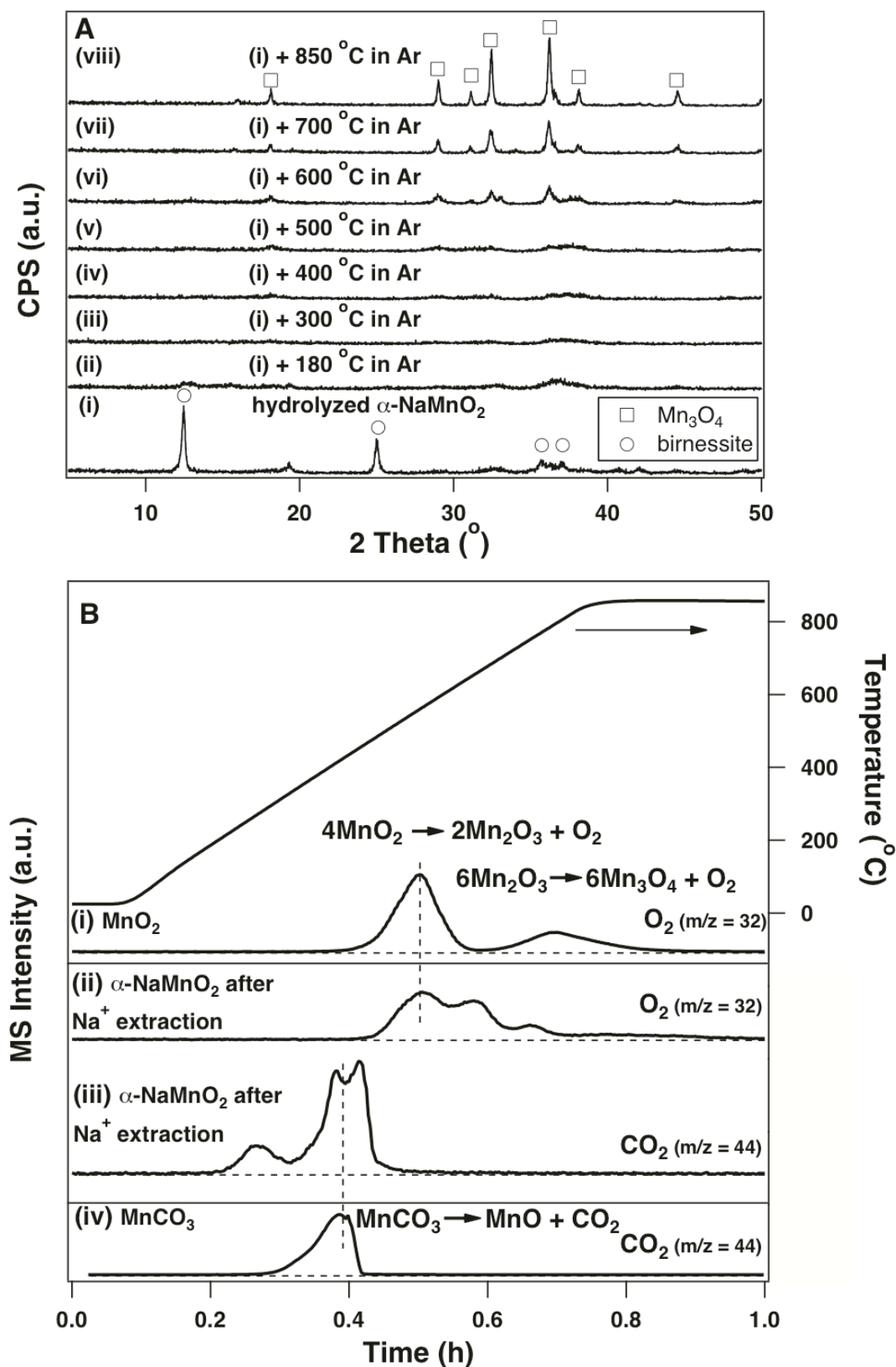


Figure 6-5 Thermal reduction of Na⁺ extracted α -NaMnO₂. (A) X-ray diffraction patterns of: (i) Na⁺ extracted α -NaMnO₂, and (i) after annealing at (ii) 180°C, (iii) 300°C, (iv) 400°C, (v) 500°C, (vi) 600°C, (vii) 700°C and (viii) 850°C in Ar for 1h. (B) Temperature programmed reaction of: (i) MnO₂, (ii) and (iii) Na⁺ extracted α -NaMnO₂ and (iv) MnCO₃.

Thermal reduction of the mixture formed after sodium extraction of α -NaMnO₂ (Fig. 6-5A(i)) in Ar at 850°C recovers Mn₃O₄. The layered structure of protonic birnessite collapses upon heating to 180°C in Ar, presumably yielding amorphous Mn(III, IV)O_x (Fig. 6-5A(ii)). The amorphous phase persisted up to 500°C, where broad and weak diffraction peaks of Mn₃O₄ begin to appear. These results are consistent with the temperature-programmed desorption profile of O₂ (Fig. 6-5B(ii)), with the onset of O₂ desorption peak at ~450°C. The first oxygen desorption peak at ~565°C from the mixture is attributed to the thermal reduction of MnO₂ to Mn₂O₃ (Fig. 6-5B(i)), indicating the reduction of amorphous MnO₂ to Mn₂O₃. The diffraction peaks of Mn₃O₄ for the Na⁺ extracted mixture gradually grow more intense and narrower as temperature increases, however, no diffraction peaks corresponding to MnO₂ or Mn₂O₃ are observed throughout the temperature range tested. The oxygen desorption peaks for the Na⁺ extracted phase above 565°C do not correspond to the desorption peaks from the reduction of Mn₂O₃ to Mn₃O₄ at 810°C (Fig. 6-5B(i)); these desorption events are attributed to the solid state reaction between amorphous Mn₂O₃ and MnO present in the mixture. The CO₂ desorption peak from the mixture appears at a similar temperature range as the decomposition of MnCO₃ to MnO and CO₂ (Fig. 6-5B(iii) and (iv)), confirming the presence of MnCO₃. The XRD pattern for the sample after thermal reduction is almost identical to that of commercial Mn₃O₄, except for a very weak peak at ~16° corresponding to trace amount of α -Na_{0.7}MnO_{2.14}.

6.3 Recyclability of the Mn_3O_4 cycle

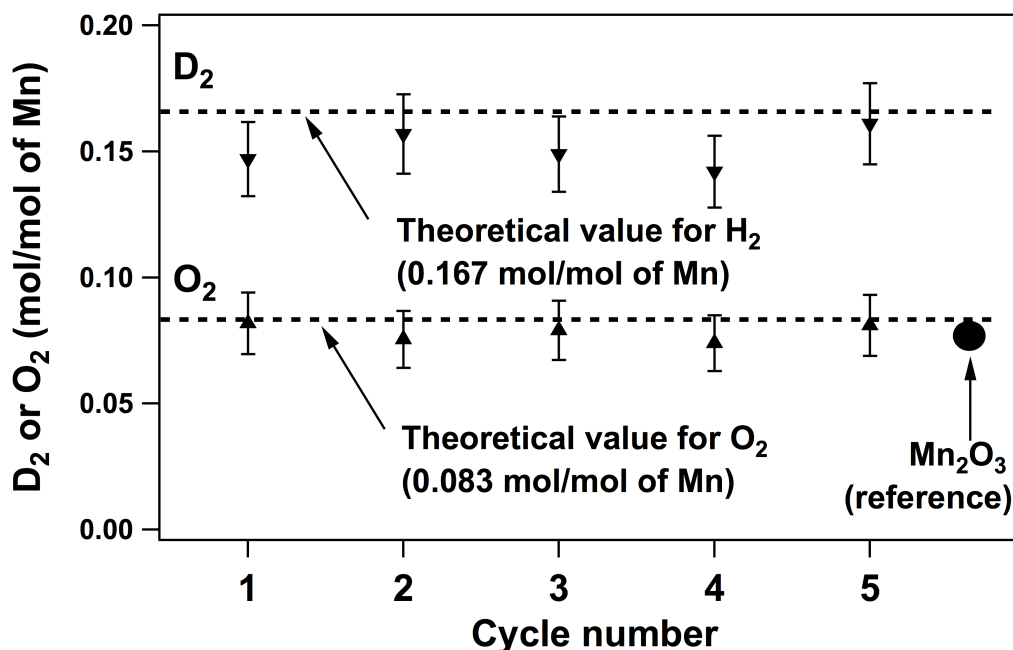


Figure 6-6 Multiple cycles of the Mn-based thermochemical water splitting system

The Mn-based thermochemical system shown here exhibits >90% yield for both hydrogen and oxygen evolution and shows no sign of deactivation during 5 cycles (Fig. 6-6). The amount of O_2 released from a thermal reduction of a commercial, crystalline Mn_2O_3 to form Mn_3O_4 (the solid black circle in Fig. 6-6) is identical to that from the thermal reduction presented above, consistent with the recovery of Mn_3O_4 in the thermochemical cycle. Furthermore, the XRD pattern of the Mn_3O_4 recovered after the oxygen evolution is identical among 5 cycles and match the reference spectrum.

The key feature contributing to the recyclability of the Mn-based system is the complete shuttling of Na^+ into and out of the manganese oxides. The Na^+ incorporation takes advantage of thermodynamically favorable reactions (Fig. 6-1, steps 1 and 2) to form $\alpha\text{-NaMnO}_2$. The Na^+ extraction step exploits the mobility of Na^+ in the layered structure when intercalated by water, and is further enhanced by the presence of CO_2 to drive the equilibrium towards the mixture of protonic birnessite, Mn_3O_4 and MnCO_3 . This mixture can be thermally reduced to Mn_3O_4 at 850°C , closing the thermochemical cycle. Importantly, the trace amount of by-product formed

by the incomplete Na^+ extraction is reintegrated into the $\alpha\text{-NaMnO}_2$ phase in the next cycle, avoiding the accumulation of a permanent, inactive phase.

6.4 Conclusions

Comparisons to other multistep thermal water splitting systems

The highest temperature required for the Mn-based cycle is near those temperatures used with other low-temperature multistep water splitting cycles. Both the hydrogen and oxygen evolution steps are conducted at 850°C in the Mn-based cycle, similar to the temperature for the highest temperature step in the now piloted sulfur-iodine system¹³.

The Mn-based system does not involve any corrosive materials, while almost all previously reported multistep low-temperature thermal water splitting cycles have toxic and/or corrosive intermediates in one or more of the steps in the cycle. Most notably, in each step of the sulfur-iodine cycle, there is at least one of the following chemicals: SO_2 , H_2SO_4 , I_2 and HI , which pose great environmental and engineering challenges¹³.

Hydrogen production via the water oxidation of metal oxides with a spinel structure in the presence of sodium carbonate was pioneered by Tamaura et al^{14,15}. However, their cycle was not closed due to the use of sacrificial Fe_2O_3 to extract Na^+ from sodium manganese iron oxide produced in the hydrogen evolution step¹⁶. Sodium sources other than Na_2CO_3 , such as NaOH , have also been employed to facilitate the oxidation of Mn^{2+} to Mn^{3+} in the water splitting step¹⁷. The volatility of NaOH at $>800^\circ\text{C}$ and incomplete Na^+ extraction by water to recover NaOH pose challenges to its implementation¹⁰. Based upon the work of Tamaura et al., Sturzenegger et al. first pointed out the possibility of creating a Mn-based cycle that utilizes Na_2CO_3 rather than NaOH ¹⁷. Here, we have shown that a closed cycle of this type can be created.

Implementation issues

There are a number of technical aspects of the Mn-based cycle proposed in this work that require solution prior to an effective implementation. It is likely that the kinetics of hydrogen evolution (Fig. 6-2B) will need to be increased. Here, no efforts have been made to control parameters such as solid particle size. Thus, there are several ways that the kinetics of hydrogen evolution may be enhanced, e.g., creation of small particles. The need for cooling the α -NaMnO₂ produced in the hydrogen evolution step from 850°C to 80°C to perform the Na⁺ extraction in the aqueous phase before heating the Na⁺ extracted phase back to 850°C may impose a considerable energy cost. Moreover, Na₂CO₃ needs to be recovered from the aqueous solution in the Na⁺ extraction step. Further research in alternative Na⁺ extraction method is certainly warranted. However, Sturzenegger and Nuesch have performed an efficiency analysis for a cycle that does require heating and cooling solids to the temperatures used here¹⁸. Their results suggest a process of this type could be feasible. Of course, higher energy efficiency will be achieved by educated reactor design with efficient heat recovery and recycling among different stages of the cycle¹⁸.

6.5 Bibliography

- (1) Kodama, T.; Gokon, N. *Chem. Rev* **2007**, *107*, 4048–4077.
- (2) Steinfeld, A. *Solar Energy* **2005**, *78*, 603–615.
- (3) Rosen, M. A. *Energy* **2010**, *35*, 1068–1076.
- (4) Alvani, C.; et al. *International Journal of Hydrogen Energy* **2006**, *31*, 2217–2222.
- (5) Varsano, F. et. al. *Solid State Ionics* **2011**, *187*, 19–26.
- (6) Xu, B.; Bhawe, Y.; Davis, M. E. *Proceedings of the National Academy of Sciences* **2012**, *109*, 9260–9264.
- (7) Azad, A. M.; Sreedharan, O. M.; Gnanamoorthy, J. B. *Journal of Nuclear Materials* **1987**, *144*, 94–104.
- (8) Lide DR (2008) CRC Handbook of Chemistry and Physics (CRC, New York).

- (9) Le Goff, P. *Solid State Ionics* **1993**, *61*, 309–315.
- (10) Kreider, P. B., et al. *International Journal of Hydrogen Energy* **2011**, *36*, 7028–7037.
- (11) Feng, Q.; Kanoh, H.; Ooi, K. *J Mater Chem.*, **1999**, *9*, 15.
- (12) Omomo, Y. et al. *Solid State Ionics* **2002**, *151*, 8.
- (13) Brown, L.; et al. **2002** *Nuclear production of hydrogen using thermochemical watersplitting cycles. Proc Int Congress on Advanced Nuclear Power Plants.*
- (14) Tamaura, Y.; et al. *Energy* **1995**, *20*, 6.
- (15) Tamaura, Y.; et al. *Int. J. Hydrogen energy*, **1998**, *23*, 1185-1191.
- (16) Kaneko, H.; *J Phys Chem Solids* **2001**, *62*, 1341–1347.
- (17) Sturzenegger, M.; et al. *T. J. Phys. IV France* **1999**, *09*, Pr3–331–Pr3–335.
- (18) Sturzenegger, M.; Nüesch, P. *Energy* **1999**, *24*, 959–970.

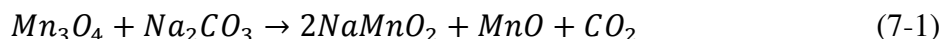
Chapter 7 Other Spinel structures[#]

7.1 Introduction

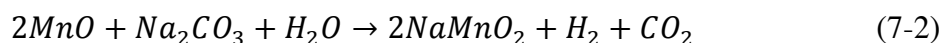
In chapter 6, one of the key points was the elucidation of a manganese oxide-based, thermochemical cycle for water splitting can be closed at 850°C without involving any toxic/corrosive chemicals.¹ This manganese oxide-based thermochemical cycle consists of the following three main steps:

1) *Hydrogen evolution step*: Mn(II) in Mn_3O_4 is oxidized by water in the presence of Na_2CO_3 , producing hydrogen. The spinel Mn_3O_4 is converted to a layered compound, $\alpha\text{-NaMnO}_2$, during this step. The hydrogen evolution step proceeds via two sequential reactions:

i) Mn_3O_4 reacts with Na_2CO_3 in the absence of water, forming $\alpha\text{-NaMnO}_2$ and MnO (reaction 1). The Mn(III) species is extracted from Mn_3O_4 through the reaction with Na_2CO_3 , leaving the Mn(II) species in the form of MnO.



ii) Mn(II) oxide is oxidized by water in the presence of Na_2CO_3 , producing hydrogen and $\alpha\text{-NaMnO}_2$ (reaction 2).



2) *Sodium cation extraction step*: The Mn(III) species in $\alpha\text{-NaMnO}_2$ cannot be thermally reduced below 1000°C,² whereas the transition from Mn(III) and Mn(IV) oxides to Mn_3O_4 occurs below 850°C. Therefore, it is critical to remove the sodium cation from the manganese oxide in order to close the thermochemical cycle below 1000°C. The sodium cations in $\alpha\text{-NaMnO}_2$ can be substituted with protons when it is suspended in water in the presence of CO_2 . Water molecules intercalate into the manganese oxide layers, increasing the distance between the layers and mobilizing sodium cations. Protons from carbonic acid, formed

[#] Originally Published in Chemistry of Materials DOI 10.1021/cm3038747

via the reaction of CO₂ and water, can exchange with the sodium cations between manganese oxide layers. When CO₂, and in turn protons, are in excess, almost all sodium cations can be removed from the manganese oxide structure. A disproportionation reaction accompanies the ion exchange process:



All Mn(IV) and the majority of Mn(III) species are in a proton exchanged birnessite phase. A fraction of the Mn(II) and the remainder of the Mn(III) are in an amorphous Mn₃O₄ phase, whereas the rest of Mn(II) species exists in the form of MnCO₃. Since no net oxidation or reduction reaction occurs during the ion exchange process, the average oxidation state of the Mn remains +3.

(3) *Thermal reduction reaction:* When the solid mixture collected after the sodium cation extraction is heated to 850°C, it restores to the spinel Mn₃O₄ phase, that can be used in the next cycle.

The entire section was focused on a single alkali carbonate (sodium) and a single spinel oxide (Mn₃O₄). In this chapter, both of these metals are varied in order to test for what the optimal combination of metals is. In addition for testing the activity in the thermochemical water splitting cycle, the activity in the thermochemical CO₂ reduction is also tested. Guiding principles for developing and optimizing low-temperature thermochemical cycles for water splitting and CO₂ reduction are discussed.

7.2 Materials & Methods

Materials preparation

Fe₃O₄ (95%), Mn₃O₄ (97%), Co₃O₄ (99.5%), Li₂CO₃ (99%), Na₂CO₃ (99.5%) and K₂CO₃ (99%) were purchased from Aldrich and used without further treatment. Na₂¹³CO₃ (99% ¹³C) was purchased from Cambridge Isotope Laboratories and used without further treatment. The

mixture of metal oxide (Fe_3O_4 , Mn_3O_4 or Co_3O_4) and alkali carbonate (Li_2CO_3 , Na_2CO_3 or K_2CO_3) with a molar ratio of 2:3 for the hydrogen evolution step was prepared by mixing these two powders in an agate mortar under ambient conditions. The alkali metal ions were extracted from the respective alkali metal oxides by bubbling CO_2 (99.997%, 10 cc/min) through an aqueous suspension of the powder (~5 wt% of solid) for 3 h at 80°C. The powder used for oxygen evolution step was obtained by separating the solid by centrifugation and drying at 100°C in air.

Reaction tests

All reaction tests were conducted in an Altamira Instruments AMI-200 catalyst characterization system equipped with a Dycor Dymaxion 2000 online mass spectrometer. The powders were pelletized, crushed, and sieved, and the particles between 20 and 35 mesh were used for testing. In order to prevent the alkali metal ions from interacting with the quartz used in the reactor tubes, the particles were supported between layers of 16-mesh alumina sand inside an alumina sheath. Under typical flow conditions, the flow rate of the gas was 50 cc/min. Depending on the experiments, the gases used were Ar (99.999%), CO_2/Ar (2%/98%) or $\text{D}_2\text{O}/\text{Ar}$ (5%/95%). Water (D_2O) vapor was introduced by flowing the carrier gas through a bubbler (50 cc/min) with D_2O at room temperature. D_2O was used instead of H_2O to obtain a better signal-to-noise ratio of the signal in the hydrogen evolution step ($m/z = 4$ for D_2 instead of $m/z = 2$ for H_2). A ramp-and-hold temperature profile was used in the characterization of these materials. The typical ramp rate was 20°C/min and the hold temperatures were varied as needed.

The conditions for water pulse experiments were similar to the flow reactions described above, apart from pulse introduction of D_2O to the gas stream for 2-15 minutes at the desired sample temperature. The reduction of the ion-extracted oxides was carried out under a 50 cc/min flow of Ar with a temperature ramp from room temperature to 850-1150°C at 20°C/min.

Characterization

Powder X-ray diffraction (XRD) patterns were collected on a Rigaku Miniflex II diffractometer using Cu K α radiation.

7.3 Reaction results

Mn₃O₄ and alkali carbonates (Li₂CO₃, Na₂CO₃ and K₂CO₃)

Mn₃O₄ reacts with Li₂CO₃ or Na₂CO₃ in Ar at or below 850°C, releasing CO₂ as the only product in the gas phase; whereas no appreciable reaction occurs between Mn₃O₄ and K₂CO₃ in this temperature range (Figure 7-1a, the molar ratio of Mn₃O₄ and alkali carbonates is 2:3). The CO₂ evolution peaks are at 625 and 850°C for Mn₃O₄/Li₂CO₃ and Mn₃O₄/Na₂CO₃, respectively. In contrast, no detectable amount of CO₂ is produced with the Mn₃O₄/K₂CO₃ mixture below or at 850°C. These observations clearly indicate the reactivity of alkali carbonates with Mn₃O₄, gauged by the temperature of CO₂ evolution peak, follows the sequence: Li₂CO₃ > Na₂CO₃ > K₂CO₃.

Unlike the reaction between Mn₃O₄ and Na₂CO₃ (reaction 7-1), where all Mn(II) species exist in the form of MnO after reaction,¹ Li₂Mn₂O₄ and Li_{0.4}Mn_{0.6}O phases are identified by powder X-ray diffraction (XRD) measurements after the temperature ramp-and-hold to 850°C for Li₂CO₃/Mn₃O₄ in the absence of water (bottom trace, Figure 7-2a). Since the atomic molar ratio of Li to Mn is 1:1 in the starting mixture, a small fraction of Li-containing phase must not be detected by XRD. This result could either be due to the crystal size of the Li-containing phase being below the detection limit of XRD, or due to the Li-containing phase being amorphous. No significant difference in the powder XRD pattern is observed after heating the K₂CO₃/Mn₃O₄ mixture in Ar atmosphere to 850°C (bottom and middle traces, Figure 7-2b), consistent with the lack of CO₂ evolution.

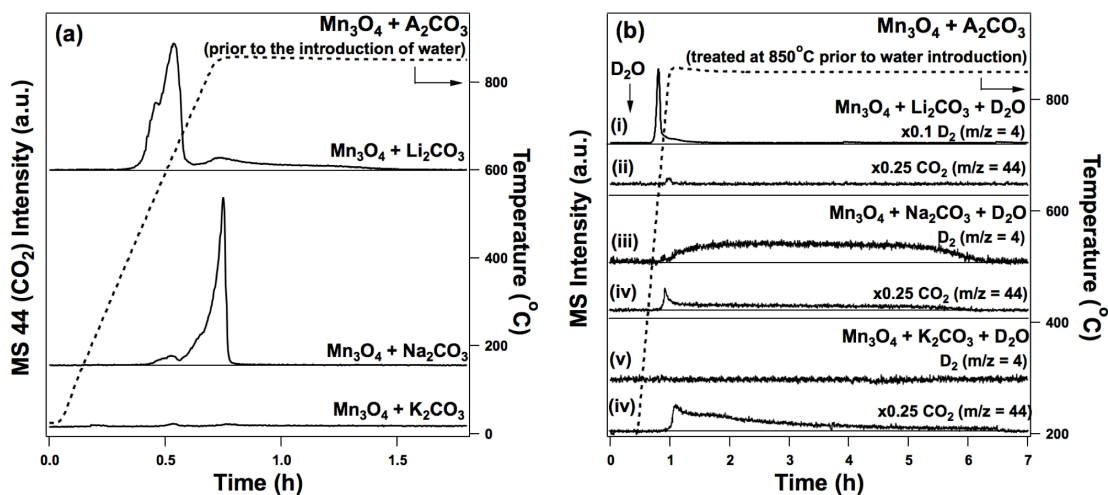


Figure 7-1 (a) Reaction of Mn_3O_4 with Li_2CO_3 (top trace), Na_2CO_3 (middle trace) and K_2CO_3 (bottom trace) in the absence of water. (b) Solids after the thermal treatment at 850 °C in (a) were cooled down to 200 °C, before D_2O was introduced. The samples were then subjected to a temperature ramp-and-hold treatment to 850 °C in $\text{D}_2\text{O}/\text{Ar}$ (5%/95%). (i, ii) D_2 and CO_2 traces for $\text{Mn}_3\text{O}_4/\text{Li}_2\text{CO}_3$; (iii, iv) D_2 and CO_2 traces for $\text{Mn}_3\text{O}_4/\text{Na}_2\text{CO}_3$; and (v, vi) D_2 and CO_2 traces for $\text{Mn}_3\text{O}_4/\text{K}_2\text{CO}_3$.

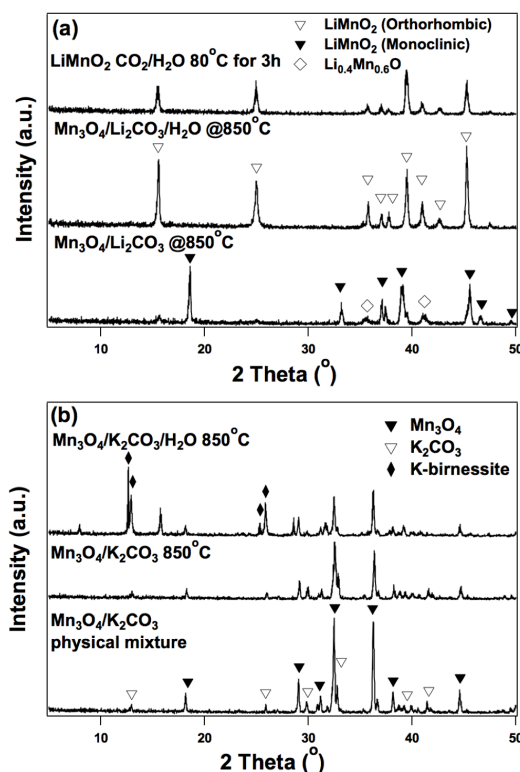


Figure 7-2 Powder X-ray diffraction (XRD) patterns identify intermediate phases in reaction of Mn_3O_4 with alkali carbonates (molar ratio 2:3) under various conditions. (a) Mixture of Mn_3O_4 and Li_2CO_3 heated to 850 °C before (bottom trace) and after (middle trace) the introduction of water. The top trace shows the diffraction pattern of the solid recovered after hydrolyzing LiMnO_2 in an aqueous suspension at 80 °C with CO_2 bubbling through for 3h. (b) Physical mixture of Mn_3O_4 and Li_2CO_3 at room temperature (bottom trace) and heated to 850 °C prior (middle trace) and after (top trace) the introduction of water.

Hydrogen evolution is observed for $\text{Mn}_3\text{O}_4/\text{Li}_2\text{CO}_3$ and $\text{Mn}_3\text{O}_4/\text{Na}_2\text{CO}_3$ at or below 850°C , but not for $\text{Mn}_3\text{O}_4/\text{K}_2\text{CO}_3$ (Figure 7-1b). The solid after the thermal treatment described in Figure 7-1a was cooled down to 200°C , and exposed to a second temperature ramp-and-hold treatment to 850°C in $\text{D}_2\text{O}/\text{Ar}$ (5%/95%). D_2 evolution is detected from $\sim 540^\circ\text{C}$ and peaks at $\sim 645^\circ\text{C}$ and for $\text{Mn}_3\text{O}_4/\text{Li}_2\text{CO}_3$ (trace i in Figure 7-1b). Little CO_2 is produced during reaction (trace ii in Figure 7-1b), indicating most of the Li_2CO_3 has reacted with Mn_3O_4 during thermal treatment prior to water introduction. Based on the XRD data, only the orthorhombic LiMnO_2 phase is present after the hydrogen evolution reaction, suggesting all Mn(II) in Mn_3O_4 has been oxidized to Mn(III) (middle trace in Figure 7-2a). D_2 evolution occurs at 850°C on $\text{Mn}_3\text{O}_4/\text{Na}_2\text{CO}_3$ (trace iii in Figure 7-1b), and the maximum rate of hydrogen evolution at 850°C is only 1/50 of that for $\text{Mn}_3\text{O}_4/\text{Li}_2\text{CO}_3$ (an indication that Li_2CO_3 is more active in promoting the hydrogen evolution reaction than Na_2CO_3). The concurrent evolution of CO_2 with hydrogen suggests that not all the Na_2CO_3 is consumed in the reaction with Mn_3O_4 prior to the water introduction, and this result is consistent with our previous study.¹ In addition, the fact that the ratio of the amount of CO_2 produced before and after water introduction is very close to 2 indicates that Na_2CO_3 extracts all Mn(III) in Mn_3O_4 but is unable to react with the Mn(II) species in the absence of water.¹ $\alpha\text{-NaMnO}_2$ is formed as the only solid product after the hydrogen evolution reaction.¹ No detectable amount of hydrogen is produced for $\text{Mn}_3\text{O}_4/\text{K}_2\text{CO}_3$, suggesting no oxidation of Mn(II) has taken place. CO_2 is observed at 850°C in the presence of water, and its amount is roughly equal to that expected from the total decomposition of K_2CO_3 . Unreacted Mn_3O_4 and K-birnessite are identified after reacting with water at 850°C by XRD. However, not all peaks in the XRD pattern are accounted for, partly due to the hygroscopic nature of the powder, which forms a wet layer during the time taken to collect one powder XRD measurement ($\sim 20\text{min}$).

Li cation removal from LiMnO_2 cannot be achieved under similar conditions to that of sodium cation removal from $\alpha\text{-NaMnO}_2$, *i.e.* stirring in an aqueous suspension at 80°C with CO_2 bubbling through for 3h (henceforth referred to as water/ CO_2 treatment). We showed in our previous work that Na cation could be completely extracted from $\alpha\text{-NaMnO}_2$ via the water/ CO_2 treatment. In contrast, the XRD patterns of LiMnO_2 before and after the water/ CO_2 treatment are very similar (top and middle traces, Figure 7-2a), suggesting that little Li cation has been removed from LiMnO_2 . Moreover, no detectable amount of O_2 was observed when the water/ CO_2 treated LiMnO_2 was subjected to a temperature ramp-and-hold procedure to 850°C in Ar (confirms the lack of Li cation removal during the water/ CO_2 treatment).

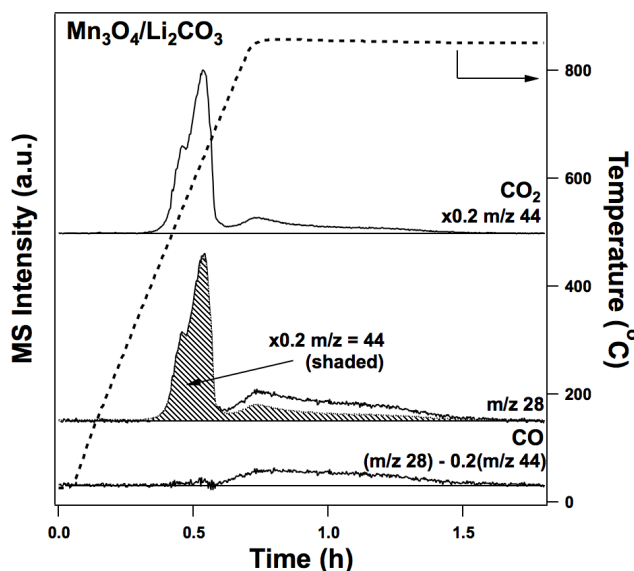


Figure 7-3 Mass fragmentation analysis shows CO_2 is reduced to CO when reacting with Mn_3O_4 and Li_2CO_3 .

A fraction of CO_2 formed from the reaction of Mn_3O_4 with Li_2CO_3 is reduced to CO during the temperature ramp-and-hold to 850°C in the absence of water, but not for Na_2CO_3 or K_2CO_3 . For both $\text{Mn}_3\text{O}_4/\text{Li}_2\text{CO}_3$ and $\text{Mn}_3\text{O}_4/\text{Na}_2\text{CO}_3$, all Mn(II) species in Mn_3O_4 are oxidized to Mn(III) in LiMnO_2 and $\alpha\text{-NaMnO}_2$, respectively, after reacting with water at 850°C (Figure 7-1b). The amount of D_2 produced from $\text{Mn}_3\text{O}_4/\text{Na}_2\text{CO}_3$ is within experimental error ($\pm 10\%$) of the theoretical maximum amount; whereas only $\sim 70\%$ of the stoichiometric amount of D_2 was

detected for $\text{Mn}_3\text{O}_4/\text{Li}_2\text{CO}_3$. Quantitative mass spectrometric analysis shows that the remaining $\sim 30\%$ of Mn(II) is oxidized by the CO_2 released during the reaction between Mn_3O_4 and Li_2CO_3 prior to the introduction of water, producing CO (Figure 7-3). In addition to the parent ion of CO_2 (m/z 44), m/z 28 signal is detected as a cracking fragment of CO_2 . For pure CO_2 , the m/z 28 signal should theoretically trace the parent ion (m/z 44) signal, differing only by a scaling factor.³ It is clear from Figure 7-3 that m/z 28 traces exactly m/z 44 by a factor of ~ 0.2 at temperatures below 685°C , beyond which the two traces deviate significantly from each other. The difference in the two traces at temperature above 685°C is attributed to CO produced from the reaction of CO_2 with the Mn(II) species .

Fe_3O_4 and alkali carbonates (Li_2CO_3 , Na_2CO_3 and K_2CO_3)

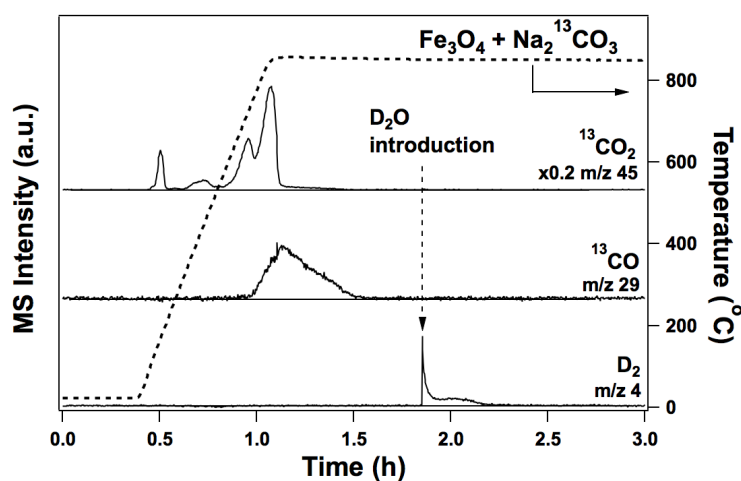


Figure 7-4 Reaction of Fe_3O_4 with $\text{Na}_2^{13}\text{CO}_3$ confirms reduction of $^{13}\text{CO}_2$ to ^{13}CO prior to the introduction of water.

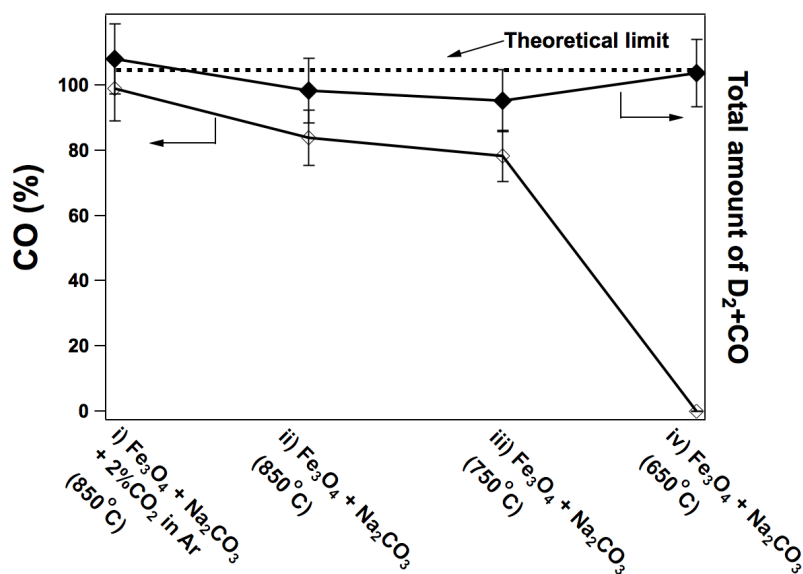


Figure 7-5 Percentage of CO of the reduction products (H₂ and CO) and total amount of H₂ and CO formed when the physical mixture of Fe₃O₄/Na₂CO₃ (molar ratio 2:3) reacts i) at 850°C with 2% CO₂ in the carrier gas (Ar); ii) at 850°C in Ar; iii) at 750°C in Ar; and iv) at 650°C in Ar. D₂O was introduced in ii), iii) and iv) after the completion of CO₂ evolution from the decomposition of Na₂CO₃ to oxidize the remaining Fe(II) species to Fe(III). The dashed line shows the theoretical maximum amount of H₂ and CO can be formed per mole of Mn.

Both hydrogen evolution and CO₂ reduction reactions occur on Fe₃O₄/Na₂CO₃ at or below 850°C (Figure 7-4). Na₂¹³CO₃, rather than Na₂¹²CO₃, was used to differentiate the contribution of CO produced from the carbonate and the CO₂ in the feed. Three ¹³CO₂ evolution peaks are observed during the temperature ramp-and-hold to 850°C for Fe₃O₄/Na₂¹³CO₃ (molar ratio of 2:3) in Ar. The peak at 165°C is likely from the decomposition of a sodium bicarbonate impurity in the sodium carbonate, whereas the two main ¹³CO₂ evolution peaks at 725 and 850°C are attributed to the reaction of Fe₃O₄ with Na₂¹³CO₃. MS signal for ¹³CO (m/z 29, corrected for the contribution from the cracking fragment of ¹³CO₂) starts to rise at 735°C, and peaks at 850°C before returning to the baseline. When D₂O is introduced at 850°C, a sharp D₂ evolution peak is observed, indicating not all Fe(II) in Fe₃O₄ has been oxidized by CO₂. Approximately 85% and 15% of Fe(II) is oxidized by ¹³CO₂ and D₂O, respectively. Replacing Na₂¹³CO₃ with Na₂¹²CO₃ in the initial solid mixture yielded very similar results. Since the molar ratio of the starting mixture of Fe₃O₄/Na₂CO₃ is 2:3, the total amount of CO₂ released from

Na_2CO_3 is 3 times that needed to fully oxidize all the Fe(II) in Fe_3O_4 . The fact that ~85% of Fe(II) is oxidized indicates that close to 30% CO_2 is consumed in reduction reaction. Approximately 80% of the Fe(II) is oxidized by CO_2 (produced from the reaction between Fe_3O_4 and Na_2CO_3) during the temperature ramp-and-hold to 750°C in Ar. The onset of CO evolution occurs at $\sim 735^\circ\text{C}$ (Figure 7-4), whereas water oxidizes Fe(II) to Fe(III) with the stoichiometric production of hydrogen at as low as 560°C (Table 7-1). The remaining Fe(II) after the completion of CO_2 evolution from the decomposition of carbonates can then be oxidized to Fe(III) by water via hydrogen evolution reaction. Therefore, the temperature of thermal treatment of $\text{Fe}_3\text{O}_4/\text{Na}_2\text{CO}_3$ can be used to control the reaction pathway for the oxidation of Fe(II) (Figure 7-5).

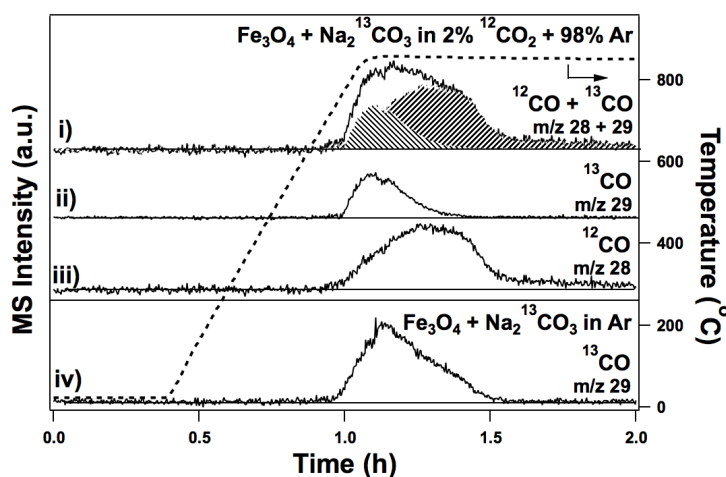


Figure 7-6 CO_2 reduction with $\text{Fe}_3\text{O}_4/\text{Na}_2^{13}\text{CO}_3$ in the presence (i, ii) and iii) and absence (iv)) of $^{12}\text{CO}_2$ in the feed.

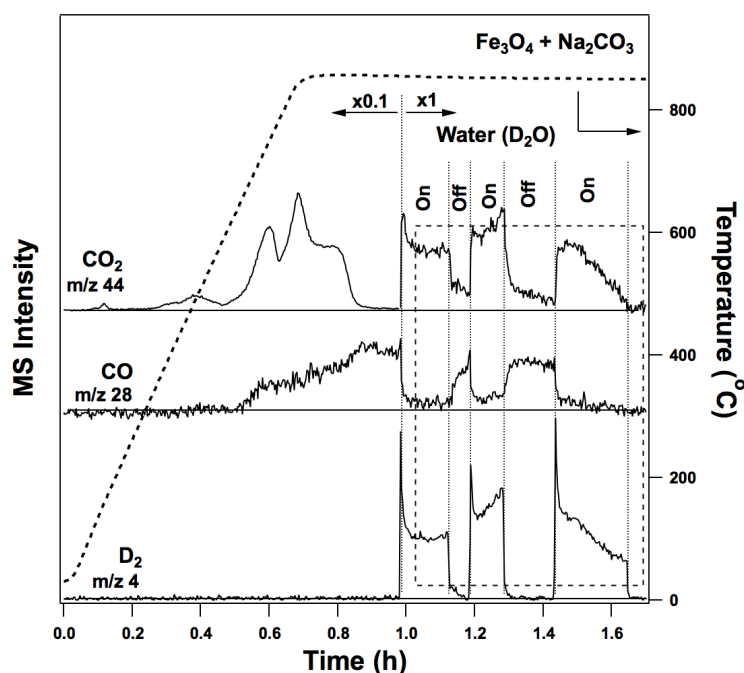


Figure 7-7 Water pulse experiments show the relative concentration of CO_2 and water controls the contribution of hydrogen evolution and CO_2 reduction over Fe_3O_4 and Na_2CO_3 . The part of the data enclosed in the box is used for the product distribution analysis.

All the Fe(II) is oxidized to Fe(III) by CO_2 during the temperature ramp-and-hold to 850°C in CO_2/Ar (2%/98%) (Figure 7-5), producing a stoichiometric amount of CO . This result suggests that the incomplete oxidation of Fe(II) during the temperature ramp-and-hold procedure conducted in Ar is caused by the limited supply of CO_2 . This speculation is also supported by the observation that the MS signals for ^{13}CO and $^{13}\text{CO}_2$ decrease simultaneously (Figure 7-4). In order to deconvolute the contributions of the CO_2 that evolves from the decomposition of the Na_2CO_3 and the CO_2 in the carrier gas in the CO_2 reduction reaction, $\text{Fe}_3\text{O}_4/\text{Na}_2^{13}\text{CO}_3$ was subjected to a temperature ramp-and-hold to 850°C in a $^{12}\text{CO}_2/\text{Ar}$ (2%/98%) atmosphere (Figure 7-6). The onset of the ^{13}CO and ^{12}CO peaks occurs at similar temperature ($\sim 735^\circ\text{C}$). The majority of the reduction product initially is ^{13}CO , suggesting $^{13}\text{CO}_2$ from $\text{Na}_2^{13}\text{CO}_3$ is preferentially reduced. It is likely that the proximity of the newly formed $^{13}\text{CO}_2$ to the Fe(II) species plays a key role. ^{12}CO becomes the dominant reduction product after $^{13}\text{CO}_2$ is exhausted. ^{13}CO accounts for approximately 30% of the reduction product and

remainder is ^{12}CO , with the total amount being close to the amount required to fully oxidize all Fe(II) to Fe(III) (within $\pm 10\%$).

Hydrogen evolution or CO_2 reduction reaction pathways can be controlled (reversibly) by tuning the relative concentrations of CO_2 and water. Upon the introduction of the first D_2O pulse to $\text{Fe}_3\text{O}_4/\text{Na}_2\text{CO}_3$ at 850°C , the rate of CO production instantaneously decreases by more than a factor of 10, and D_2 evolution is observed (Figure 7-7). In addition, the CO_2 concentration also spikes upon D_2O introduction, indicating less CO_2 is consumed in the reduction reaction. The reverse occurs when the D_2O pulse stops, *i.e.*, CO production recovers instantaneously and the D_2 signal decreases to baseline. The pathway for oxidizing Fe(II) to Fe(III) can be controlled by the relative amounts of CO_2 and water present until the Fe(II) species is exhausted.

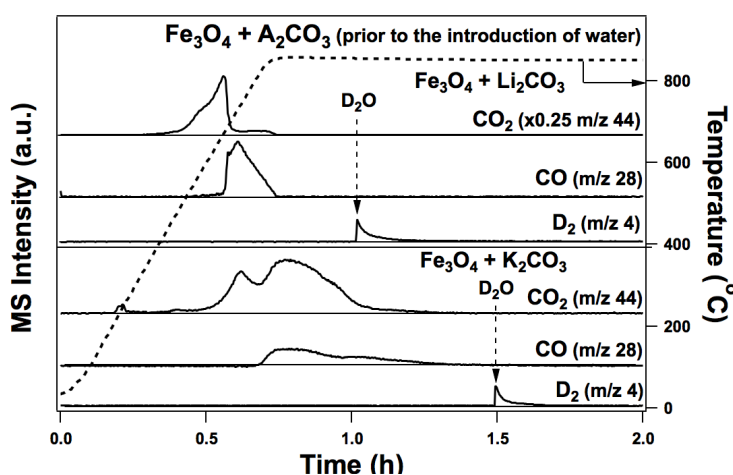


Figure 7-8 Reactions of Fe_3O_4 with Li_2CO_3 and K_2CO_3 show both CO_2 reduction and hydrogen evolution.

CO_2 reduction and hydrogen evolution reactions also take place on $\text{Fe}_3\text{O}_4/\text{Li}_2\text{CO}_3$ and $\text{Fe}_3\text{O}_4/\text{K}_2\text{CO}_3$ (Figure 7-8). The CO evolution during the temperature ramp-and-hold to 850°C in Ar starts at 680 and 815°C for $\text{Fe}_3\text{O}_4/\text{Li}_2\text{CO}_3$ and $\text{Fe}_3\text{O}_4/\text{K}_2\text{CO}_3$, respectively. Water (D_2O) was introduced at 850°C after the CO signal returns to baseline, and the amounts of D_2 produced account for approximately 20% and 10% of the Fe(II) in $\text{Fe}_3\text{O}_4/\text{Li}_2\text{CO}_3$ and

$\text{Fe}_3\text{O}_4/\text{K}_2\text{CO}_3$ respectively. The temperatures for the onset of the D_2 evolution for Fe_3O_4 and carbonates during the temperature ramp-and-hold in $\text{D}_2\text{O}/\text{Ar}$ (5%/95%) are all around 500°C .

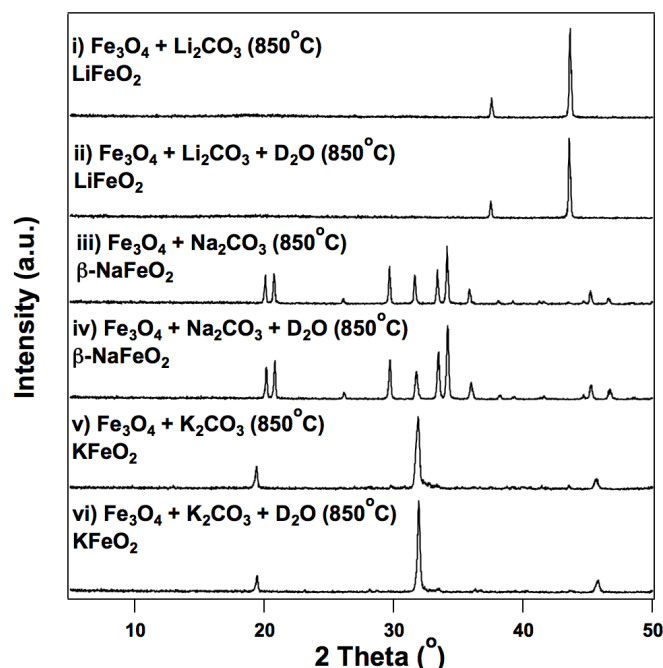


Figure 7-9 X-ray diffraction patterns of solids collected after reacting the physical mixture of Fe_3O_4 and alkali carbonates in the absence and presence of D_2O at 850°C .

The powder XRD patterns show only the AFeO_2 ($\text{A} = \text{Li}, \text{Na}$ and K) phases after the temperature ramp-and-hold to 850°C in Ar (Figure 7-9). These results are consistent with the observation that 80% or more of the Fe(II) in Fe_3O_4 is oxidized to Fe(III) by the CO_2 from the carbonates. No detectable change was observed for the solids collected before and after the introduction of water at 850°C for all Fe_3O_4 and alkali carbonate systems.

Sodium and potassium can be removed from the iron oxide structure via the water/ CO_2 treatment, resulting in an amorphous Fe_2O_3 phase, whereas Li cation removal from LiFeO_2 cannot be achieved by the water/ CO_2 treatment.

Co_3O_4 and alkali carbonates (Li_2CO_3 , Na_2CO_3 and K_2CO_3)

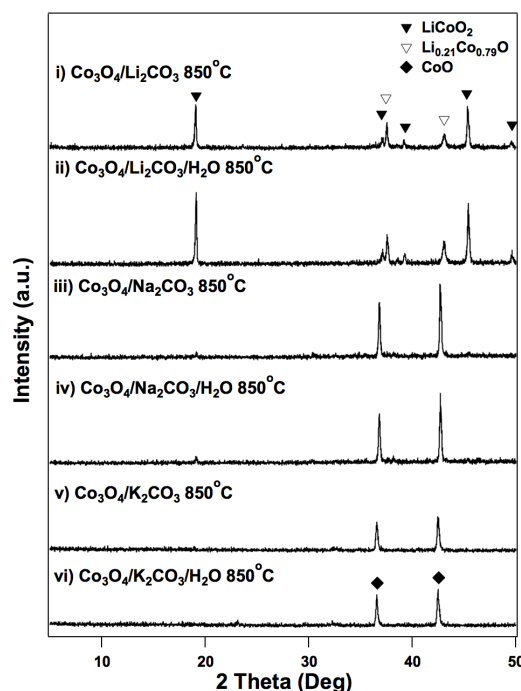


Figure 7-10 Powder X-ray diffraction patterns of the solid collected after reacting Co_3O_4 with Li_2CO_3 , Na_2CO_3 and K_2CO_3 at 850°C in the absence (i), iii) and v), respectively) and presence (ii), iv) and vi), respectively) of water.

No CO_2 reduction was observed during the temperature ramp-and-hold to 850°C for Co_3O_4 with all three alkali carbonates (Li_2CO_3 , Na_2CO_3 and K_2CO_3) in Ar; nor did hydrogen evolution occur upon the introduction of D_2O at 850°C . However, Co_3O_4 does react with Li_2CO_3 during the temperature ramp to 850°C , as evidenced by the LiCoO_2 and $\text{Li}_{0.21}\text{Co}_{0.79}\text{O}$ phases identified by powder XRD measurement of the solid collected after the thermal treatment (Figure 7-10) and the sharp CO_2 evolution peak at 575°C (Figure 7-11). A CO_2 evolution peak occurs at $\sim 850^\circ\text{C}$ and has a long tail for both $\text{Co}_3\text{O}_4/\text{Na}_2\text{CO}_3$ and $\text{Co}_3\text{O}_4/\text{K}_2\text{CO}_3$ mixtures during the temperature ramp-and-hold procedure. The total amount of CO_2 evolved is closed to that expected for total decomposition of Na_2CO_3 and K_2CO_3 . No sodium or potassium-containing phase is identified by XRD after the temperature and hold procedure for $\text{Co}_3\text{O}_4/\text{Na}_2\text{CO}_3$ and $\text{Co}_3\text{O}_4/\text{K}_2\text{CO}_3$, also suggesting the total decomposition of the carbonates. The lack of crystalline sodium or potassium containing phases might be attributed to the hygroscopic nature of sodium and potassium oxides and hydroxides. The X-ray diffraction

patterns show little change after the introduction of water at 850°C for all alkali carbonates, consistent with the lack of hydrogen evolution.

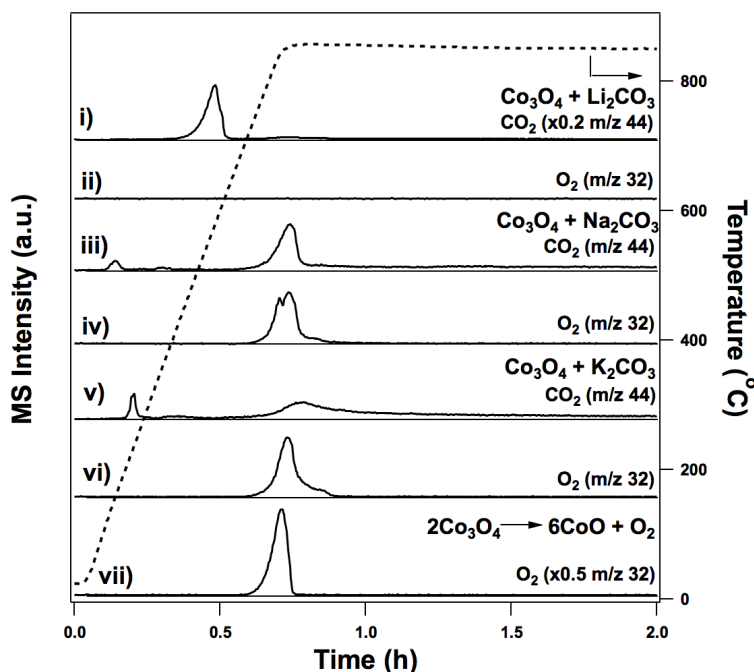


Figure 7-11 Reaction of Co_3O_4 with Li_2CO_3 (i) and ii)), Na_2CO_3 (iii) and iv)) and K_2CO_3 (v) and vi)) during the temperature ramp and hold procedure to 850°C in Ar. vii) shows the control experiment of thermal reduction of Co_3O_4 to CoO , releasing O_2 .

Thermal reduction of the metal oxides

After removing alkali cation from the metal oxide structure, the solids are subject to temperature ramp-and-hold procedures in Ar to thermally reduce to the spinel oxides (Figure 7-12). The alkali cation extracted Mn(III) and Fe(III) oxides are fully reduced to Mn_3O_4 and Fe_3O_4 at 850 and 1150°C, respectively, similar to the temperatures for thermal reduction of Mn_2O_3 and Fe_2O_3 . Co_3O_4 is reduced to CoO during the temperature ramp of the $\text{Co}_3\text{O}_4/\text{Na}_2\text{CO}_3$ mixture to 850°C, as evidenced by the powder XRD measurement and the O_2 evolution peak at ~850°C for pure Co_3O_4 .

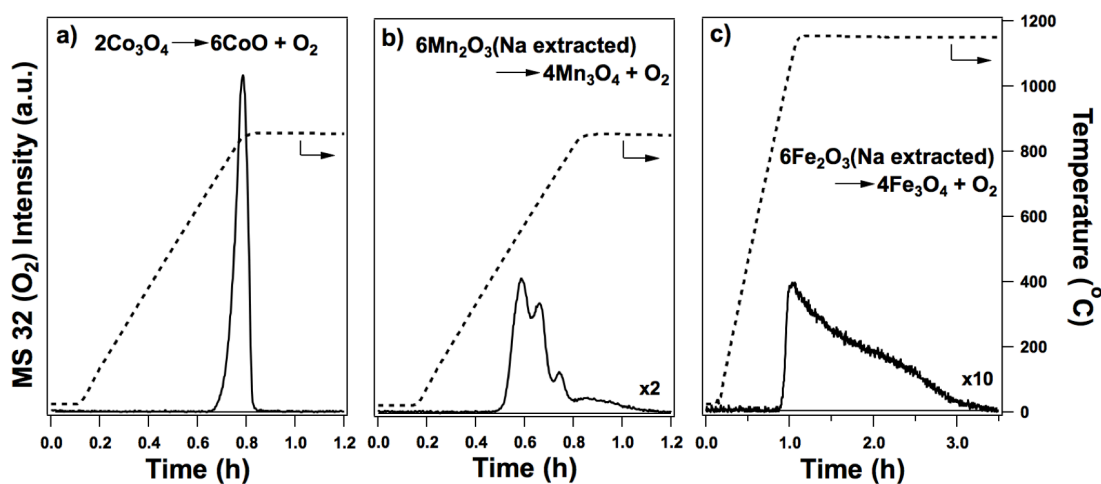


Figure 7-12 Thermal reduction of a) Co_3O_4 , b) Na ion extracted Mn_2O_3 and c) Na ion extracted Fe_2O_3 .

7.4 Discussion

Comparison of reactivity among alkali carbonates

The ability of alkali carbonates to promote hydrogen evolution and CO_2 reduction with a given metal oxide that has a spinel structure follows the descending order: $\text{Li}_2\text{CO}_3 > \text{Na}_2\text{CO}_3 > \text{K}_2\text{CO}_3$ (e.g., evaluated by the onset temperatures for hydrogen evolution and CO_2 reduction reactions on various combinations of Mn_3O_4 and alkali carbonates (Table 7-1)). D_2 started to evolve on $\text{Li}_2\text{CO}_3/\text{Mn}_3\text{O}_4$ at 540°C , and in contrast no detectable amount of D_2 was observed on $\text{Na}_2\text{CO}_3/\text{Mn}_3\text{O}_4$ until 850°C . In addition, the peak rate of D_2 evolution on $\text{Li}_2\text{CO}_3/\text{Mn}_3\text{O}_4$ is ~ 50 times that measured from $\text{Na}_2\text{CO}_3/\text{Mn}_3\text{O}_4$. No D_2 evolution is detected for $\text{K}_2\text{CO}_3/\text{Mn}_3\text{O}_4$ at reaction temperature up to 850°C . For the CO_2 reduction reaction, the onset temperatures for CO evolution are 675 , 735 and 805°C for $\text{Li}_2\text{CO}_3/\text{Fe}_3\text{O}_4$, $\text{Na}_2\text{CO}_3/\text{Fe}_3\text{O}_4$ and $\text{K}_2\text{CO}_3/\text{Fe}_3\text{O}_4$, respectively, further confirming the trend in reactivity for the carbonates investigated. Reactivities of various combinations of spinel metal oxides and alkali carbonates for hydrogen evolution and CO_2 reduction reactions are summarized in Figures 7-13 and 17-14.

Water splitting @850°C	Fe ₃ O ₄	Mn ₃ O ₄	Co ₃ O ₄
Li ₂ CO ₃	✓	✓	✗
Na ₂ CO ₃	✓	✓	✗
K ₂ CO ₃	✓	✗	✗

Figure 7-13 Summary of the combinations of spinel metal oxides and alkali carbonates for hydrogen evolution reaction at 850°C.

Table 7-1. Onset temperatures for hydrogen evolution and CO₂ reduction reactions

Sample	Onset temperature (°C)		
	CO ₂	D ₂	CO
Mn ₃ O ₄ /Li ₂ CO ₃	400	540	685
Mn ₃ O ₄ /Na ₂ CO ₃	515	850	-
Mn ₃ O ₄ /K ₂ CO ₃	-	-	-
Fe ₃ O ₄ /Li ₂ CO ₃	375	510	675
Fe ₃ O ₄ /Na ₂ CO ₃	385	500	735
Fe ₃ O ₄ /K ₂ CO ₃	445	500	805

Comparison of reactivity among the spinel metal oxides

CO ₂ reduction @850°C	Fe ₃ O ₄	Mn ₃ O ₄	Co ₃ O ₄
Li ₂ CO ₃	✓	✓	✗
Na ₂ CO ₃	✓	✗	✗
K ₂ CO ₃	✓	✗	✗

Figure 7-14 Summary of the combinations of spinel metal oxides and alkali carbonates for CO₂ reduction reaction at 850°C

The reactivity for hydrogen evolution and CO₂ reduction reactions of spinel metal oxides with a given alkali carbonate follows the descending order: Fe₃O₄ > Mn₃O₄ > Co₃O₄. Hydrogen evolution occurs on Fe₃O₄ with all three alkali carbonates, whereas Mn₃O₄ must be combined with the more reactive carbonates, Li₂CO₃ and Na₂CO₃ for activity to be observed. For Co₃O₄, hydrogen evolution does not occur even when it is combined with the most reactive lithium carbonate. This reactivity trend is more pronounced for the CO₂ reduction reaction, which occurs on all Fe₃O₄ containing sample with alkali carbonates. In contrast, only when Mn₃O₄ combined with lithium carbonate, can CO evolution be detected. None of the Co₃O₄ containing samples is active for CO₂ reduction at or below 850°C.

Comparison of ion extraction and thermal reduction of metal oxides

The extraction of alkali cations from the alkali metal(III) oxides is key to being able to close the thermochemical cycle at reasonable temperatures (<1000°C), since alkali metal(III) oxides cannot easily be thermally reduced (<1500°C). The degree of difficulty for alkali cation extraction parallels the reactivity of the corresponding alkali carbonates: Li⁺ > Na⁺ > K⁺. No appreciable lithium extraction is observed for LiFeO₂ and LiMnO₂, whereas almost complete sodium extraction can be achieved for both NaFeO₂ and NaMnO₂ (Figure 7-15). Furthermore,

complete potassium cation removal can also be achieved by the water/CO₂ treatment from KFeO₂.

Alkali ion extraction @80°C (aq.)	Fe ₃ O ₄	Mn ₃ O ₄	Co ₃ O ₄
Li ₂ CO ₃	X	X	NA
Na ₂ CO ₃	✓	✓	NA
K ₂ CO ₃	✓	NA	NA

Figure 7-15 Summary of alkali ion extraction from the alkali metal salts formed in the hydrogen evolution reaction in an aqueous suspension at 80°C in the presence of CO₂.

Tuning the operating temperature of thermochemical cycles

A general tradeoff exists between the temperatures of oxidation (M(II) → M(III)) and reduction (M(III) → M(II)) reactions of the metal species in the thermochemical cycles: the lower the reaction temperature in one direction accompanies by the higher reaction temperature of the other direction. This is analogous to the case of redox pairs in solution phase: the less stable the oxidized species is, the more stable the reduced species is, and *vice versa*. In turn, more external energy input, *e.g.* electricity or heat, is required to convert the more stable species to the less stable one. Since heat is the only energy source for thermochemical cycles, higher temperature is generally needed to promote energetically unfavorable reactions, *e.g.* thermal reduction of metal oxides. The relatively high thermal reduction temperature (~1150°C) of Fe₂O₃ to Fe₃O₄ indicates that Fe(III) is more stable than Fe(II) below 1150°C, which suggests the oxidation of Fe(II) to Fe(III) should occur at relatively low temperature. Indeed, both hydrogen evolution and CO₂ reduction reactions occur on all Fe₃O₄-based systems at or below 850°C. In contrast, the relative low thermal reduction temperature of Co₃O₄ to CoO

(680-850°C) suggests that Co(II), rather than Co(III), is the more stable species at this temperature range. Therefore, it is not surprising that none of the Co_3O_4 based systems are active for hydrogen evolution or CO_2 reduction reactions. Whether and at what temperature a thermochemical cycle can be closed is primarily determined by the step that converts the more stable to the less stable phase, *e.g.* thermal reduction of Fe_2O_3 . The lowest operating temperature for a thermochemical cycle should be reached when stability of the oxidized and reduced phases is comparable. The Mn_3O_4 -based cycle falls in that category, as the hydrogen evolution and thermal reduction reactions both occur at $\sim 850^\circ\text{C}$.

7.5 Conclusions

Low-temperature thermochemical cycles for water splitting and CO_2 reduction involving spinel metal oxides and alkali carbonates were investigated. The reactivity sequence for hydrogen evolution reaction of metal oxides with a given alkali carbonate is: $\text{Fe}_3\text{O}_4 > \text{Mn}_3\text{O}_4 > \text{Co}_3\text{O}_4$; whereas that of alkali carbonates with a given metal oxide is: $\text{Li}_2\text{CO}_3 > \text{Na}_2\text{CO}_3 > \text{K}_2\text{CO}_3$. Hydrogen evolution and CO_2 reduction reactions occur at lower temperature on more reactive metal oxide and alkali carbonate combinations; however, thermal reduction temperature is higher and the alkali ion extraction is more difficult for more active metal oxide and alkali carbonate, respectively. $\text{Mn}_3\text{O}_4/\text{Na}_2\text{CO}_3$ appears to be the best combination in that the temperatures required for hydrogen evolution and thermal reduction of metal oxide are similar. In addition, complete alkali ion extraction can be achieved for the $\text{Mn}_3\text{O}_4/\text{Na}_2\text{CO}_3$ combination.

7.6 Bibliography

- (1) Xu, B.; Bhawe, Y.; Davis, M. E. *Proceedings of the National Academy of Sciences* **2012**,

109, 9260–9264.

- (2) Kreider, P. B.; et al. *International Journal of Hydrogen Energy* **2011**, 36, 7028–7037.
- (3) Xu, B.; Madix, R. J.; Friend, C. M. *J. Am. Chem. Soc.* **2010**, 132, 16571–16580.

Chapter 8 Conclusions from Materials for thermochemical cycles

8.1 Conclusions from impregnated clusters

Chapters 2-4 of this thesis work looked at the feasibility of closing a thermochemical water splitting cycle using active metal particles impregnated on an inert zeolite support. There are two key findings from these chapters, both of which help in the understanding of stoichiometric redox reactions occurring on metal particles.

First, it was shown that experimentally, changing the particle size could change the thermodynamics of redox reactions occurring on particles of metal oxides. This was shown through two different systems, the reduction of CuO particles, and the oxidation of FeO particles. In both of these cases, the minimum temperature of the reaction was lowered when transitioning from bulk metal oxides to particles impregnated in the pores of Si-*BEA. The reduction temperature was lowered much more for CuO than the oxidation temperature for FeO. Thus, for reactions that involve steps with complete oxidation or reduction of metal oxide particles, reducing the particle size is advantageous.

Second, it was shown, that given the flow conditions under which the reaction is typically carried out, a two-step thermochemical water splitting cycle could not be closed under 1000°C. It was shown using first principles thermodynamic analysis, that for $\Delta\Delta S_{Red-Ox}^\theta$ and $\Delta\Delta H_{Red-Ox}^\theta$ that are expected for common metal oxides, that it would be thermodynamically unfeasible to close the cycle under 1000°C. It was at this point that multiple-step cycles (such as the spinel cycles) were explored to carry out thermochemical water splitting.

8.2 Conclusions from spinel structures

Chapters 6 & 7 showed in detail several materials that were capable of completing thermochemical cycles. Chapter 6 showed the first such cycle that was successfully tested as part of this thesis work, a cycle involving Na₂CO₃ and Mn₃O₄. The main figure detailing this

cycle is Figure 6-1. The rest of chapter 6{Xu:2012ix} was used to discuss and to prove how the entire cycle is completed, and the reaction sequence in each of the steps. Chapter 7 then looked at varying the metals in the cycle to try to find the optimum combination for the reactions in question. The sodium / manganese combination was optimal for water splitting, while the sodium / iron system was optimal for CO₂ reduction. The key drawback of these cycles is the step in which the alkali metal ion is extracted from the layered phase that is formed. In order to do the extraction, the solid has to be cooled down to room temperature, and immersed in liquid water in the presence of a flow of CO₂ in order to extract the alkali metal as the alkali metal carbonate. The solution is then dried to recover the alkali carbonate. This is extremely energy intensive, and undesirable for scale-up operations.

8.3 Recommendations for future work

The key suggestions for future work are to mitigate the energy requirements of the alkali-ion extraction stage of the thermochemical cycles presented thus far. This essentially presents an engineering challenge to find a route to extract the alkali ion (and replace it with a hydronium ion) without requiring a thermal cool down, and more importantly, without requiring the presence of liquid water. Several approaches were briefly experimented and abandoned as part of the thesis work on this thesis project, and these approaches could potentially be explored further.

First, supercritical CO₂ in the presence of vapor phase water could be used to try to extract the alkali metal as an alkali carbonate. This approach was attempted for the Na/Mn cycle, and while there was some extraction possible, the extraction wasn't to a degree desired for completion of the cycle. The experiment was conducted in a Teflon lined stainless-steel autoclave. One possible explanation for the incomplete extraction of the alkali metal from the layered structure is that the entire system reached an equilibrium state, and was unable to react

further. Thus, one possible way to explore this further is in a flow system in the presence of supercritical CO₂.

Second, a device can be envisioned with a sodium and proton permeable membrane in between a “sodium lean phase” and a “sodium rich phase”, and flows of water vapor, CO₂ and temperatures can be controlled such that the entire system allows the transmission of sodium in and out of the layered phase without energy inefficiencies. Again, this option was attempted as part of this thesis work, using Sodium β alumina as the sodium transporting membrane. However, the membrane suffers from insufficient physical strength. Any increase in the stress on the membrane causes the membrane to fracture, and allows gas flow across the membrane.

Thus, the future work would focus on trying to engineer a better setup for the Na₂CO₃/Mn₃O₄ system such that the system can be commercially implemented to capture waste heat. Special attention needs to be paid to the extraction of the alkali metal cation, as this step is currently the most energetically inefficient step in the entire cycle.

8.4 Introduction to the Methanol-to-Olefins (MTO) reaction

8.5 Motivation for the MTO reaction

As the reserves of petroleum in the world deplete, there is an ever-greater push to find alternative routes to existing petroleum-derived products. Apart from deriving transportation fuels, one of the largest uses of petroleum is for plastics production¹. Currently, ethylene, for example, is produced from steam cracking in the petrochemical industry¹. However, a large amount of research is going into finding alternative sources for these hydrocarbons.

There are many possible alternative routes to generate petrochemical products from non-petroleum sources (see figure 9-1). Highlighted in black are the existing routes to petrochemical products, through processing of crude oil. There is a growth in interest for conversion of biomass to petrochemical products through platform chemicals such as 5-

hydroxymethylfurfural^{2,4}. Biomass, and coal can be gasified under partial oxidation conditions⁵⁻⁷ while natural gas can be steam-reformed⁸ to yield syngas.

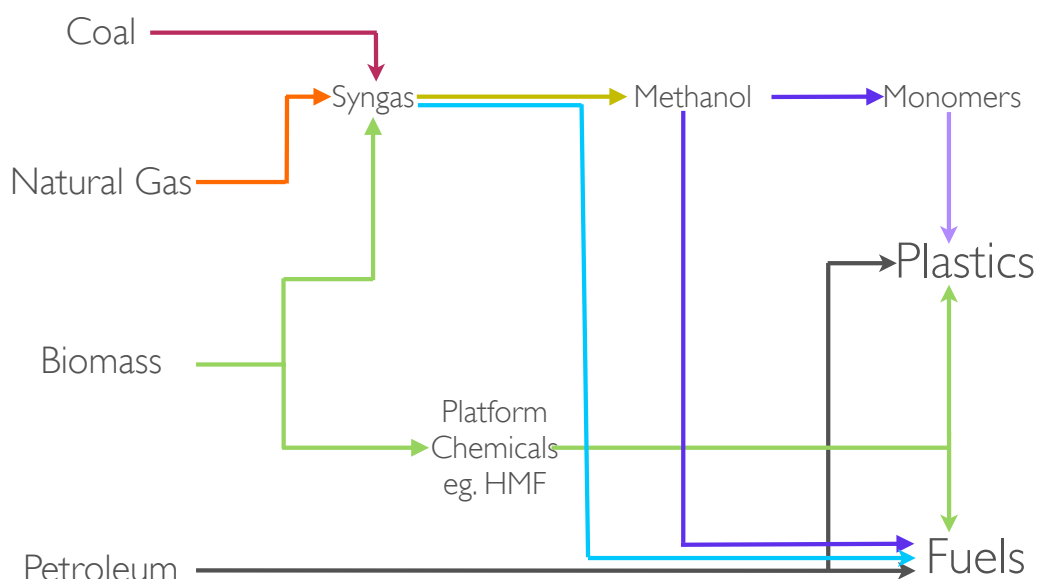


Figure 8-1 Overall scheme of alternative conversions

Syngas can then be used as a platform to yield the same set of hydrocarbons that can be obtained from petroleum through a variety of chemical conversions. First, syngas can be converted through Fisher-Tropsch chemistry to yield liquid hydrocarbons⁹ for fuels. Syngas can also be converted to methanol over copper / zinc oxide on alumina catalysts to yield methanol¹⁰. This is the route for commercial production of methanol.

This is where the methanol to hydrocarbons umbrella of chemistry becomes important. It uses methanol as a platform chemical to create longer chain hydrocarbons as well as shorter chain monomers for plastics production¹¹. It provides a route for the conversion of alternative carbon sources, such as biomass, to plastics and fuels through methanol as an intermediate.

The first reports of conversion of methanol to hydrocarbons come from Mobil¹². They involve the use of synthetic zeolite H-ZSM5 to convert methanol to a variety of hydrocarbons at 371°C with greater than 10% selectivity each to isobutane, propane, xylenes and toluene. They also report similar trends with higher carbon-number alcohols. The focus on conversion

to olefins came about due to the discovery and usage of silicoaluminophosphate type molecular sieves¹³. H-SAPO-34 was reported to convert methanol with greater than 80% selectivity by moles to ethylene and propylene, with trace amounts of butylene being formed. This structure greatly reduced the formation of aromatic species in the product stream from the reaction.

Since these early reports, a large number of structures and materials have been studied for their activity in the methanol-to-hydrocarbons, and methanol-to-olefins reactions¹¹. All of these reactions are conducted over microporous solid acids. Before continuing, a brief discussion of what these materials are is thus necessary.

8.6 Zeotype materials

Zeotype materials are a family of solid, crystalline materials formed from lattices comprised of $[\text{TO}_4]^{n-}$ tetrahedra connected through the oxygen atoms at the apex. The presence of bridging oxygens affords the creation of a wide array of lattices, with a variety of cavity, channel (pore) and connectivity features see figure 9-2. The tetrahedral atom, T, can have a wide range of valencies, from +2 (Zn) to +5 (P), creating a wide range of materials with varying chemical properties. If a material is comprised entirely of tetravalent atoms (Si, Ge) in the tetrahedral positions, the resulting framework is charge neutral. Substitution of these tetrahedral atoms with tetravalent atoms bearing empty orbitals generates Lewis acid sites. Di- and Tri-valent atoms like Zn, Al, Ga, Fe or In can also substitute in these tetravalent positions, forming a local negative charge (see figure 9-3). This negative charge acts as a site for cation exchange. When the exchanged cation is a proton it is a local Brønsted acid site. A common proxy of acid “concentration” is the ratio of tetravalent atoms to trivalent atoms in a zeolite structure (Si/Al for example). Finally, pentavalent atoms (such as P) can also fill the tetrahedral sites, however, special rules apply to the formation of these structures that will be discussed below. The most common group of materials has T being either silicon or aluminum, and is known as zeolites.

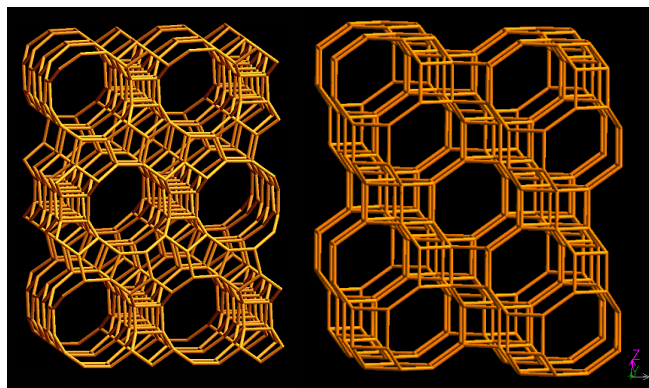


Figure 8-2 Examples of Zeotype Frameworks, *BEA (Left) and CHA (Right)¹⁴

Zeolites are tectosilicate materials with only Si or Al at the tetrahedral sites. The Swedish mineralogist Cronstedt first discovered zeolites in 1756. These materials have a wide variety of applications; they can be ion exchangers to soften water ¹⁵, they are used to trap water from organic solvents¹⁶ and last but not least, as catalysts¹⁷. Naturally, zeolites are formed under hydrothermal or sedimentary conditions in the presence of large quantities of alkali metal cations and silica-alumina. Naturally occurring zeolites tend to be rich in heteroatoms, allowing for large ion exchange capacities, but are often poor catalysts. Zeolites are now made synthetically for all the purposes they are commonly used for. A much larger variety of synthetic zeolite structures have been discovered through artificial synthesis and structure solution.

Zeolites are synthesized from a gel mixture comprised of a silica source, an organic or inorganic structure-directing agent, a mineralizing agent (fluoride or hydroxide ions) and water¹⁸. These gels are then heated to temperatures above the boiling point of water, where they are held for an extended length of time until solid crystals are formed. The release of the mineralizing agent into the supernatant liquid as a function of time is often used to monitor zeolite crystallization¹⁹. Typically, the crystal structure formed is checked by powder X-Ray Diffraction (XRD). Synthetic analogues of a large number of natural zeolites have been made with much more tunable structure compositions than available naturally.

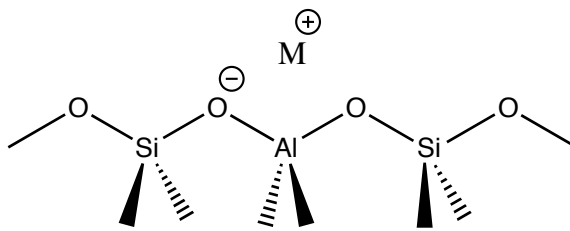


Figure 8-3 Schematic showing framework charge and balancing cation

The next biggest class of zeotype materials is known as aluminophosphates – AlPOs. Based on Lowenstein's rule²⁰ and empirical rules from Flanigen, Patton and Wilson²¹, these structures are formed from alternating $[\text{AlO}_4]$ and $[\text{PO}_4]$ tetrahedral. They can be isostructural with zeolites, eg: AlPO-34 and SSZ-13 both have the chabazite structure, and have acidity derived from incorporation of tetravalent (eg. Si, Sn, Ti) and divalent (eg. Zn, Co, Cr) atoms. The most common acidic aluminophosphate analogs are Silicoaluminophosphates, SAPOs. In these structures, the silicon atoms replace the phosphorous atoms to generate an acid site²¹. The bridging oxygen that bears the charge in a silicoaluminophosphate is very similar to the oxygen that bears the charge in a silicoaluminate material.

A lot of zeolite nomenclature has evolved to describe the frameworks that are often encountered in zeotype materials. Each framework in the synthetic molecular sieve community has been given a 3-letter code, such as MFI (**M**obil **F**ive) for H-ZSM-5, or CHA (**CH**Abazite) for chabazite-type materials. Further, the pores and channels encountered in a zeolite are often referred to by the number of tetrahedral atoms that comprise them. For example, in figure 9-4, the straight channel of the MFI structure has a 10-membered ring channel with the 10 tetrahedral atoms highlighted in red.

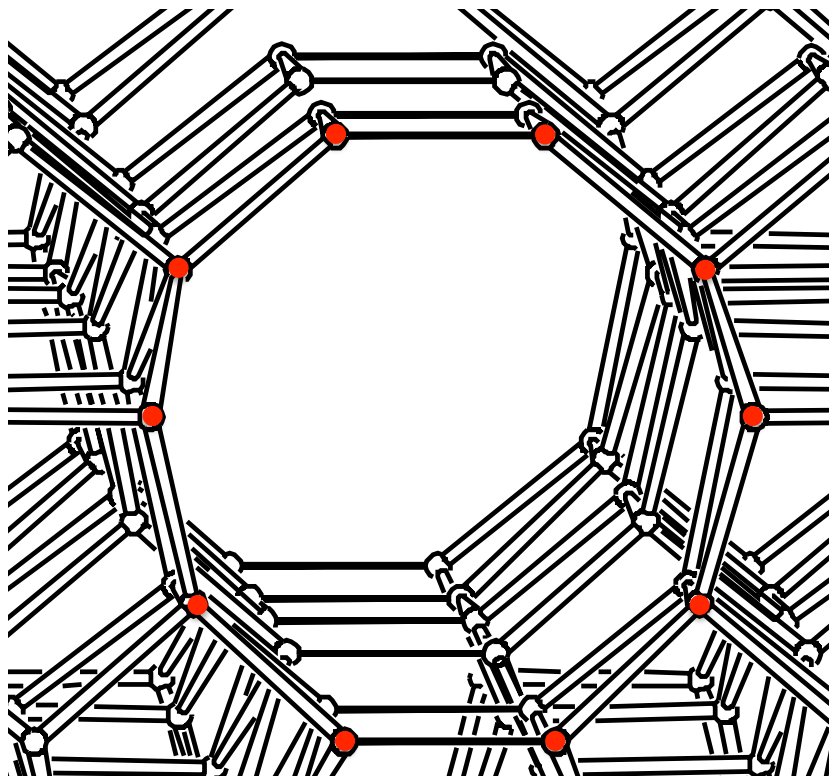


Figure 8-4 Straight Channel in MFI-type framework with the ten tetrahedral atoms highlighted

As mentioned previously, crystal structure confirmation and determination of zeolites and zeotype solids are typically done with X-ray Diffraction measurements. While this work does not detail the synthesis and crystal structure solution of a new material, this technique has been used in the characterization of all the materials that have been made for reaction testing, and the spectra obtained were compared with known spectra in the literature. Spectra were obtained with $\text{Cu-K}\alpha$ radiation on a Rigaku Miniflex II diffractometer. Elemental characterization of the materials was carried out using Energy-Dispersive Spectroscopy (EDS) using a JEOL JSM-6700F instrument equipped with an Oxford INCA Energy 300 X-ray Energy Dispersive Spectrometer.

Part 2 of this thesis focuses on utilizing zeolite and zeotype materials for understanding the structure-property relations on the Methanol-to-Olefins (MTO) reaction. As such, there is a large synthetic and characterization component associated with the catalytic testing of the materials. Where appropriate, synthetic and characterization details will be provided to discuss

how certain materials were made, treated and then tested for their conversions and selectivities in the MTO reaction.

8.7 Mechanisms for the Methanol-to-Hydrocarbons (MTH) reaction

The conversion of methanol to a mixture of hydrocarbons involves an intricate network of reactions. The exact mechanism through which the reaction proceeds is a subject of debate²²⁻²⁴. However, in the literature, there seems to be a consensus on the intermediates through which the reaction proceeds. Based on mechanistic studies in literature^{11,24,25}, the following general schematic (see figure 9-5) can be devised for the general methanol-to-hydrocarbons reaction.

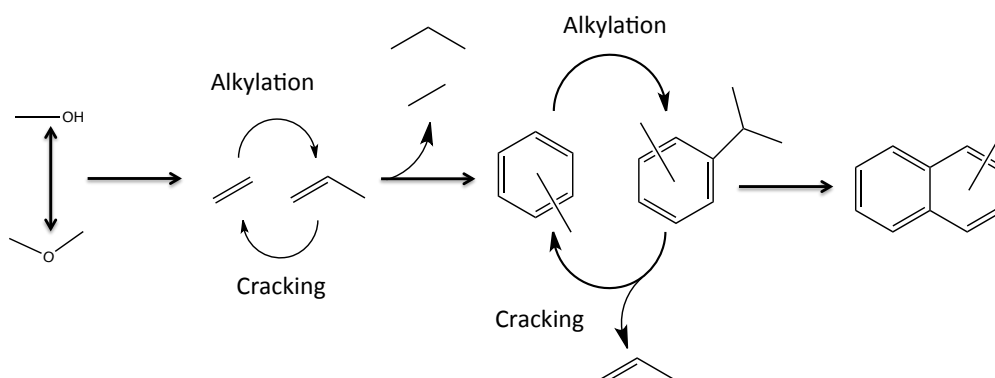


Figure 8-5 Schematic mechanism for methanol-to-hydrocarbons chemistry

This mechanism starts off with the equilibration of methanol with its dehydrated product – dimethyl ether. This equilibration can occur over weak acid sites, such as the Si-OH defect sites present in zeolite crystals, or at the crystal termini. This mixture is then further converted by strong acid sites to hydrocarbons. As such, either methanol or dimethyl ether can be used as the oxygenated carbon source for the reaction. All the experiments presented in this work were done with methanol as the input carbon source. However, there is a large exotherm associated with the dehydration of methanol^{11,26} that is not present if dimethyl ether is used as the carbon

source. There are literature reports²⁷ as well as reports of industrial processes for running the dehydration reaction in a separate reactor^{28,29} over an alumina based catalyst, and subsequent hydrocarbon formation in a separate reactor unit. This separation of the dehydration and hydrocarbon formation steps provides an engineering advantage of reducing the temperature rise of the process stream. However, these reports also present similar product distribution profiles from both methanol and dimethyl ether.

Over stronger acid sites, such as the acid sites in zeolites or SAPOs, the equilibrium mixture is then further converted to light olefins, such as ethylene and propylene, with the evolution of water as a byproduct. These olefins can either be left unconverted and evolved as products of the reaction, or be further converted. There are methylation and cracking sequences within the olefins that yield a variety of carbon-chain lengths in the products. The olefins can also react within themselves to yield aromatic compounds. The hydrogen evolved in the formation of these aromatic species is transferred to olefins to yield paraffins. The branches on the aromatic species can undergo further alkylation cracking sequences to yield short chain products. Thus, there are two simultaneous alkylation-cracking sequences in progress, one involving the olefins directly, the other involving branches off the aromatic groups¹¹.

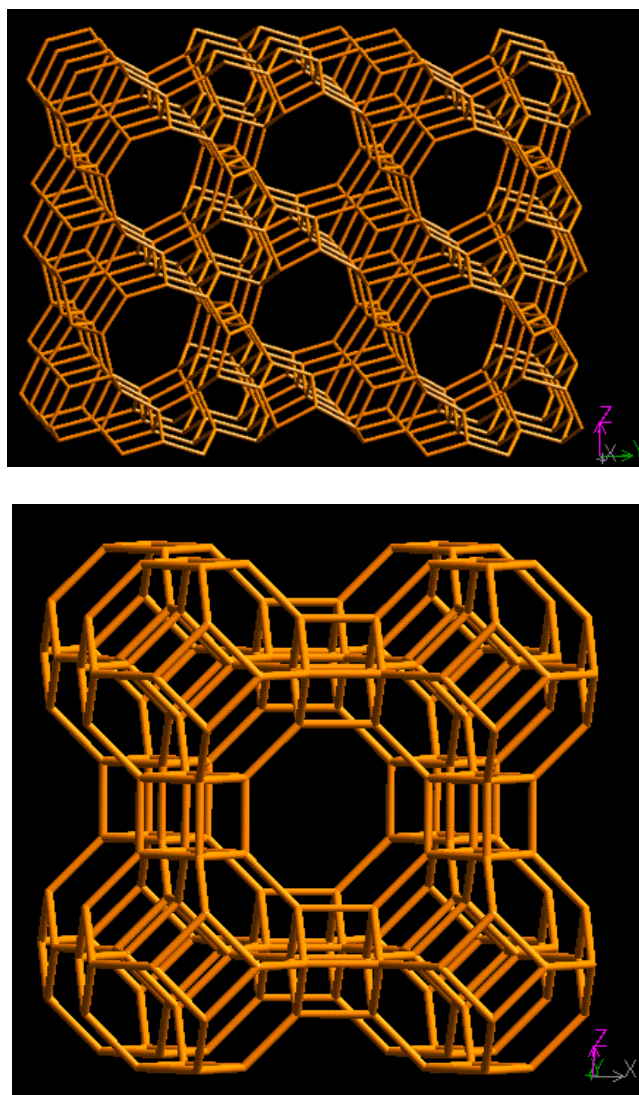


Figure 8-6 Schematic of structures that only contain channels (top) and structures that contain channels that open into cavities¹⁴² (bottom)

This is where the features of different structures create differences in the way that the reactions proceed. Figure 9-6 shows a schematic of two possible framework configurations. Frameworks that contain just channels through which molecules can flow, and frameworks that contain channels that open up into wider cavities. In order for the full range of intermediates to be formed, the structures need to have a certain minimum width of 5\AA (see below). The structures that contain channels wider than aromatic rings allow the aromatic products to escape the solid as organic products. However, the structures that have channels narrower than the cavities that they open into prevent these aromatic species from escaping. Consequently, the product mix for channel-only structures contains a high fraction of aromatic species, and

paraffinic species. These species are absent from the product mix for structures with cavities occluded behind small windows. The cavity structures trap the aromatic species in the methylation / cracking cycle, and over time, cause a carbonaceous buildup within the cavities of the catalyst. When the rate of alkylation exceeds cracking such that polyaromatic species (such as the methylated naphthalenes shown in figure 9-5) are formed, the cavities get blocked with these aromatic species, and that cavity is “deactivated” from the reaction. Channel type frameworks, on the other hand allow these aromatic species to escape from the catalyst. This can be seen from the presence of aromatic species in the product stream, and so typically exhibit a longer catalyst lifetimes. As discussed in some of the more recent works, the product selectivities for the MTO reaction over a material like H-ZSM-5 are independent of coke buildup³⁰. Examples of this reaction behavior are provided below.

Having discussed the types of catalytic materials to be employed in this part of the thesis, the two materials commercialized for this process shall first be explored to understand how well they perform in the desired reaction.

8.8 MTH reaction testing unit

For this part of the thesis, a flow reactor unit (from the one described in the first part of this work) had to be refurbished for use in the reaction. The principle of operation of the reactor unit was essentially identical to the reactor unit described in part I – reactants and carrier gases were independently controlled and then injected into a homogenization vessel, after which, the reactant blend is sent through a reactor tube containing an undiluted catalyst bed.

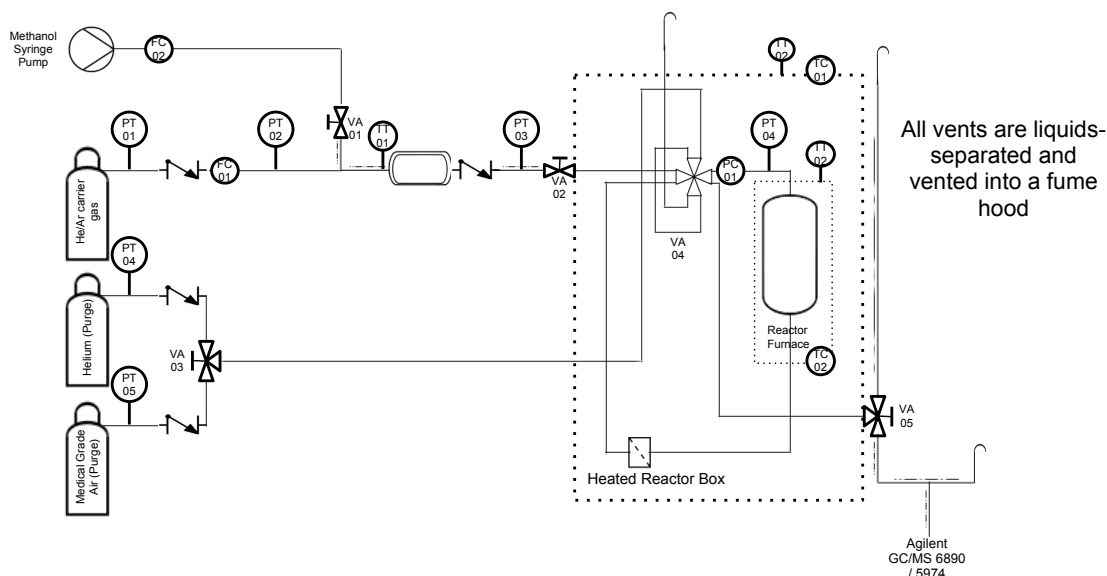


Figure 8-7 MTO reactor piping diagram

Figure 9-7 shows the final piping diagram for the reactor unit. Methanol was injected via a high precision liquid syringe pump. It was then piped to a heated mixing vessel to allow for vaporization of the methanol, and homogenization with the He/Ar carrier gas. The carrier gas used was 5% ultra high purity Ar in ultra high purity He. The Ar is used as an internal standard for self-consistent quantification on the GC/MS. The ion current is used for the quantification. The areas of the reactant and product chromatogram peaks are quantified against the area of the Ar, which shows up as the first (unretained) peak in the chromatogram. Quantifying the reactants and products against this internal standard helps correct for pressure fluctuations as well as changes in the ion current as the filament on the mass spec changes with time. The catalysts loaded into the reactor unit can be pretreated with an inert (He) or with medical grade air (for in-situ calcination). During the pretreatment phase, the purge gases flow over the catalyst bed, and are then sent to the vent. The feed mixture bypasses the reactor bed and is injected into the GC/MS. After operation parameters (feed concentration, bed temperature, vapor flowrate) have stabilized, the 8-way valve (VA04) is switched. After this, the gas streams are switched, so that the purge gases are vented, while the feed mixture is fed through the reactor.

An Agilent GC/MS unit was thus used for the detection of products from the reaction unit. The GC was equipped with an HP Plot-Q column. The temperature programme for the oven was written so that all the hydrocarbons formed from the reaction showed sufficient separation that the peaks could be integrated. This program allowed for the separation of propane and propylene, which proved to be critical in understanding the reaction over 8-membered ring systems.

The results from the reaction run are always compared to the stabilized feed mixture that was bypassing the reactor tube prior to the switching of the 8-way valve. Based on this average input, molar selectivities and conversions were calculated as per Equation 9-1.

$$\text{Conversion, } X = 1 - \frac{n_{CH_3OH \text{ output}}}{n_{CH_3OH \text{ input}}}$$

$$\text{Selectivity to } i, S_i = \frac{n_{\text{carbons in } i} * n_{i, \text{output}}}{n_{CH_3OH, \text{input}} - n_{CH_3OH, \text{output}}}$$

Equation 9-1 Formulae used to compute conversion of methanol and selectivity to products

After having refurbished and set up the reaction-testing unit for operation with this reaction, the next experiments conducted were to run known industrial catalysts to generate a “baseline” to build upon. Methanol-to-hydrocarbons reactions were run over H-ZSM-5 and H-SAPO-34, and compared to numbers presented in the open and patent literature.

8.9 Commercialized Methanol-to-Hydrocarbons (MTH) catalysts

Two materials have been commercialized for the conversion of methanol to hydrocarbons. These happen to be zeolite H-ZSM-5, a aluminosilicate zeolite with a 2-dimensional channel framework, with slightly wider cavities where the channels intersect; and H-SAPO-34, a silicoaluminophosphate molecular sieve with a 3-dimensional channel system with cavities obscured behind 8-membered ring openings. The details of these reactions will be explored in this section.

8.9.1 HZSM-5

H-ZSM-5 is one of the first commercialized^{12,17} and most popular commercial zeolite catalysts. It was commercialized as part of Mobil's Gas-to-Gasoline effort in New Zealand in the 1970s and 1980s³¹. H-ZSM-5 is an acidic aluminosilicate zeolite catalyst with the MFI (Mobil number five) framework. A 3D caricature of this framework along with a schematic representation of the channel system is shown in Figure 9-8.

The framework is made up of a channel structure of intersecting 10-membered ring channels. There are straight channels in the 010 direction (vertical direction in the left panel), and perpendicular to that, in the 100 direction, is a sinusoidal 10-membered ring channel (horizontal direction). A view down the straight channel is shown in the image on the right. There is a wide range of acid site densities that can be made with this material, either with or without an organic structure-directing agent³².

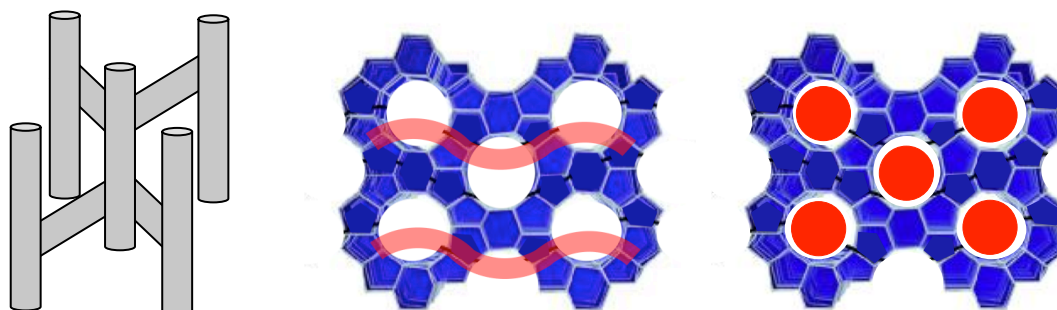


Figure 8-8 Channel System schematic, each grey area is a channel for molecular transport (left). The framework of H-ZSM-5, MFI, with red forms indicating the two types of channels: sinusoidal (center), straight channel (right).

The typical synthesis for an MFI material involves the use of a tetrapropylammonium template. This synthesis was attempted as a starting point for this study as well. Starting with this comparison and reproduction of the catalytic test of an existing commercial catalyst, the remainder of this present work will be presented in segments detailing the synthetic protocol, followed by the reaction testing data.

The synthesis gel composition was 0.29 NaOH : 0.074 (CH₃CH₂CH₂)N⁺Br⁻ : 0.024 Al₂O₃ : 1 SiO₂ : 36.25 H₂O. Cab-o-sil M5 was used as the silica source, sodium aluminate was used as the aluminium source. Sodium Hydroxide pellets were used as a further source of sodium. Tetrapropylammonium Bromide crystals were used as the source for the organic structure-directing agent. The gel yielded solid crystals after 4 days at 150°C without agitation. The powder XRD pattern was consistent with what was reported in literature for MFI. An EDS analysis yielded a crystal composition of Si/Al = 28.3 ± 0.53. The solid crystals were calcined in air with the temperature ramp shown in Figure 9-9 in a flow of medical grade air (<1000 PPMV CO₂, <10 PPMV CO, <5mg/m³ aerosols). The calcined solids were then exchanged to remove sodium cations from the solid. A 1 mol/L solution of NH₄NO₃ in de-ionized water was used as the exchange media. 50 ml of exchange media was used per gram of calcined solid. This process replaces the combination of protons and alkali metal ions that are charge balancing ionic sites in the zeolite with ammonium ions. Exchanges were carried out in 50 ml centrifuge tubes for 2 hours at 95°C. After the exchange, the media was decanted off, and the solids were washed thrice with 50 ml of deionized water, and dried. In order to “activate” the acid sites on the zeolite the solids were calcined in situ under a flow of ultra high purity argon at 580°C. This activation process causes the ammonium ions to decompose yielding ammonia gas and protons to balance the charge balance sites in the zeolite.

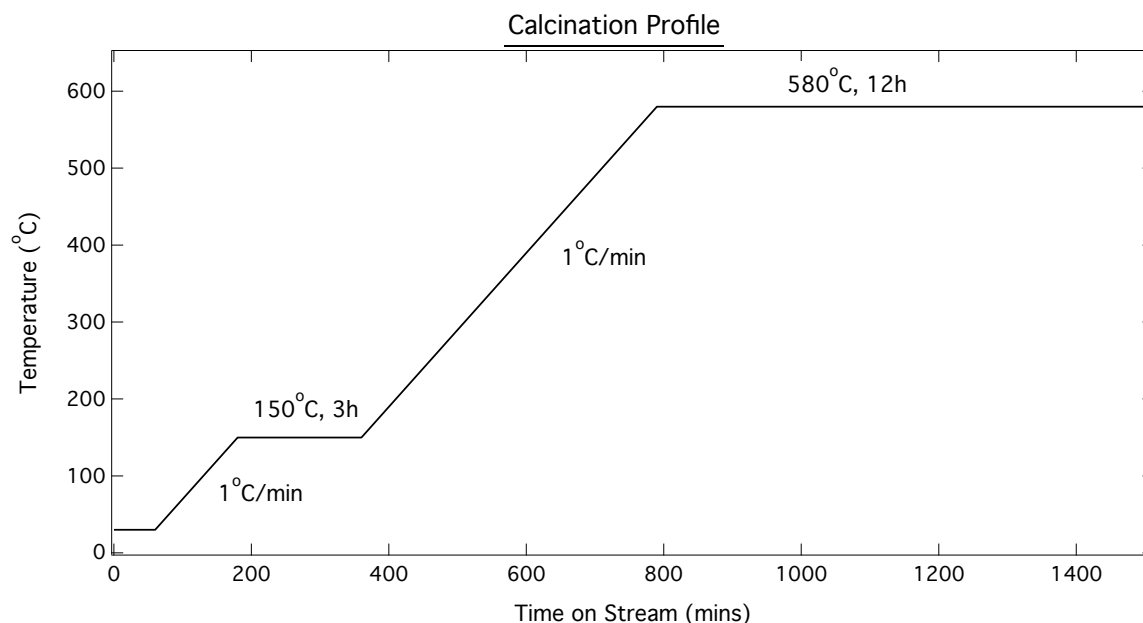


Figure 8-9 Calcination temperature profile

Methanol in a flow of helium/argon (95/5) at a concentration of 60% methanol was then fed to the catalyst that was being held at 400°C. The resulting product profile is shown below in Figure 9-10. The stability of the conversions and selectivities as a function of time was the most remarkable thing about this catalyst. Over the 10 hour reaction run, the conversion was always at 100%, and all the product selectivities did not vary by more than 2%. The selectivities of ethane and ethylene were almost identical to one another throughout the entire length of the reaction run. In addition to the products shown here, there was also a substantial amount of benzene, toluene and xylenes being produced (combined selectivity 24%-28%).

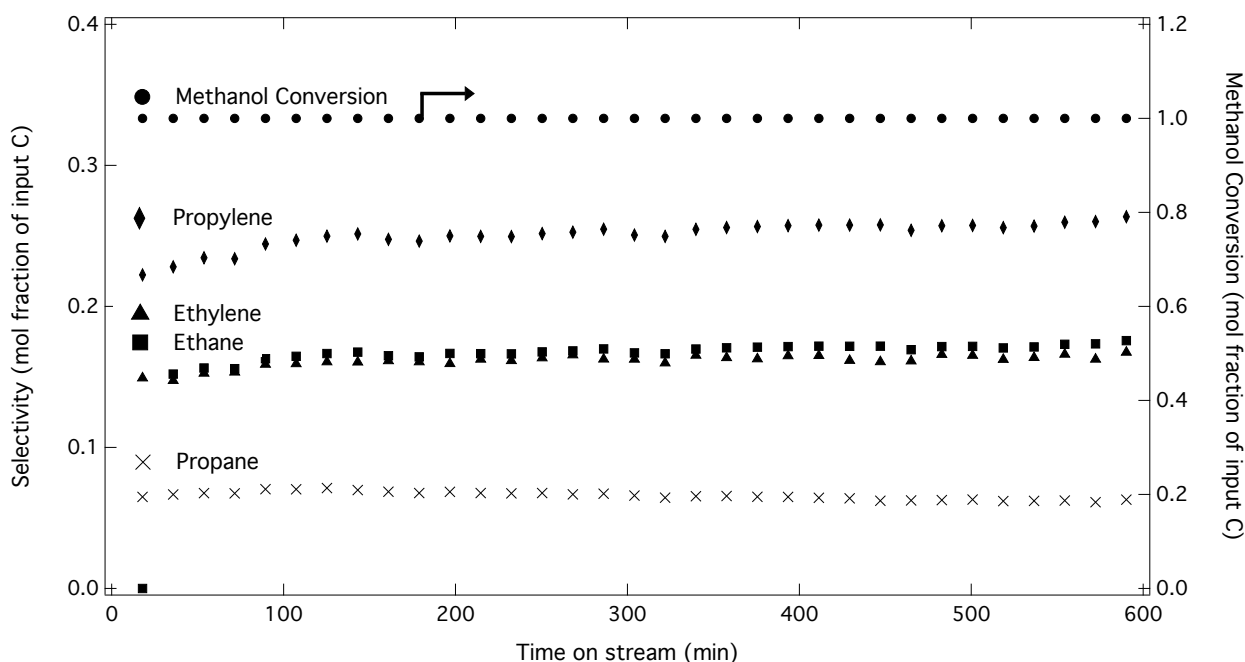


Figure 8-10 Reaction profile of H-ZSM-5

This is very similar to the data presented by Chang and Silvestri¹². The reactions in their initial study were run at 371°C, at a WHSV of 1h⁻¹, in a neat methanol feed. Chang et al. also published a series of two papers on the effect of reaction parameter variations on the product selectivities of the MTO reaction over H-ZSM-5^{29,33}. The first of these papers looked at the effect of reaction temperature, zeolite Si/Al ratio and methanol pressure on the selectivities in the reaction. They showed that over ZSM-5, the aromatics formation was not strongly affected by temperature. Increasing the reaction temperature resulted in higher selectivity towards C₂-C₅ olefins. Further, they showed that when they diluted the methanol feed with water, the selectivity towards light olefins increased. At each Si/Al ratio, Chang also looked at the effect of varying the liquid hourly space velocity. For all the Si/Al ratios they studied, the C₂-C₅ selectivity formed a parabola when plotted against liquid hourly space velocity (LHSV). The maximum selectivity they obtained was with a catalyst that had a Si/Al of 500, and the reaction run had a LHSV of 0.1 h⁻¹. Since they had used 3 cm³ of catalyst per reaction run, this translated to a liquid hourly space velocity of 5μl/min. For 200mg of dry catalyst being loaded per reaction run, this translates to a weight hourly space velocity of 1.19 h⁻¹. These data, and

this catalyst, was used as a starting point to determine the general testing conditions to be used as part of this project, with the objective being maximizing selectivity towards light olefins, and in particular, propylene.

Since the goal of this project is to increase selectivity towards a particular light olefin, higher temperatures and lower concentrations were considered while looking at channel-type structures. A brief study of varying temperatures showed that temperatures above 450°C yielded rapid deactivation of the catalyst bed, and a relatively poor selectivity to light olefins. Thus, 400°C was chosen as the standard test reaction temperature. These were the first conditions used for all subsequent tests of various zeotype materials. Initially starting with a 60% MeOH in inert feed, the feed concentration was lowered in an attempt to get higher selectivities to light olefins. Finally, a feed concentration of 10% MeOH in inert was decided as the feed concentration. All the reactions used 95%He/5%Ar as the inert. While this is a narrower range than what was studied by Chang et al., it also showed that the with a methanol weight hourly space velocity of 1.3h^{-1} gave the optimal selectivity towards light olefins.

There some caveats associated with this brief parametric analysis that has been conducted that should be noted. First, all the trends described were based on data collected on H-ZSM-5, and varying the framework can have an impact on how the reaction responds to parameter variations, particularly response to temperature variations. Second, the conditions were tuned for the highest light olefin selectivities while keeping aromatic make low. A large portion of the work presented in this thesis involved the synthesis and reaction testing of zeolites with 8-MR frameworks, such as CHA. In these structures, there is no aromatic make in the product stream. Thus, reaction temperatures would have to be varied in order to obtain conditions that would give the highest selectivity towards propylene over other light olefins. Finally, other catalyst parameters would also affect these selectivities, the first of which (acid site concentration) is studied below.

8.9.1.1 *Study of Si/Al effects on selectivities of MTH reaction on MFI*

The reaction of one Si/Al material at one temperature was reported above. The next step to try to understand the effect of catalyst structures and structure parameters on the conversions and selectivities was to try to vary the Si/Al of MFI to understand the effect on the first catalyst tested.

In order to get several MFI materials with varying Si/Al, some commercial samples (Zeolyst, Inc academic sample) were obtained and an aluminium rich sample was synthesized via the organic free route³¹. Upon characterizing their aluminum contents, the materials had Si/Al ratios of 28.3 and 140 for the two commercial materials, and 13.7 for the aluminium rich material synthesized by the organic-free route. Upon testing all the materials at 400°C under a flow of 10% methanol in 95% helium/5% argon at a weight hourly space velocity of 1.3h⁻¹, the following summarized chart was made (see Figure 9-11).

As anticipated, the lower the Si/Al content of the zeolite material, the lower the net selectivity towards light olefins. Based on the mechanism depicted in Figure 9-5, it can be expected that the higher the concentration of the strong acid sites, the more secondary conversions to benzene, toluene and xylenes can be expected. Further, since MFI is a channel type framework, these products should be removed from the catalyst as products of the reaction. This is indeed what was observed in this set of experiments. As the Si/Al ratio is reduced, more BTX is observed at the expense of selectivity to light olefins. This is consistent with what is observed in the literature for the reaction of both methanol²⁹ and ethanol³⁴ over MFI of various Si/Al ratios. Studies by Chang et al. also showed that the higher the Si/Al, the higher the selectivity towards light olefins.

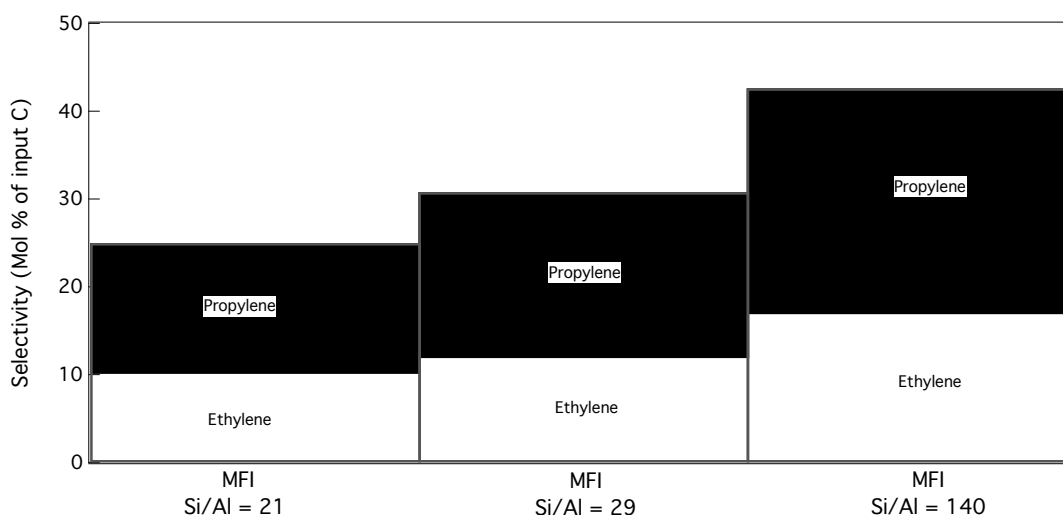


Figure 8-11 Effect of Si/Al on selectivities to light olefins

All of these runs were conducted under the same weight hourly space velocity and methanol concentration. It could be possible to gain mechanistic insight on the reaction by studying the reaction under constant methanol flow per acid site. Normalizing the above cumulative $C_2 + C_3$ selectivity by the Si/Al ratio to gain qualitative insight into whether there are mechanistic differences at different Si/Al ratio yields essentially the same number for the first two samples (1.1-1.2), but a much lower number (0.33) for the high Si/Al ratio sample. This would suggest that the data as presented in figure 9-11 need to be treated more carefully. That is, the difference between the first two bars is simply a normalization problem, while the last bar actually does show that there is a difference mechanistically (perhaps fewer secondary conversions) at higher Si/Al ratios.

Once again, there are several caveats that need to be kept in mind while studying these data. First, these Si/Al ratios are taken at face value. No analysis was ^{27}Al -MAS NMR analysis was conducted to look for extraframework Alumina species that would not contribute to the acid site density but would contribute to the Si/Al ratio. The template free material probably has the most extraframework alumina. Second, other catalyst parameters, such as crystallite sizes were not controlled for in this study. These changes could also have a notable impact on the selectivities being perceived. Finally, as shown by Chang et al²⁹, the hourly space velocity

that yields maximum olefin selectivity increases with increasing Si/Al. The hourly space velocities were not optimized here for each Si/Al studied. The reaction data presented in this work focuses on selectivities obtained under operating conditions of 100% conversion of methanol. Thus, an analysis of the selectivities obtained under this condition will not be presented.

Since the catalytic activity of the MFI framework in the MTO reaction has now been looked at, and the effect of acid site concentration in the same catalyst has also been studied, a baseline has been set for the MTH reaction. The next catalyst that was studied was a small pore molecular sieve, HSAPO-34. It is expected that there will not be aromatic compounds in the product stream from the MTO reaction over the small pore catalyst since these are too large to fit through the pore openings. The HSAPO-34 catalyst has been commercially implemented in the Dalian Institute of Chemical Physics' (DICP) dimethyl ether to olefins (DMTO) plant¹¹.

8.9.2 HSAPO-34

As mentioned previously, this was the first 8-membered ring (MR) opening containing material tested as part of this work. This is a silicoaluminophosphate molecular sieve with the CHA framework. It has 8-MR windows opening into a larger cavity. The cage present in the structure is shown below in Figure 9-12. The structure is made up by connecting these cages via double 6-MR. The 8-MR windows open up into a much larger, 12-MR cavity. Unlike zeolites, the acid sites in SAPO materials is created by the incorporation of tetravalent Si atoms in an otherwise tri- and penta-valent framework. Thus, rather than characterizing the solid by the Si/Al ratio, two different elemental composition metrics are necessary to characterize the catalyst. First, in order to ensure that there is no Si islanding present in the solid material, the $\frac{Si+P}{Al}$ ratio should not exceed 1. In a SAPO molecular sieve, the silicon atoms substitute the phosphorous atoms. In order for these silicon atoms to form quantifiable acid sites, the silicon atoms must be isolated. However, since silicon is a tetravalent atom, and it can form an

extended tetrahedral structure, as seen in zeolites. It can thus form an extended tetrahedral silicate structure within the AIPO framework, or an “island”. These islands are not site-isolated silicon, and thus only the atoms on the edge of the island can generate acid sites. Second, as a characterization of the density of acid sites present in the molecular sieve, the $\frac{(Al+P)}{Si}$ ratio is an analogous quantity to Si/Al, quantifying the inverse of the density of the acid sites in the solid material. However, as mentioned previously, if islanding is present, the ratio $\frac{(Al+P)}{Si}$ would overcount the number of acid sites present.

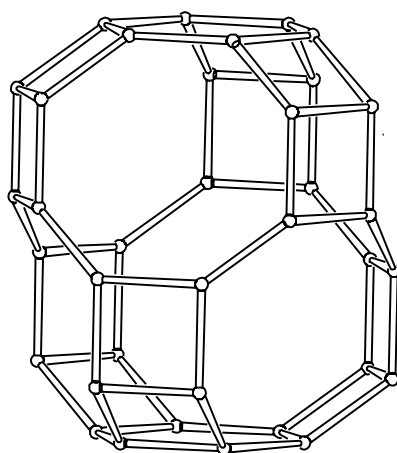


Figure 8-12 CHA cage in CHA framework¹⁴

The synthesis of this material was carried using a recipe found in the literature³⁵. The synthesis gel had a composition of 0.5 $((CH_3CH_2)_4N)_2O$: 1.6 $(CH_3CH_2CH_2)_2NH$: 1 Al_2O_3 : 1 P_2O_5 : 0.3 SiO_2 : 50 H_2O . Ludox LS-40 was used as the silica source, Catapal B- Alumina as the Aluminum source, 85% Orthophosphoric Acid as the phosphorous source, and organics were obtained from Aldrich and used as is. The material characterization yielded a material that had a $\frac{Si+P}{Al}$ ratio of 0.9, and a $\frac{Al+P}{Si}$ ratio of 11.8. The first quantity is slightly below 1 due to the presence of microcrystalline Alumina present in the solid. The crystal domains of these alumina crystallites are smaller than the detection limits of the powder XRD instrument being used, thus the lines associated with any of the common phases of alumina were not observed in the powder XRD pattern.

The data obtained from the continuous cycling of a SAPO-34 catalyst in the plant set up by the Dalian Institute of Chemical Physics (DICP) yielded the graph shown below in Figure 9-13. Rather than the fixed bed continuous flow reactor that is being used for reactions in the laboratory that are presented in this work, the industrial system from which the data in figure 9-13 were obtained works on a continuous fluidized bed reactor – regenerator loop. The catalyst is fluidized in a gas stream containing the reactants. At the end of the reactor, a cyclone separates the solid catalyst from the reactants and products. The catalyst is then regenerated in heated air before being recycled back into the fluidized bed reactor. The selectivity towards all the products are very stable throughout the time of study. Since this is a continuous cycling process, this is the data off of an “average age” catalyst. The overall selectivity to light olefins is close to 80 wt% throughout the 11 day trial. Further, the selectivity to the individual components of ethylene and propylene are 40 wt%. This is the disadvantage of the catalyst, that the selectivities towards the light olefins are almost identical, requiring extensive separation in order to yield the two desired monomers.

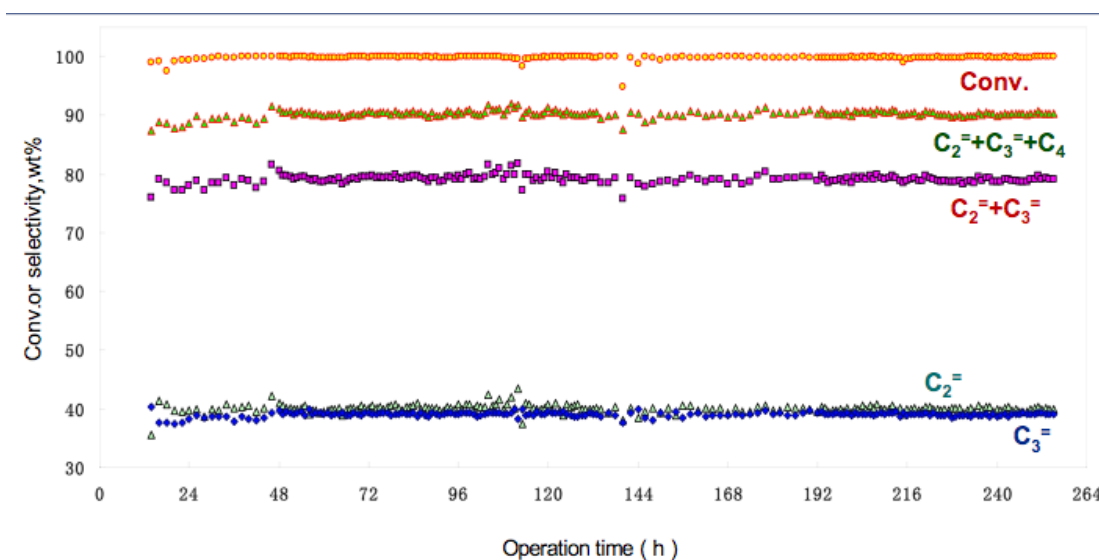


Figure 8-13 Fluidized bed circulation data for HSAPO-34³⁶

An analogous run on the packed-bed reactor was also run at 400°C, under standard flowrate conditions. The conversion and selectivity data obtained from a single run are shown

in Figure 9-14. The time profile is very different from the circulating reactor and the HZSM-5 catalyst that was shown previously. First, there is a marked buildup period, in which the selectivity towards ethylene and propylene increase from about 20 mol% to roughly 35 mol%. Upon completion of this buildup period, there is a six hour period during which the selectivities towards all the light hydrocarbons shown is stable. At the end of this period, the catalyst deactivates rapidly, during which selectivities towards ethylene and propylene drop to 0. While conversion of methanol remains high during this period, the methanol is merely dehydrated to dimethylether during this phase. Upon converting the mol% numbers to mass % numbers, the results during the 6-hour stable period correspond well with the data presented by DICP. While the focus of this reaction study is selectivity towards ethylene and propylene, it is important to note that there were C_4 compounds produced during the reaction, the DICP study showed roughly a 10 weight % selectivity towards C_4 compounds, which was similar to the C_4 content observed in the fixed bed reactor.

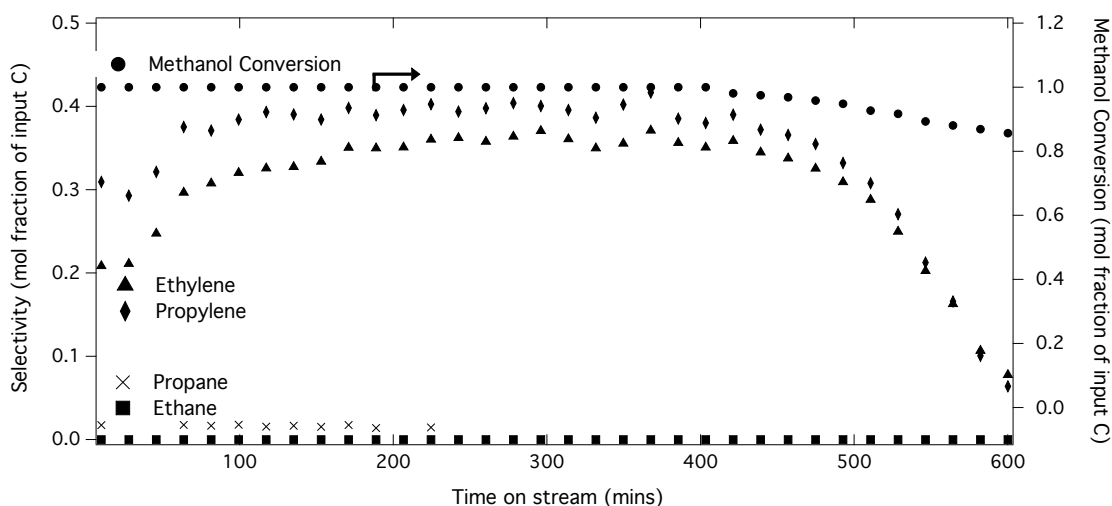


Figure 8-14 Selectivity and conversion over HSAPO-34 in packed bed reactor

8.10 Objectives for project & layout of this section

Through these studies on HZSM-5 and HSAPO-34, a baseline of selectivities and conversions was obtained for channel, and cage type materials, respectively. The objective of

this project, thus, is to try to understand the effect of zeolite structures on the selectivities in the methanol-to-olefins reaction, with the specific goal to try to find a way to improve the selectivity towards propylene.

In an attempt to do this, a step-by-step study of different parameters of the catalyst structure that may affect the selectivity in the MTO reaction are studied. The focus was on structures with 8-MR openings leading into larger cavities. The first study carried out involved understanding how the width of the cavities affected the selectivities towards various products. Then, at the optimal cavity width, the length of the cavities was varied to try to understand how this affected the selectivity towards various products. Finally, the composition of the framework was also varied.

The hypothesis behind all of these framework parameter variations is that the shapes and sizes of the cavities present behind the small openings in MTO molecular sieves affects the hydrocarbon pool in terms of their relative alkylation and cracking rates. Studies by the Bhan group have begun to place kinetic parameters upon these relative alkylation and cracking rates on channels of varying widths and sizes²⁵. Given the large reaction network that the MTO reaction undergoes, certain kinetic parameters can be optimized in order to yield a higher selectivity towards propylene.

As stated previously, there are two alkylation-cracking cycles occurring as part of the overall MTO reaction to yield the light olefins desired. The first is the direct alkylation-cracking of the olefinic species being formed, and the second is the alkylation cracking sequence associated with the branches of the aromatic “hydrocarbon pool”. Therefore, the relative rates of the alkylation – cracking sequence would determine the selectivity to the light products desired. Intuitively, the higher the alkylation rate is to the cracking rate, the longer the hydrocarbon chains produced during the reaction. Since molecules with more than 4 carbons cannot exit through an 8-MR opening, the higher this ratio is, likely the higher the C₃-C₄

products. Further, since this is a cascade reaction that is catalyzed by the zeolite in question, if structure effects are to have an effect on the product distribution, it would have to be through stabilization of any intermediates that are critical to the desired product.

Prof. Bhan's group at the University of Minnesota conducted studies over channel-type zeolites to understand the kinetics of the hydrocarbon reactions involved in the MTH reaction. The first set of studies of interest compared rates of methylation of C₂ and C₄ compounds over various zeolites.^{25,37} They found that the activation energy for methylation was structure independent in the case of 1-butene, and also very similar in the case of propylene. In the case of ethylene methylation, the structures with 12-MR openings show a lower activation energy than the 10-MR structures. Thus it appears that a larger opening size is required for the stabilization effects of the zeolite structure to be perceived by the kinetics of the reaction. Thus, for the alkene methylation route to propylene, it appears that 12-MR channels would be preferred over 10-MR channels since the 10MR channels would just as easily promote alkylation past propylene, but require more energy to alkylate the ethylene. However, as mentioned previously, there are two routes to generate propylene in the cascade reaction above, one is through direct methylation, the other is through methylation and cracking of the side chains of aromatic species. Based on some of the work by the same group³⁸, lower temperatures tend to favor the aromatic cycle, while higher temperatures favor the aliphatic cycle. In order for propylene to be the product of this cycle, an intermediate with a propyl branch must be formed, and stabilized. Work by Wichterlová et al. showed³⁸ that for isopropanol alkylation of benzene and toluene, more open structures favor the formation of more branched products, analogous to the isopropyl benzene related substituent that is required for formation of propylene through a cracking reaction. Thus, given the two slightly differing pictures on the effect of structure on the selectivity towards precursors that would yield propylene as a product, further study on the effect of framework topology on olefin selectivity are warranted. While

this work will not provide a detailed and thorough kinetic analysis of the effect of structures on individual reactions in the cascade, it will try to provide a macroscopic view of how framework variations affect olefin selectivity given reaction conditions that are close to operating conditions. (high conversion of methanol)

Aside from the framework structure parameters mentioned above, the reaction parameters (such as temperature, pressure, space velocity, reactant concentration) would also affect the product selectivities in the reaction. For each of the structures, the effect of temperature variation was looked at to understand the effect of reaction temperature on the selectivity for different frameworks. Based on work presented by Wu et al.³⁹, for HSAPO-34, increasing reaction temperature resulted in an increase in the $C_{2=}/C_{3=}$ ratio. Thus, emphasis will be put on the lower operating temperatures (350°C – 400°C). However, the effect of other operating parameters such as the space velocity, concentration and pressure were not studied extensively. Based on previous work by Liang et al., varying the space velocity by a factor of four resulted in no marked change in the hydrocarbon selectivity.

8.11 Bibliography

- (1) Kniel, L.; Winter, O. *Ethylene, keystone to the petrochemical industry*; 1980.
- (2) Moliner, M.; Roman-Leshkov, Y.; Davis, M. E. *Proceedings of the National Academy of Sciences* **2010**, *107*, 6164–6168.
- (3) Serrano-Ruiz, J C; West, R.; Dumesic, J. *Annual Review of Chemical and Biomolecular Engineering* **2010**, *1*, 79-100.
- (4) Wettstein, S G, et al. *Current Opinion in Chemical Engineering* **2012**, *1*, 1-7
- (5) Abu El-Rub, Z.; Bramer, E. A.; Brem, G. *Industrial & Engineering Chemistry Research* **2004**, *43*, 6911–6919.
- (6) Corella, J.; Toledo, J. M.; Molina, G. *Industrial & Engineering Chemistry Research*

- 2006**, *45*, 6137–6146.
- (7) Kopyscinski, J.; Schildhauer, T. J.; Biollaz, S. *Fuel* **2010**, *89*, 1763–1783.
 - (8) Ding, Y.; Alpay, E. *Chemical Engineering Science* **2000**, *55*, 3929–3940.
 - (9) Iglesia, E. *Applied Catalysis A, General* **1997**, *161*, 59–78.
 - (10) Chinchén, G. C.; et al. *Applied Catalysis* **1987**, *30*, 333–338.
 - (11) Olsbye, U.; et al. *Angew. Chem. Int. Ed.* **2012**, *51*, 5810–5831.
 - (12) Chang, C.; Silvestri, A. *Journal of Catalysis* **1977**, *47*, 249–259.
 - (13) Liang, J.; Li, H.; Zhao, S.; Guo, W.; Wang, R. *Applied Catalysis* **1990**.
 - (14) Baerlocher, C.; McCusker, L. B.; Olson, D. H. *Atlas of Zeolite Framework Types*.
 - (15) Curkovic, L.; Cerjan-Stefanovic, S.; Filipan, T. *Water research* **1997**, *31*, 1379–1382.
 - (16) Joshi, S.; Fair, J. R. *Industrial & Engineering Chemistry Research* **1988**, *27*, 2078–2085.
 - (17) Cejka, J.; Zones, S.; Corma, A., *Zeolites and Catalysis*, Wiley-VCH: Weinheim, **2010**, Vol 2.
 - (18) Davis, M. E.; Lobo, R. F. *Chemistry of Materials* **1992**, *4*, 756–768.
 - (19) Casci, J. L.; Lowe, B. M. *Zeolites* **1983**, *3*, 186–187.
 - (20) Loewenstein, W. *American Mineralogist* **1954**, *39*, 92–96.
 - (21) Flanigen, E. M.; Patton, R. L.; Wilson, S. T. *Studies in surface science and catalysis* **1988**, *37*, 13–27.
 - (22) Svelle, S.; Bjørgen, M. *J. Phys. Chem. A* **2010**, *114*, 12548–12554.
 - (23) Svelle, S.; et al. *J Am Chem Soc* **2006**, *128*, 14770–14771.
 - (24) Song, W.; et al. *J Am Chem Soc* **2000**, *122*, 10726–10727.
 - (25) Hill, I. M.; Hashimi, S. A.; Bhan, A. *Journal of Catalysis* **2012**, *285*, 115–123.
 - (26) Chang, C D; *Catal Reviews* **1983**, *25*:1, 1-118
 - (27) Chen, Y et al. *Catal Lett* **2008**, *124*, 297-303

- (28) Keil, F J; *Micropor Mesopor Mater* **1999**, 29, 49-66
- (29) Chang, C D; Chu, C T; Socha, R F *Journal of Catalysis* **1984**, 86, 289-296
- (30) Bleken, F L, et al., *Micropor Mesopor Mater* **2012**, 164, 190-198
- (31) Chang, C. D. *Catalysis Today* **1992**, 13, 103–111.
- (32) Machado, F. J.; López, C. M.; Centeno, M. A.; Urbina, C. *Applied Catalysis A, General* **1999**, 181, 29–38.
- (33) Chang, C D; Lang, W H; Smith R H *Journal of Catalysis* **1979**, 56, 169-173
- (34) Inoue, K.; et al. *Catalysis Letters* **2010**, 136, 14–19.
- (35) Park, J.; et al. *Applied Catalysis A, General* **2008**, 339, 36–44.

- (36) Liu, Z; Presentation, May 23-24, 2007,
http://belfercenter.hks.harvard.edu/publication/10136/coal_to_chemicals.html
- (37) Hill, I M; Ng Y S; Bhan A *ACS Catalysis*, **2012**, 2,1742-1748

- (38) Wichterlová, B; Čejka, J; Žilková, N; *Microporous Materials* **1996**, 6, 405-414
- (39) Wu, X; Abraha, M G; Anthony R G; *Applied Catalysis A* **2004**, 260, 63-69

Chapter 9 Effect of channel size and shape on MTO reaction

The previous chapter provided background information on methanol to hydrocarbons chemistry, particularly the major catalysts that have been studied and some of the mechanistic details that are already known. In this chapter, the first study of structural feature effects on MTO selectivity conducted as part of this work will be presented. That is, the effect of changing the channel cross-section on the MTO reaction.

Light olefins can be formed from methanol over microporous acidic catalysts through two connected reaction pathways¹. One of the routes through which light olefins are formed in the MTO cascade is through an alkylation-cracking sequence^{1,2} of the side chains of aromatic species. As the intermediate through this pathway is an alkylated benzene species, it is important to understand whether local confinement effects would affect the stability of these intermediates, and if this would result in differing selectivities to light olefins. Literature precedent suggests³ that local confinement can affect the thermodynamics of reaction intermediates and transition states in the case of a couple of model reactions, and this can in turn have an effect on the conversions and selectivity of reactions. The work of Lesthaeghe et al.⁴ also emphasizes the importance of transition state and intermediate stabilization of the carbocationic intermediate on the reactivity of these organic species in the MTO reaction. Thus, in order to increase selectivity towards a desired product, the desired reaction intermediate needs to be stabilized relative to its reactants more so than its products, and this change needs to affect the desired intermediate more so than intermediates that lead to other products.

One possible model intermediate for the reaction is toluene. This molecule can subsequently undergo an alkylation-cracking sequence to yield desired light olefins as products. Post reaction data has shown this to be one of the occluded organic species in the solid (see chapter 11). Based on trigonometry and reported bond lengths for toluene⁵, the planar dimensions of this molecule are roughly 4.7Å by 2.4Å. Thus, an 8-MR channel would not be

able to accommodate the aromatic intermediates. However, channels larger than 8-MR can accommodate these substituted aromatic species within them, with a 10-MR channel being the next tightest fit. One hypothesis is that a larger channel would have a “flatter” local surface, allowing the intermediate to be more closely associated with the catalyst surface (see figure 10-1). In order to understand whether this solvation would play a strong role in affecting the stability of the cationic intermediate formed in the reaction, a study of the effect of channel sizes on the selectivities to various light olefin products in the reaction was conducted.

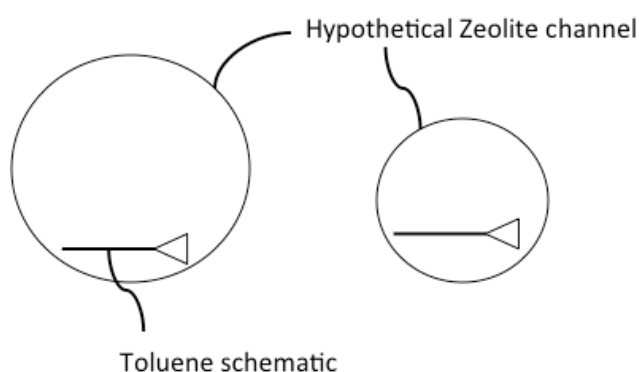


Figure 9-1 Caricature of toluene intermediate in channels of different sizes

The “fit” described in the work from the Iglesia group could also be affected by the eccentricity of the channels in question. Given the intermediates are mostly planar (aromatic rings) with small deviations at the alkyl substituents, the proximity of the cationic intermediate with the reactive center as well as the strength of the solvation effect could be also determined by how closely the channel shape fits the intermediate shape (see Figure 10-2). The hypothesis for this change would be that the more elliptical the channels are, the closer the intermediate can be to the channel walls.

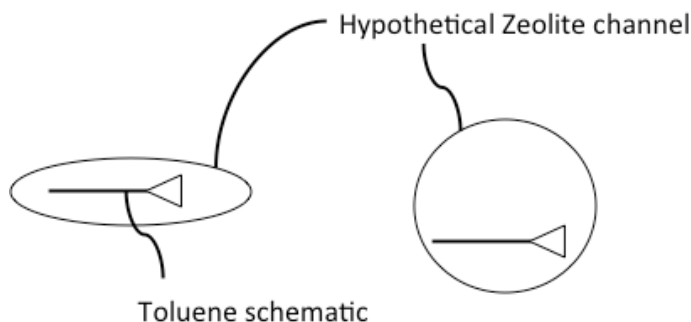


Figure 9-2 Caricature of toluene intermediate in channels of different eccentricities

Both of these effects would alter the stability of the intermediates and the transition states that are formed in this reaction cascade. The selectivity towards ethylene and propylene were used as indicators for whether the confinement effects altered stabilization of the intermediates in the desired direction. In order to control the reaction parameters, the structures were compared at the same weight hourly space velocity (1.3h^{-1}), the same concentration of methanol in helium (95%) / argon (5%), (10%) and the same reaction temperature, 400°C .

As with other studies conducted thus far, there are a few caveats to the approach to study the effect of the channel cross section. First, as seen below in the next few sections, in order to promote selectivity towards propylene in a single pass, the selectivity towards light olefins needs to be maximized. In order to do this, structures with cavities occluded behind small pore openings (like chabazite) would be preferred over channel type structures. Using channel structure data as a proxy for structures with cavities differing sizes behind small pores has several limitations. Most importantly, it does not reflect the effect of severe diffusion limitations (aromatic structures cannot escape) that the organic co-catalyst encounters in the small pore materials. These restrictions undoubtedly have an effect on the reaction pathway that is not reflected in the channel systems study. The channel materials would also not provide a good proxy because they would not provide confinement in 3 dimensions analogous to what is present in the cavity type structures. However, since the aromatic species form through a ship-in-a-bottle type process in a cavity structure, and cannot be directed to form particular aromatic

species, it is difficult to ascertain the effects of these changes in isolation. Thus, this study was conducted over channel type structures even though these would not be the ideal structures to direct formation of light olefins.

Keeping the operating parameters constant across the various structures also comes with some caveats. First, as seen from studies by Chang et al.⁶ and Wu et al.⁷ temperature changes affect different catalysts differently. Thus, studying a constant reaction temperature across all the structures would not yield the absolute maximum selectivity towards a particular light olefin that that structure can yield, but rather, a the selectivity at just one particular temperature. Second, as shown by work from Illias & Bhan⁸ on MTO catalysis over HZSM-5, the side chain cracking mechanism is dominant at lower reaction temperatures. Third, as seen from studies by Chang et al.⁹, variations of the space velocity of methanol over HZSM-5 result in a maximum selectivity towards light olefins for each Si/Al ratio. The maxima do not coincide for the various Si/Al ratios. Again, this would yield the same problem that was seen with keeping the temperature constant. The selectivity observed would be the value for that material under an arbitrary set of conditions, rather than the maximum possible from that structure. However, keeping these parameters constant allows for the assessment of the impact the structural changes have on the reaction pathway under constant energy, and concentration conditions.

9.1 Methods & Materials

In order to study the effect of channel size and shape on the selectivity towards light olefins, 1-dimensional channel structures of varying dimensions were used as proxies for various cavity sizes and shapes. Ideally, the materials would be synthesized such that only the channels varied across the materials studied. Most of the materials presented here had been previously synthesized in the lab, and possible synthesis protocols used are referenced. The

materials used in these studies are presented in table 10-1. Under ideal circumstances, the channel sizes would span a range of channel widths from 8MR materials to 14 MR materials. However, obtaining 1-D channels with 8MR and 14MR openings and a catalytically interesting acid site concentrations proved difficult. Thus, the materials presented here show a comparison of 10 and 12MR zeolites and the effect of channel width, and the effect of channel eccentricity on the product selectivity in the MTO reaction. The materials selected for this study show a variation in channel size from 4.4Å to 7.2Å, and eccentricities that range from 0 for the perfectly circular channels (ZSM-48) to 0.6. Eccentricity was computed using the formula

$$e = \sqrt{1 - \frac{b^2}{a^2}}, \text{ where } b < a.$$

In order to run all of these materials under constant reaction conditions, all the materials were tested at 400°C, at 1.3h⁻¹ weight hourly space velocity of methanol at a concentration of 10% methanol in the inert gas stream. Typical catalyst loadings were 200mg of undiluted zeolite catalyst. All catalysts were activated to their proton forms by calcination to 580°C, ammonium exchange, followed by activation in inert, in-situ at 580°C prior to reaction testing.

Material (Framework)	Size of 1D Channel
ZSM-23 (MTT) ¹⁰	10MR (4.4Å x 5.2Å)
ZSM-22 (TON) ¹¹	10MR (4.6Å x 5.7Å)
ZSM-48 (*MRE) ¹²	10MR (5.5Å x 5.5Å)
SSZ-41 (VET) ¹³	12MR (5.9Å x 5.9Å)
ZSM-12 (MTW) ¹⁴	12MR (5.6Å x 6Å)
SSZ-42 (IFR) ¹⁵	12MR (6.2Å x 7.2Å)

Table 9-1: Materials selected to study effect of channel size on the MTO reaction

9.2 Effects of channel size & channel eccentricity

Table 10-2 shows a summary of the Si/Al ratios and the product selectivities observed over the series of catalysts chosen. SSZ-41 was not included in this list as only dehydration products were observed over this material, between 350°C and 450°C. This suggests that the acid sites in the sample of SSZ-41 used in the study had lost its Brønsted acidity, which may have been due to the workup procedure employed. As mentioned above, while ideally all the structures studied should have similar Si/Al ratios, the materials available for testing had a range of Si/Al ratios from 24 to 80. Apart from ZSM-12 and ZSM-23, the materials had remarkably poor catalyst lifetimes (< 1h). Lifetime was defined as time taken for conversion to fall below 80% of the input methanol. Based on preliminary data from other structures studied, once the conversion dropped below this point, the selectivity towards the desired light olefin products declined rapidly, and predominantly DME products were seen. ZSM-12 and ZSM-23 had very stable conversion and selectivities that only decreased gradually over the time course of the reactor run. All the materials except ZSM-48 (68%) and SSZ-42 (80%) had 100% conversion of methanol.

Most of the materials yielded very low selectivities towards the light olefins, but showed a very favourable $C_3=C_2=$ ratio (much higher than 1). The SSZ-41 material yielded dimethyl ether as the only product from the reaction, and was deemed to be inactive due to the Brønsted acid sites being leached out during the pretreatment procedure. The original SSZ-41 patent presents data from reactions that require Brønsted acid sites. Thus, this could have been specific to the harsh procedure used for the post-synthetic workup used as part of this work. As seen from Table 10-2, there is no consistent trend in terms of channel size with the maximum selectivities observed for propylene and ethylene.

In order to get a better understanding of these data, the reaction data were plotted against certain key dimensions to try to understand if there is any trend, or any critical value that is necessary to enhance the reaction.

Material	Si/Al (by EDS, $\pm 2\%$)	Reaction Temperature (°C)	Lifetime (Conv < 80%)	Maximum C ₂₌ selectivity	Maximum C ₃₌ selectivity
ZSM-23	35	400	>4h	5	25
ZSM-22	51	400	35 mins	7	23
ZSM-48	80	400	1h	0	9
SSZ-41	50	400	(Dehydration Only)		
ZSM-12	39	400	>4h	4	26
SSZ-42	24	400	40 mins	5	7

Table 9-2 MTO Reaction data over select 1-D aluminosilicate zeolites at 400°C

As seen from this figure, only one distinct trend can be drawn. The other points on the plot of maximum selectivities against the channel dimensions yield no pattern. Apart from one outlier (ZSM-12), the remaining data for maximum propylene selectivity plotted against the smaller of the cage dimensions yields a good linear fit. These data are shown by the red squares in figure 10-3. It suggests that the smaller the semi-minor axis is, the higher the selectivity to propylene. It may suggest that in order to obtain higher selectivity towards propylene, the smaller dimension needs to be reduced.

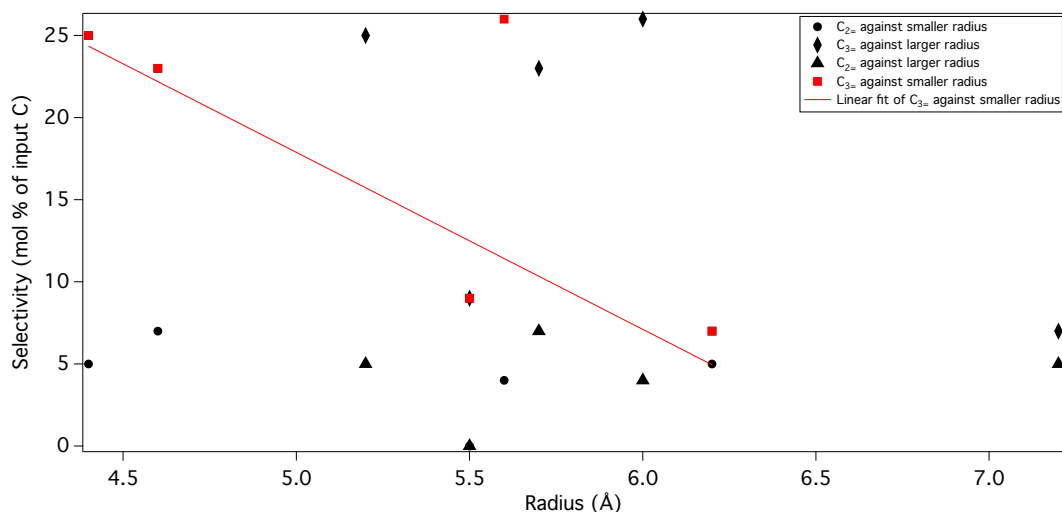


Figure 9-3 Maximum Selectivities to ethylene and propylene plotted against channel dimensions.

Finally, the same data was plotted against eccentricity to understand if this was a key factor. These data are shown in figure 10-4 below. Here, it seems that there is no consistent trend with regards to the maximum selectivities towards ethylene and propylene as a function of the channel eccentricity. Thus, given these data, the effect of the eccentricity of the channel on the product selectivity in the methanol-to-olefins reaction is inconclusive. Thus for the remaining studies in this thesis, circular channels were used.

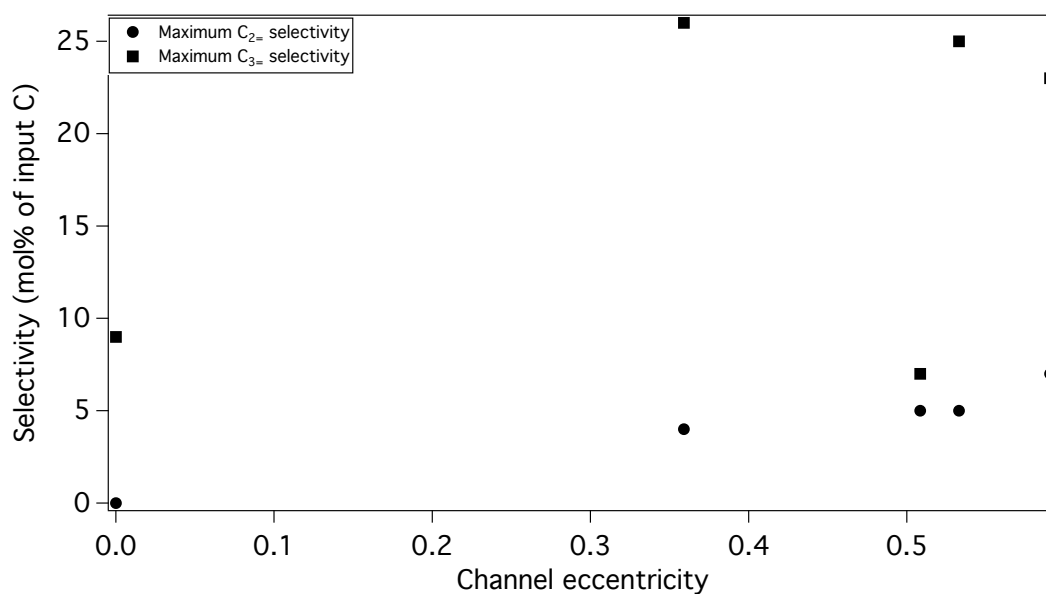


Figure 9-4 Maximum selectivities to C₃₌ and C₂₌ for channels of varying eccentricity

9.3 Conclusions

This chapter looked at the effect of changing channel size and channel shape (through different eccentricities of the circles formed by the channels) on the product selectivities in the MTO reaction. A set of 6 aluminosilicate structures were made that contained 1-D channels. These channels were of varying widths and eccentricities. Their behavior under the MTO reaction was studied. This information was desired in an attempt to understand if confinement effects could allow stabilization of intermediates in a fashion that would increase the selectivity towards light olefins. It was seen that there was a trend of increasing selectivity to propylene by reducing the semi minor axis of the channel. However, when looking at the eccentricity of the channel as a whole, no trend was found. Further studies could have been conducted to analyze the effects of varying catalyst and reaction parameters on the selectivity to ethylene and propylene in the reaction. For instance, a better understanding of the confinement effects could result if a full study of WHSV effects and Si/Al effects were studied, similar to the H-ZSM-5 work. This could have been done on ZSM-12 and ZSM-23, both of which can be made in a range of Si/Al ratios. For example, analogous to the experiment by Chang et al. on H-ZSM-5, if keeping the same flowrate of methanol normalized per acid site under different concentration, WHSV or Si/Al ratio results in differing selectivities, then this would offer insight on the preferred products under differing reaction parameter regimes. However, given that the overall results from this preliminary survey did not show an extensive change in selectivity due to changes in the channel parameters, focus was shifted to cage type structures (seen in the next two chapters).

9.4 Bibliography

- (1) Olsbye, U et al.; *Angew. Chem. Intl.* **2012**, *51*, 5810-5831
- (2) Bjørgen, M.; Svelle, S.; Joensen, F.; Nerlov, J.; Kolboe, S.; Bonino, F.; Palumbo, L.; Bordiga, S.; Olsbye, U. *Journal of Catalysis* **2007**, *249*, 195–207.

- (3) Gounder, R.; Iglesia, E. *Acc. Chem. Res.* **2012**, *45*, 229–238.
- (4) Laesthege, D.; Van Speybroeck, V.; Waroquier, M. *Phys. Chem. Chem. Phys.* **2009**, *11*, 5222-5226
- (5) Chen, P. C.; Wu, C. W. *The Journal of Physical Chemistry* **1995**, *99*, 15023–15027.
- (6) Chang, C.D.; *Catalysis Reviews*, **1983**, *25*, 1-118
- (7) Wu, X; Abraha, M. G.; Anthony, R. G.; *Applied Catalysis A*, **2004**, *260*, 63-69
- (8) Ilias, S; Bhan, A; *Journal of Catalysis*, **2012**, *290*, 186-192
- (9) Chang, C.D.; Chu, C. T-W.; Socha, R. F.; *Journal of Catalysis*, **1984**, *86*, 289-286
- (10) Plank, C. J.; Rosinski, E. J.; Rubin, M. K. Crystalline zeolite ZSM-23 and synthesis thereof US Patent 4,076,842 **1976**.
- (11) Verduijn, J. P.; Martens, L. R. M. ZSM-22 zeolite, US Patent 5,783,168 **1996**.
- (12) Valyocsik, E. W. Synthesis of crystalline silicate ZSM-48, US Patent 4,585,747 **1984**.
- (13) Zones, S. I. Zeolite SSZ-41, US Patent 5,591,421 **1994**.
- (14) Kühl, G. H. Synthesis of ZSM-12 zeolite, US Patent 4,559,213 **1984**.
- (15) Zones, S. I.; Rainis, A. Methods of using zeolite SSZ-42, US Patent 5,653,956 **1997**.

Chapter 10 Effect of cage size variation[#]

10.1 Introduction

For this section, the sizes of the cages in structures were varied to understand the effect of the cage size in the presence of a “restricted” 8-MR window. In the previous section, the effect of varying the width and eccentricity of a 1-D channel on the selectivity and conversion of the MTO reaction was studied. In this section, the effect of size (length) of cages on the selectivity and conversion of the MTO reaction was studied.

To deconvolute the effect of other catalyst parameters on the selectivities to light olefins in the MTO reaction, care had to be taken to ensure that these parameters were kept the same across all the frameworks studied. As alluded to in the previous section, the acid site concentration in the catalytic materials affects the selectivity towards various products in the MTO reaction. This is shown in Figure 9-11 for MFI zeolite. As such this was one of the catalyst parameters that was kept constant in this study. In addition to literature evidence¹, experiments conducted as part of initial studies for this work also showed that the size of crystal aggregates affected data obtained from running the MTO reaction on them.

Zeolite HSSZ-13 materials were made with varying aggregate crystal sizes using different literature recipes^{2,3}. All the materials had crystal Si/Al compositions between 14-17. This ensured that the effects being observed were not once again due to acid site concentration variation. SEM images of the resulting aggregates are shown in Figure 11-1. The resulting CHA crystal aggregates form aggregates that span two orders of magnitude.

[#] Originally published in ACS Catalysis DOI: 10.1021/cs300558x

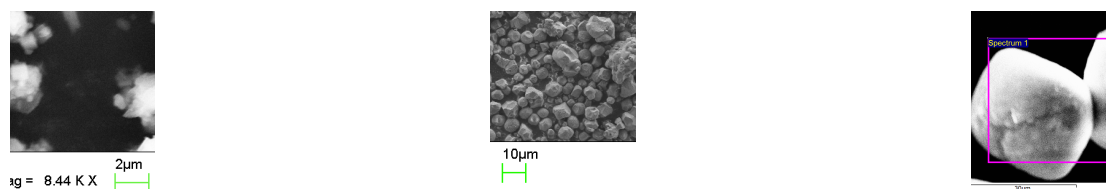


Figure 10-1 Aluminosilicate CHA of varying crystal aggregate sizes

One caveat of the characterization employed above is that the aluminium distribution in the crystals is assumed to be homogeneous. The reported Si/Al ratios are the bulk compositions of the solids as measured by EDS. There is a possibility, based on literature evidence^{4,5}, that there is a non-homogeneous distribution of Al throughout the individual crystals, resulting in higher acid site concentrations near the surface of the crystals. Especially in the case of the larger crystals, which would have stronger diffusion limitations, this could result in selectivity and conversion trends analogous to a higher aluminum material. Ideally, these materials would have been controlled for their surface aluminum contents by measuring this value through a surface-probing technique, and comparing this value to the bulk value. However, as these data were not available, the composition was taken at face value, and it was assumed that the surface aluminium content would not be very different from the bulk aluminum content.

These materials as catalysts for the MTO reaction yielded similar selectivities and conversions, but with varying catalyst lifetimes on stream. The trend that was observed on the lifetimes of the catalysts was as expected. The larger the crystal aggregates, the larger the diffusion limitations on the reactants into the catalyst and products out of the catalyst. The lack of difference in selectivities and conversion as a function of time on stream would also suggest that the assumption made about the extent of aluminum localization close to the surface of the crystal was minimal. As seen in early work as part of this study, materials with high aluminum content ($\text{Si/Al} < 5$) often result in very rapid deactivation, and very low selectivities. This was not observed in the materials in this study. One possible interpretation of this is that the variations in aluminum content were not significant enough to rapidly coke the outer layer of

the zeolite crystals, preventing access to the core of the crystal. This would have resulted in a deactivation profile similar to materials with a higher aluminum content throughout the crystal.

A summary of the reaction data is presented in Table 11-1.

Aggregate Size	Maximum C ₂₌ Selectivity	Maximum C ₃₌ Selectivity	Catalyst Lifetime (time till conversion < 80%)
< 2 μ m	38%	41%	240 mins
1 – 10 μ m	42%	44%	220 mins
30 – 60 μ m	39%	42%	180 mins

Table 10-1 Reaction data from Aluminosilicate CHA of varying aggregate sizes

Thus, for this study, the crystal Si/Al, the primary crystallite size and the crystal aggregate size were kept the same. Synthesis recipes for aluminosilicate materials with these properties being the same were found. Then, once the effect of the cage size change in isolation was studied, the Si/Al ratio was varied across all three frameworks to see how the Si/Al variations affected the three different materials.

Here, we focus on how the size of a zeolite cage can affect the conversion of methanol and the selectivity towards ethylene and propylene production. We investigated zeolites with the LEV, CHA and AFX frameworks as all three topologies have cages that are accessed by 8MR pores (schematics of topologies are provided in the database of zeolite structures.^{6,7}). Previous work has revealed that variations in crystal parameters such as Al content in the zeolite^{8,9}, and crystallite size¹⁰ can alter the reactivity. Thus, we investigated the effects of cage size over a range of Si/Al ratio with small crystallite sizes.

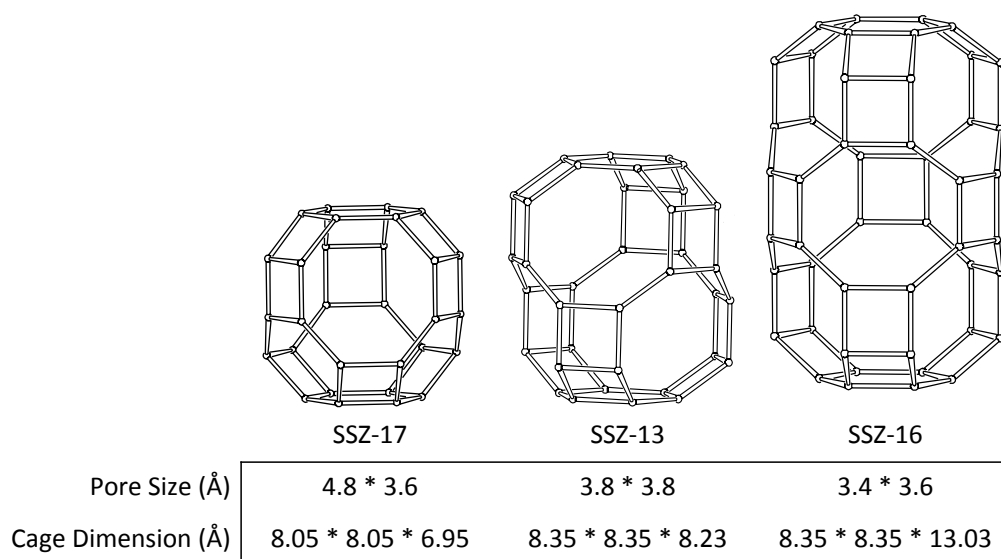


Figure 10-2 Cages in Zeolite framework study, dimensions obtained from IZA website

10.2 Materials & Methods

Organic structure directing agents

The organic structure directing agents (SDAs) required for the zeolite syntheses were prepared in-house. The LEV material was obtained using a N-methylquinuclidinium hydroxide SDA¹¹. The CHA material was synthesized with the N,N,N-trimethyl-adamantylammonium hydroxide SDA². The AFX material was crystallized using the 1,3-bis(1-adamantyl)imidazolium hydroxide SDA as described by Archer et al.¹²

Inorganic synthesis

Syntheses used to yield materials of desired crystal Si/Al were modified from known recipes.^{2,11,12}

LEV (SSZ-17) – A synthesis gel of the composition 1SiO₂:0.023Al₂O₃:0.2ROH:0.2NaOH:40H₂O was prepared with Cabosil M5 as the silica source, Reheis F2000 as the alumina source, and Baker NaOH pellets as the NaOH source (ROH is the SDA). The gel was loaded into a Teflon-lined autoclave and heated under autogenous pressure

at 170°C with tumbling. After 6 days, a crystalline product was recovered, washed with water and dried.

CHA (SSZ-13) – A synthesis gel of the composition $1\text{SiO}_2:0.026\text{Al}_2\text{O}_3:0.2\text{ROH}:0.2\text{NaOH}:40\text{H}_2\text{O}$ was prepared with Cabosil M5 as the silica source, Reheis F2000 as the alumina source, and Baker NaOH pellets as the NaOH source. The gel was loaded into a Teflon-lined autoclave and heated under autogenous pressure at 160°C with tumbling. After 5 days, a crystalline product was recovered, washed with water and dried.

AFX (SSZ-16) – A synthesis gel of the composition $1\text{SiO}_2:0.028\text{Al}_2\text{O}_3:0.25\text{ROH}:0.1\text{NaOH}:30\text{H}_2\text{O}$ was prepared with Cabosil M5 as the silica source, Tosoh HSZ320NAA (Zeolite Y, $\text{SiO}_2/\text{Al}_2\text{O}_3 = 5.5$; $\text{Na}_2\text{O}/\text{Al}_2\text{O}_3 = 1.01$) as the Al source, Baker NaOH pellets as the NaOH source. The gel was loaded into a Teflon-lined autoclave and heated under autogenous pressure at 150°C with tumbling. After 12 days, a crystalline product was recovered, washed water and dried.

Si/Al variation of the zeolites

In order to vary the Si/Al of the structures studied, two different approaches were used. For the CHA and LEV frameworks, compositional variations could be achieved by changing the amount of $\text{Al}(\text{OH})_3$ added to the synthesis gel. The AFX framework was not amenable to incorporating more aluminum using the same recipe. For the high aluminum SSZ-16 material, an alternative literature recipe¹³ was employed.

10.3 Results

The synthesized zeolites were analyzed by powder XRD and SEM/EDS. The syntheses used here yielded pure crystals of the desired structures based on comparisons of XRD patterns to reference patterns in the IZA database (figure 11-3). The primary crystallite sizes were measured from the XRD data using the Scherrer equation, and the results show that the sizes of the primary crystallites for all the materials were between 350-400 Å (Table 11-2). SEM images reveal that the primary crystallites form aggregate solid particles that are approximately 1-5 μm in size (

Table 10-2 and Figure 11-4). The AFX particles (3-5 μm) were slightly larger than the CHA and LEV particles (1-3 μm). EDS analyses of these materials yielded similar Si/Al ratios

that were between 14 and 17. A summary of the characterization data for the zeolites is shown in table 11-2. From the data listed in Table 11-2, it is clear that these materials are appropriate for examining the effects of cage size on the selectivity to lower olefins in the MTO reaction while holding all other properties relatively constant.

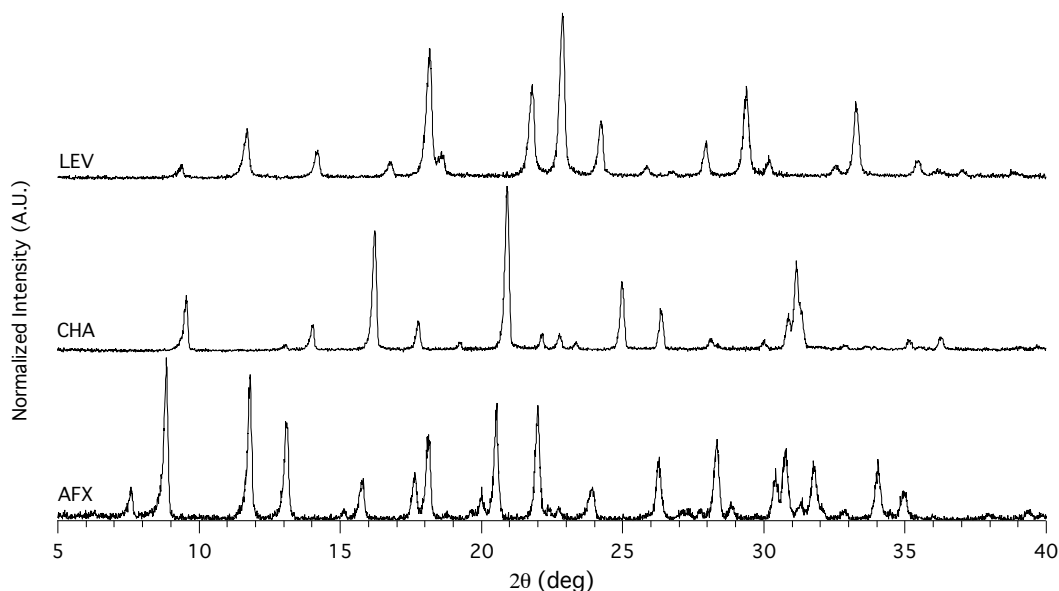


Figure 10-3 Powder XRD patterns from obtained zeolite materials

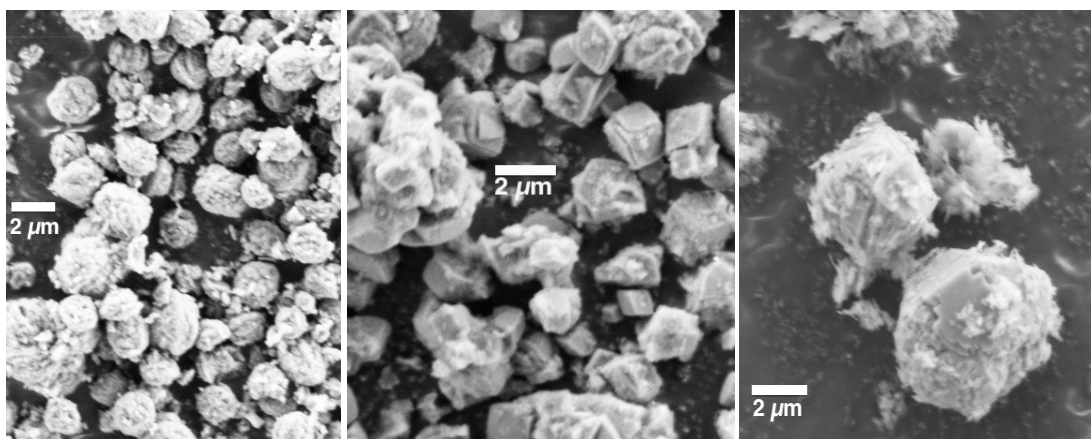
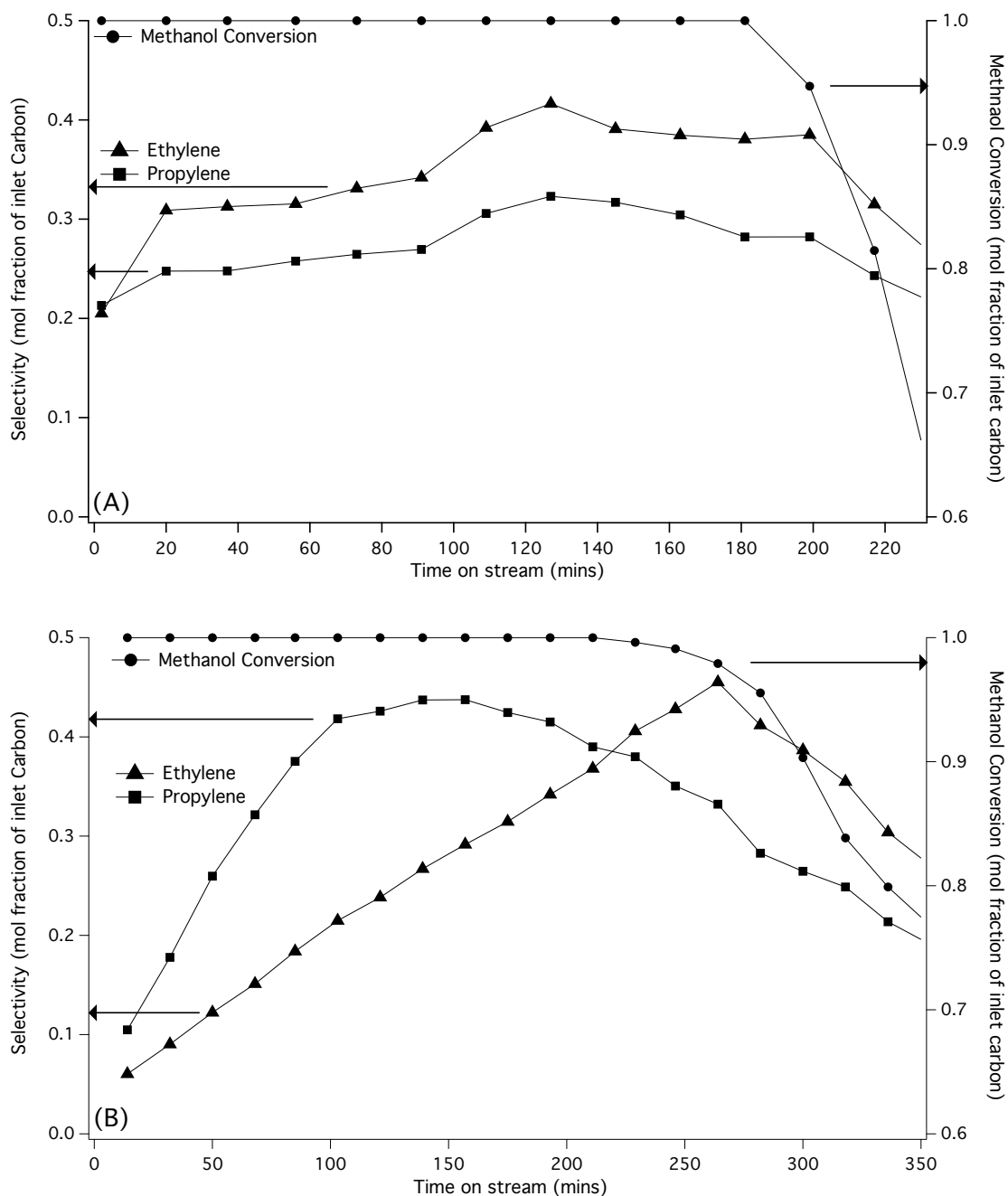


Figure 10-4 SEM images of the aggregates of the LEV(left panel), CHA (middle panel) and AFX (right panel)

Figure 11-5 illustrates the time-on-stream reaction data from the three different zeolites. These data show that the selectivity towards olefins increases over time when the conversion is at 100%, but rapidly drops once the conversion begins to decrease below 80%. The conversions

and selectivities for the AFX material rapidly decline after the 90 min on stream. Table 11-2 lists a summary of the reaction data for all three materials (the maximum ethylene, propylene, and maximum combined $C_2 - C_3$ olefin selectivities for the three frameworks studied).



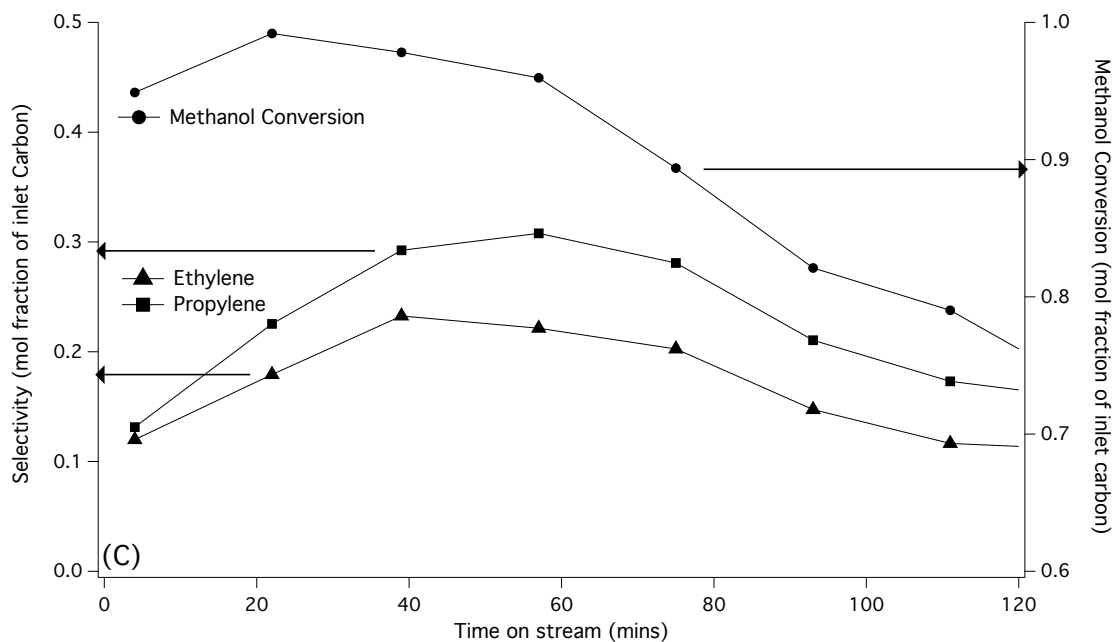


Figure 10-5 Time profiles for the MTO reaction on the LEV (A), CHA (B), and AFX (C) frameworks at 400°C, with WHSV = 1.3 h⁻¹

All three structures show a trend of selectivities changing with a function of time, however, CHA displays the most interesting trend of the three materials studied. LEV and AFX both show trends of selectivities increasing at the start of the reaction run, and upon conversion of methanol going below 80%, a decline in the selectivity towards ethylene and propylene. CHA, on the other hand, displays two regions of selectivity. Initially, propylene is being formed at a higher selectivity than ethylene. Throughout this period, the ethylene selectivity builds continuously until there is a crossover, and ethylene is the dominant product. Once conversion falls below 100%, the selectivity to both ethylene and propylene (similar to what occurred with the other structures) decline rapidly.

There are several possible explanations to the rise in ethylene selectivity as a function of time on stream. One possible explanation for the continuous buildup of ethylene selectivity is that as the carbonaceous species in the hydrocarbon pool get larger, there are space limitations for forming propyl branches off of the aromatic ring, and the ethyl branches get cracked off to yield higher selectivity to ethylene. Another explanation is a reduced concentration of surface methoxy species as the reaction progresses that would allow ethylene to be methylated to yield

propylene. Further characterization of the coked material would be required to determine if either of these are the reasons for the trend in ethylene selectivity.

The most apparent trend in the reactivity data is that the maximum ethylene selectivity increases as the cage size decreases. The LEV material is the only catalyst that produces more ethylene than propylene after 90 minutes on stream. The maximum propylene selectivity is the highest for CHA.

Framework	Si/Al	Aggregate Crystal Size (μm)	Primary Crystallite size (\AA)	Maximum $\text{C}_{3=}$ selectivity	Maximum $\text{C}_{2=}$ selectivity	Maximum (C_2+C_3) selectivity
LEV	16.8	1-3	389	32	43	69
CHA	14.4	1-3	364	44	46	79
AFX	16.7	3-5	395	31	23	53

Table 10-2 Characterization and results summary for the three materials

The AFX material has the shortest lifetime, and the worst carbon balance of the three materials studied. It deactivates much faster than the CHA and LEV materials, and at most, 53% of the methanol feed is recovered in ethylene and propylene. The amount of carbonaceous material deposited on the catalyst samples during tests was determined from thermogravimetric analysis. Figure 11-6 shows TGA data obtained from post-reaction samples for all three materials. AFX has the lowest amount of higher temperature mass loss, 1.3%-3.5% lower than CHA and LEV, respectively.

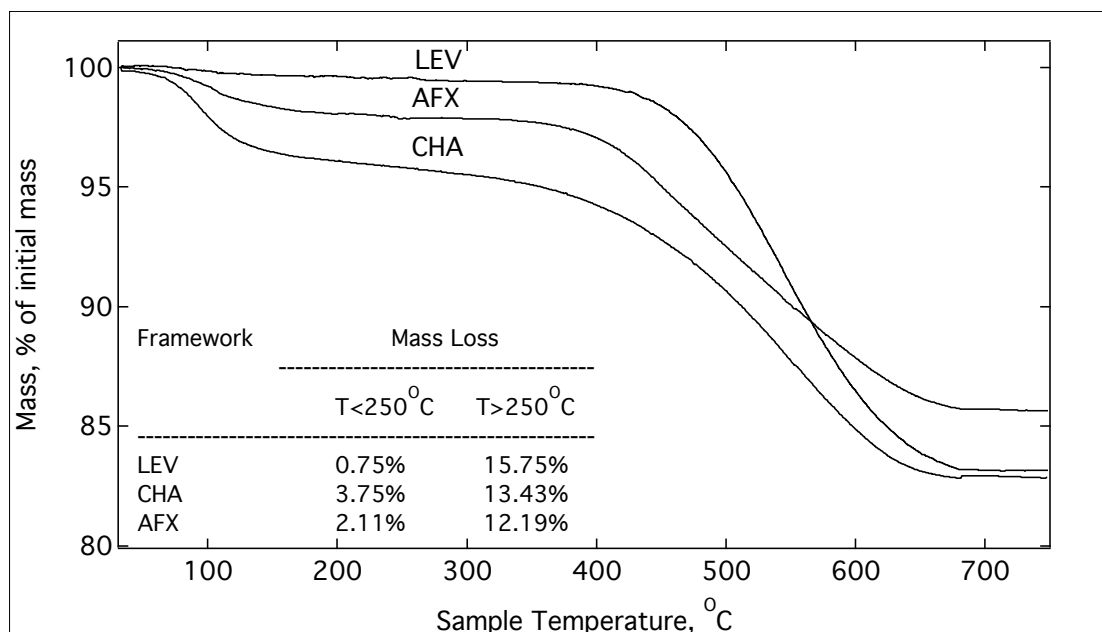
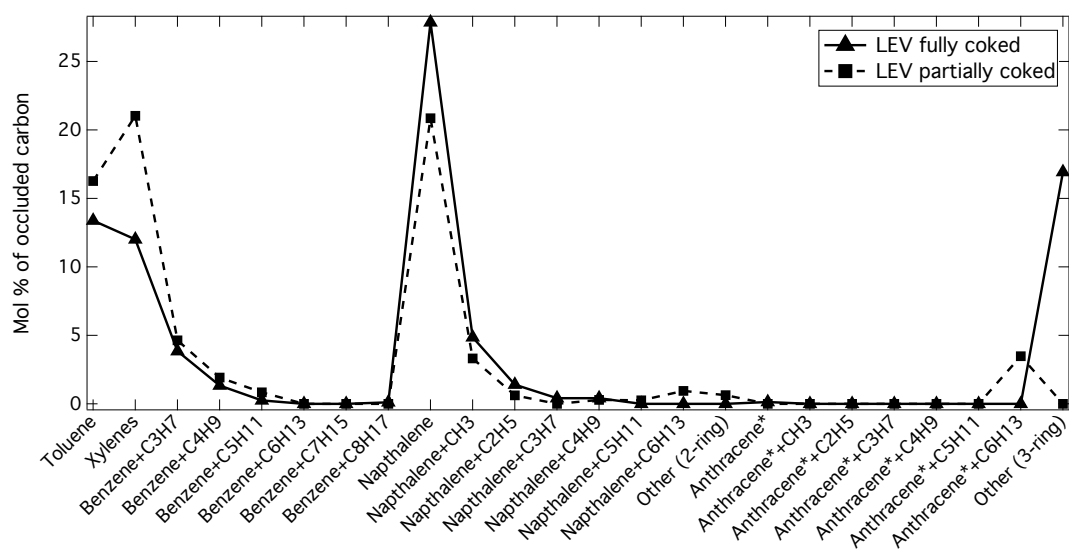


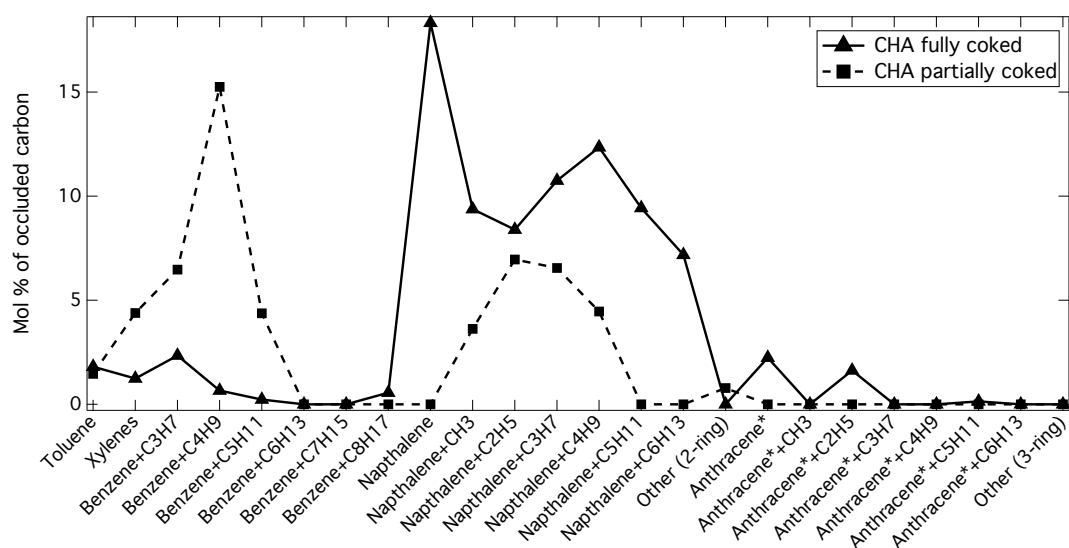
Figure 10-6 Thermogravimetric analysis of deactivated catalysts. Mass loss under 250°C was attributed to water removal, while mass loss above 250°C was attributed to organic removal.

Occluded Organic Analysis

In order to understand the carbonaceous buildup during the reaction and at the end of the catalyst lifespan, analyses of the occluded organic species were conducted at the time of maximum propylene conversion (see Table 11-3 for time on stream), and at the time of complete deactivation through HF dissolution of the zeolite framework. GC/MS data are presented in Figure 11-7. The GC/MS distribution data suggest that the carbonaceous species formed during the reaction are related to the size of the cavities present in the respective frameworks. LEV and CHA show a trend of forming light coked species first, and upon further deactivation, these light carbonaceous species (toluenes, xylenes, etc.) are converted to heavier carbonaceous species (higher alkylated benzenes and anthrones for LEV and alkylated naphthalenes for CHA). As the reaction proceeds, alkyl substituents are added to the hydrocarbon pool, and upon the formation of some critical concentration of these polyaromatic species, the catalyst deactivates.



(A)



(B)

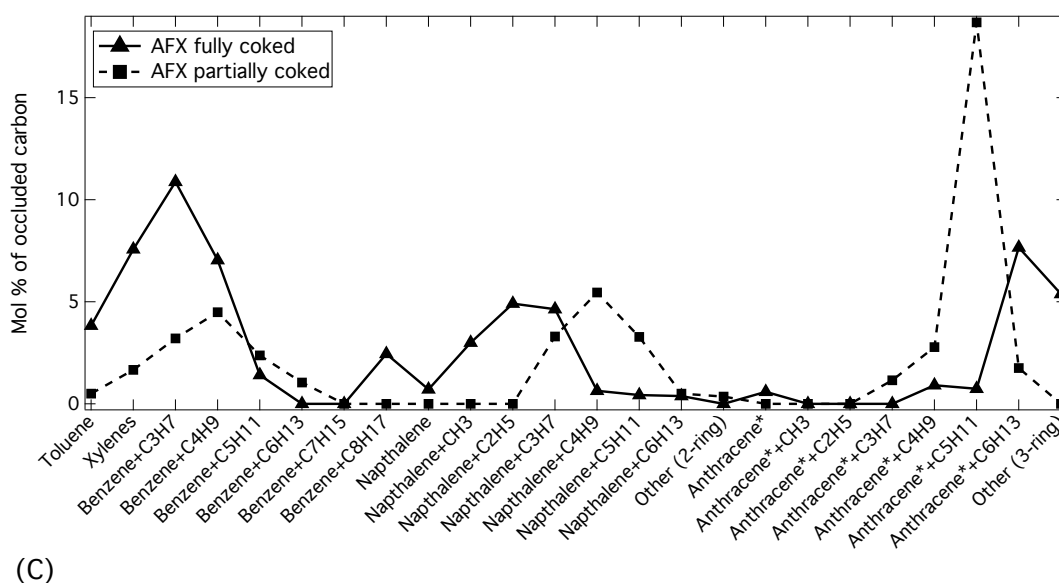


Figure 10-7 GC-MS data of occluded organic analyses of partially and completely deactivated catalysts for LEV (A), CHA (B), and AFX(C)

AFX, on the other hand, shows that larger organic species are formed first, and then the diminished remaining free cage volume is filled up with smaller organic molecules as the catalyst deactivates. This is seen in the increased organic content in the monoaromatic region upon complete deactivation that is absent in the partially coked material. These results suggest that the mechanism for coking of the AFX cage is different from the mechanism for coking of the CHA and LEV materials. That is, the large anthracene based molecules are formed relatively quickly in the AFX cages as the hydrocarbon pool builds up. We did not observe the formation of any significant amounts of four-ring or larger aromatic rings. Instead, the still available free space is filled with single ring aromatics and further alkylation products. Given the large size of these carbon pool molecules, the carbon balance is poor at the start of the reaction (42% by mol yield of C_1 - C_4 in the first 2 data points). However, upon formation of these anthracene species, further growth of aromatic structure is impaired. This hypothesis can be supported by estimating the volume of the larger AFT cage in the AFX structure (530 \AA^3), and comparing that with an estimated volume obtained from bulk density for a substituted

anthracene molecule (610 \AA^3). At this point, only cracking reactions can then proceed in the larger AFT cage, and any carbon buildup has to occur in the smaller GME cage.

	Partially Deactivated		Completely Deactivated	
	Time on stream (min)	Average MW of organic material	Time on stream (min)	Average MW of organic material
LEV	123	91	250	112
CHA	140	77	360	141
AFX	60	101	130	100

Table 11-3 Average molecular weights of occluded organics and time of removal from reaction stream for the three frameworks after partial and complete deactivation

The difference in coking mechanism is also observed in the average molecular weights of the occluded organic species as listed in Table 11-3. LEV and CHA continue increasing average molecular weight of the hydrocarbon pool as the reaction deactivates from the point of maximum propylene selectivity while the net pool stays approximately constant during the deactivation of the AFX structure. These details suggest that the AFX is deactivating due to pore blockage.

10.4 Si/Al variation study

Variations in the Si/Al ratio of the CHA and in LEV materials caused alterations in the primary crystallite sizes and the results are shown in Figure 11-8. Data in Figure 11-9 summarize the reaction selectivities as a function of Si/Al ratio. The data reveal that a Si/Al ratio between 14 and 17 gives higher selectivity to propylene for all three materials. The data show the importance of having the Si/Al ratio of the sample above a critical value (based on these data above 12), otherwise resulting in rapid deactivation and poor selectivities. This is most apparent in the AFX structure, as a higher Al content resulted in poor selectivity towards both ethylene and propylene.

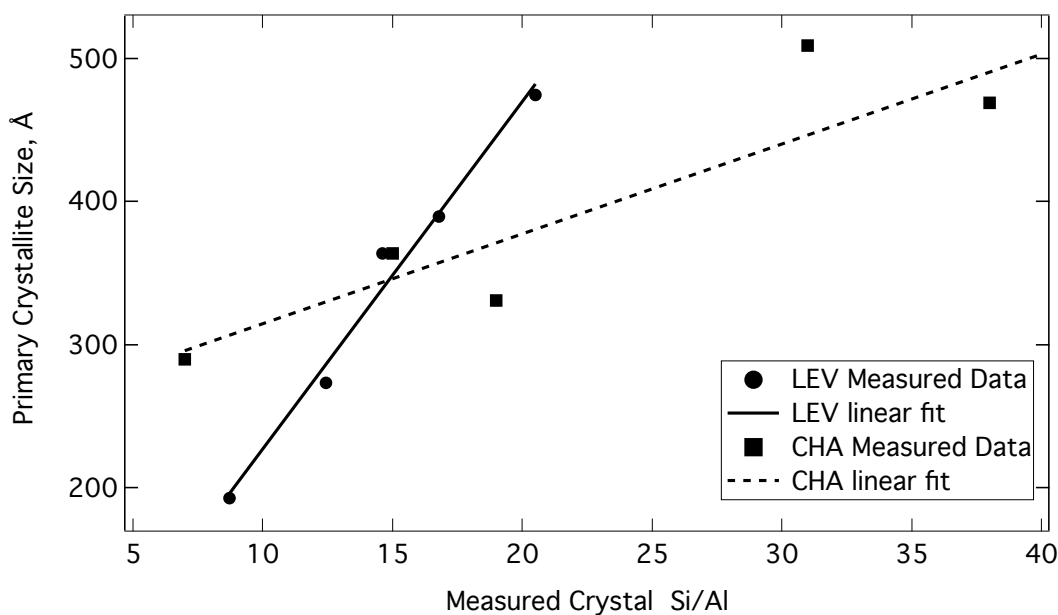


Figure 10-8 Primary crystallite sizes as a function of crystal Si/Al for LEV and CHA. The linear fits have R^2 values of 0.98 for LEV and 0.88 for CHA

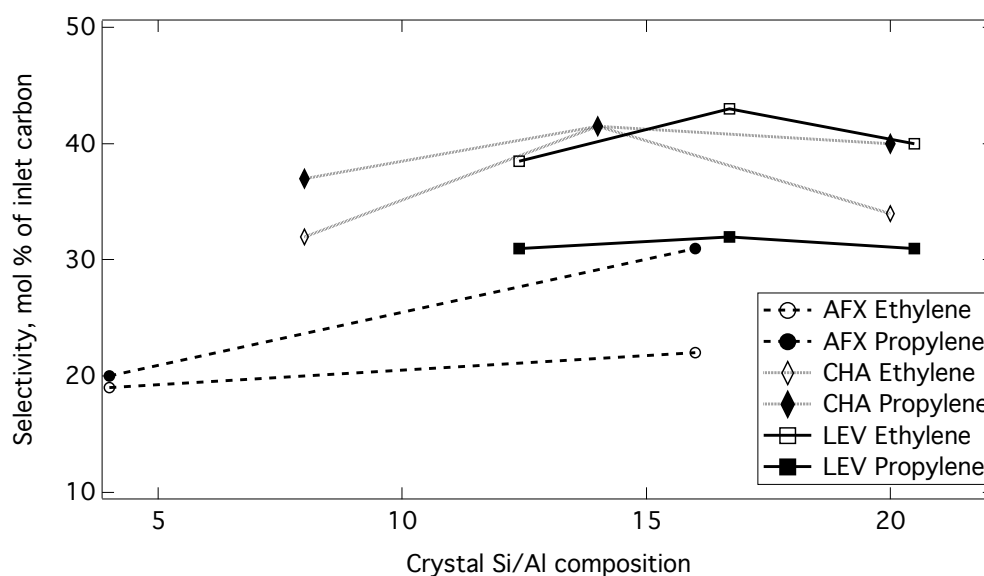


Figure 10-9 Maximum Ethylene and propylene selectivities throughout time profile for LEV, CHA and AFX for various crystal Si/Al ratios. LEV data taken between 120 mins – 150 mins, CHA taken between 160-200 mins and AFX data taken after 90 mins on stream.

In conclusion, zeolites with the LEV, CHA and AFX frameworks were used to study the effect of the cage size on the selectivity toward lower olefins in the methanol-to-olefins reaction. These materials all had cavities that were accessible through 8-membered ring windows, but had cavities of differing lengths. The aggregate crystal size, primary crystallite size and the Si/Al ratio were kept constant to study the effect of framework topology alone.

Reaction testing of these catalysts showed that the selectivity towards ethylene increased with a decrease in cage size. Propylene selectivity was highest with the CHA framework. The AFX material had the worst carbon yield and catalyst lifetime, but it also had the lowest amount of carbon deposited after complete deactivation, suggesting that there was pore blockage preventing further reaction. This interpretation is consistent with the analysis of the occluded organics, which showed that the AFX material formed large three-ring aromatics at maximum propylene selectivity, before the formation of smaller aromatics that filled the GME cage. Variation of the Si/Al ratio shows that the maximum selectivities were obtained at Si/Al of 14–17.

10.5 Bibliography

- (1) Lee, K.; Chae, H.; Jeong, S.; Seo, G. *Applied Catalysis A, General* **2009**, 369, 60–66.
- (2) Zones, S. Zeolite SSZ-13 and its method of preparation, US Patent 4,544,538 **1985**.
- (3) Zones, S. I.; Yuen, L. T.; Miller, S. J, Small Crystalline zeolite CHA, US Patent 6,709,644 **2004**.
- (4) Von Ballmoos, R; Meier, W. M.; *Nature*, **1981**, 289, 782–783
- (5) Althoff, R.; et al. *Microporous Materials* **1993**, 1, 207–218
- (6) *Database of Zeolite Structures*; Baerlocher, C.; McCusker, L. B., Eds.
- (7) Baerlocher, C.; McCusker, L. B.; Olson, D. H. *Atlas of Zeolite Framework Types*.
- (8) Inoue, K.; et al. *Catalysis Letters* **2010**, 136, 14–19.
- (9) Zhu, Q.; et al. *J Phys Chem C* **2007**, 111, 5409–5415.
- (10) Chen, D.; et al. *Microporous and mesoporous materials* **1999**, 29, 191–203
- (11) Zones, S. I.; Van Nordstrand, R. *Zeolites* **1988**, 8, 409–415.
- (12) Archer, R. H.; Zones, S. I.; Davis, M. E. *Micropor Mesopor Mat* **2010**, 130, 255–265.
- (13) Fickel, D.; Lobo, R. *The Journal of Physical Chemistry C* **2009**, 114, 1633–1640.

Chapter 11 Effect of framework composition variations

11.1 Objective

The objective of this section of the thesis is to understand the effect of changing the composition of the framework on the product selectivity in the methanol to olefins reaction. The most straightforward change in the framework composition is going from the aluminosilicate to the silicoaluminophosphate, for instance, comparing SAPO-34 to SSZ-13. In addition to a change in acid site strength¹, there is also a change in the nature of the surface going from silicate to aluminophosphate. The silicate structure is composed almost entirely of tetravalent atoms in a tetrahedral structure, with a small fraction of trivalent atoms, however the SAPO has large sections of the structure made up of alternating tri- and pentavalent atoms in the tetrahedral structure. This could potentially have an effect on the nature of the hydrocarbon pool and consequently product selectivities.

The effect of varying framework composition on product selectivity was studied by Yuen et al² for the CHA and AFI structures. They looked at alumino- and boro-silicates, and silicoaluminophosphates and magnesiumaluminophosphates. For the CHA structure, they found that the borosilicate analog was not acidic enough for the conversion, and, at 400°C, that the SAPO material gave a higher C₂-C₄ olefin selectivity, but lower propylene selectivity after 2 hours on stream. The runs presented in the work had water and nitrogen as diluents to the methanol inlet stream, while the runs presented in figure 12-1 only had methanol and helium/argon as the inlets. Based on the paper, incorporation of water increases the time before methanol breakthrough occurs, but does not mention anything about the specific olefin selectivities. Work by Wu and Anthony³ has shown that reducing water content in the feed not only reduces the time before methanol breakthrough occurs, there is also a much more pronounced time profile for the selectivities. Thus the data presented as part of this thesis could

thus still be consistent with the data from the Zones lab depending on the time at which the reaction was analyzed.

The motivation for this work comes from one of the first screening studies that was conducted as part of this project. In an attempt to understand the effect of reaction temperature on the selectivity towards ethylene and propylene, the data at 180 mins time on stream were compared. These data are shown below in figure 12-1. In general, what was observed was that the ethylene selectivity increased with increasing temperature, while the propylene selectivity increased with decreasing temperature. However, the increase in propylene selectivity was much more remarkable for SSZ-13 than for the SAPO-34. Since the objective for this project was to attempt to increase the selectivity towards propylene, the same comparison was done on all the structures reported thus far.

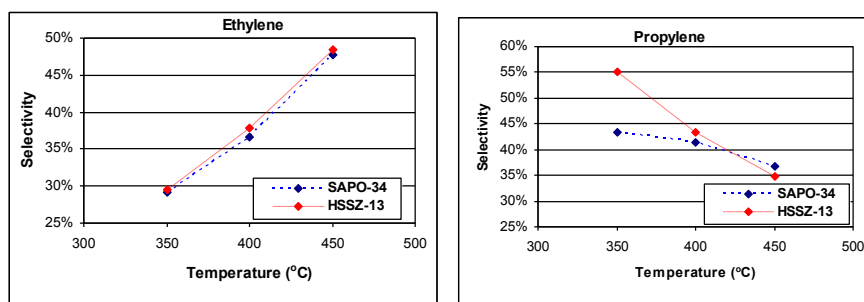


Figure 11-1 Reaction data from 180 mins TOS for SSZ-13 and SAPO-34 for Ethylene (left) and Propylene (right)

11.2 CHA

While the data shown in figure 12-1 suggest a dramatic change in the selectivity towards propylene at lower temperatures, they do not provide the complete picture with regards to selectivity differences. A time profile of the MTO reaction over SSZ-13 is shown below in figure 12-2. The strongly time-varying nature of the reaction profile causes the propylene to

ethylene ratio varies greatly. On a commercial scale this reaction would be carried out in a continuous fluidized bed reactor rather than a single pass fixed bed reactor, thus it may be possible to tune the extent of deactivation at which the catalyst is run. Therefore, the absolute maxima and minima of the $C_{3=}/C_{2=}$ ratio is a more relevant reflection of the selectivity differences on the various catalysts.

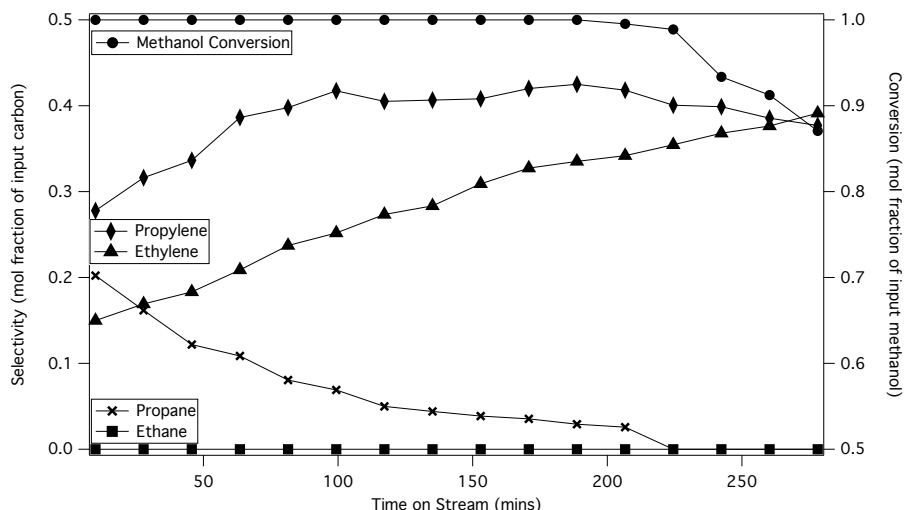


Figure 11-2 Time profile of MTO reaction on SSZ-13

The more appropriate comparison between SSZ-13 and SAPO-34 is shown in figure 12-3. The main trend that can be drawn from this is that for both the materials of the CHA structure, the $C_{3=}/C_{2=}$ ratio decreases with increasing temperature. SSZ-13 provides a wider range of accessible $C_{3=}/C_{2=}$ ratios than does SAPO-34. Given the complex nature of the reaction, it is difficult to hypothesize and test the precise change in mechanism that is occurring to cause this change in selectivities. One possible hypothesis consistent with this observation is that with an increase in temperature, the rate of cracking increases faster than the rate of methylation. However, in order to prove this, more detailed studies on the kinetics of these elementary steps must be conducted⁴.

One caveat to the data above is the issue of Si islanding. While the overall acid site concentration as measured by the silicon content in the SAPO seemed close to the aluminum content in the silicate, islanding could have an effectively lower acid site density. This is

because in the event of Si islanding, only the atoms on the “edge” of the silicon island would generate any sort of acidity. Thus, the bulk measure of Si content would not be an accurate gauge for the acid site concentration. One route to ascertain the extent of the Si islanding is to study the ^{29}Si -MAS NMR spectrum of the material. A ^{29}Si spectrum showed a large peak at -90 ppm, with a noticeable shoulder at -100 ppm. These peaks correspond to site isolated Si atoms, and species where the local coordination is $\text{Si}(\text{OSi})_3\text{OH}$, (the latter based on ^{29}Si NMR spectra of Aluminosilicate CHA), suggesting that there is some islanding present. Thus, the data presented here should be treated carefully given that the acid site concentration is not as high as perceived.

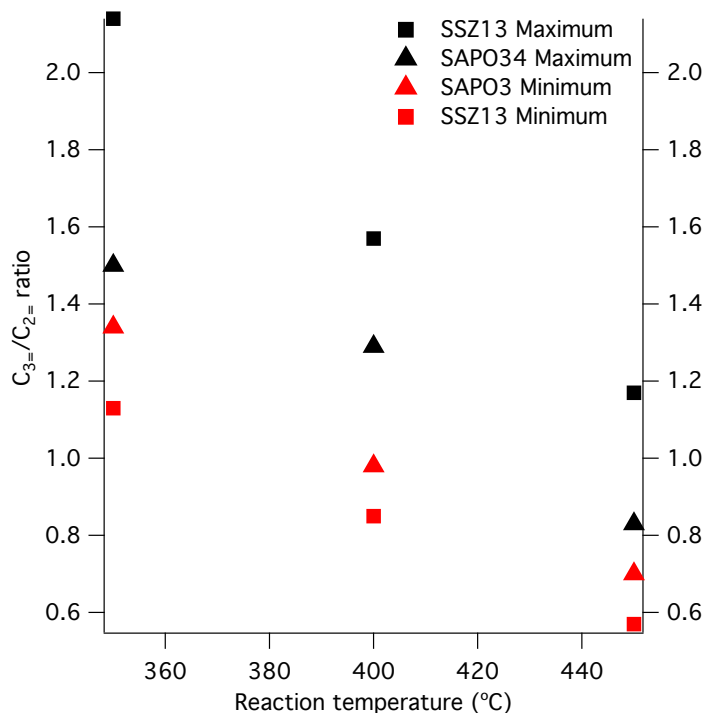


Figure 11-3 $C_{3=}/C_{2=}$ ratio for SSZ-13 and SAPO-34 at various reaction temperatures

11.2.1 Other silicate forms of CHA

In order to explore this effect of framework composition further, other materials with the CHA structure were also synthesized and reaction tested. The first material synthesized was Gallosilicate CHA. Based on literature evidence, isomorphous substitution of aluminum in a zeolite framework with gallium, iron or boron is known to affect the strength of the acid sites

that are generated⁵. This experiment would try to understand if varying the reaction temperature has the same effect on Gallosilicate CHA as it does on the aluminosilicate CHA. Rather than following the recipe used in the work from the Tatsumi group⁶ for the synthesis attempted in the lab, the recipe used to obtain aluminosilicate CHA was used with Ga₂O₃ instead of Al₂O₃.

This synthesis recipe had been described previously for the synthesis of SSZ-13 in the study of cage sizes. 1 SiO₂ : 0.044 Ga₂O₃ : 0.2 NaOH : 0.2 ROH : 44 H₂O. This works to give a Si/Ga ratio in the gel of 23. However, based on the work by the Tatsumi group, it was noticed that the crystal Si/Ga ratio closely followed the gel Si/Ga ratio, unlike the aluminosilicate material. Thus, a Si/Ga ratio closer to the desired Ga content (Si/Ga =15) in the crystal was chosen (Si/Ga = 12).

The synthesis was conducted under the same conditions as the aluminosilicate, 160°C with tumbling. The synthesis took longer than the aluminosilicate CHA synthesis (7 days instead of 5), and the yield was also poorer (65% rather than 80%) than aluminosilicate CHA. The resulting crystals showed an XRD pattern consistent with the CHA structure. An EDS analysis showed that the crystals had an Si/Ga ratio of 16, in the range of interest for the project. Thus, the catalyst was calcined, exchanged, and activated in the same way as the aluminosilicate catalysts described thus far.

The catalysts were then tested on the reactor at reaction temperatures ranging from 325°C to 450°C to understand the effect of temperature on this catalyst. A typical run on this catalyst is shown below in figure 12-4. This reaction was conducted at 350°C. The selectivity to olefins was poorer than the selectivity to olefins observed on an analogous aluminosilicate. However, the formation of saturated hydrocarbons at the start of the reaction was suppressed. The conversion also fell much more rapidly than in the aluminosilicate.

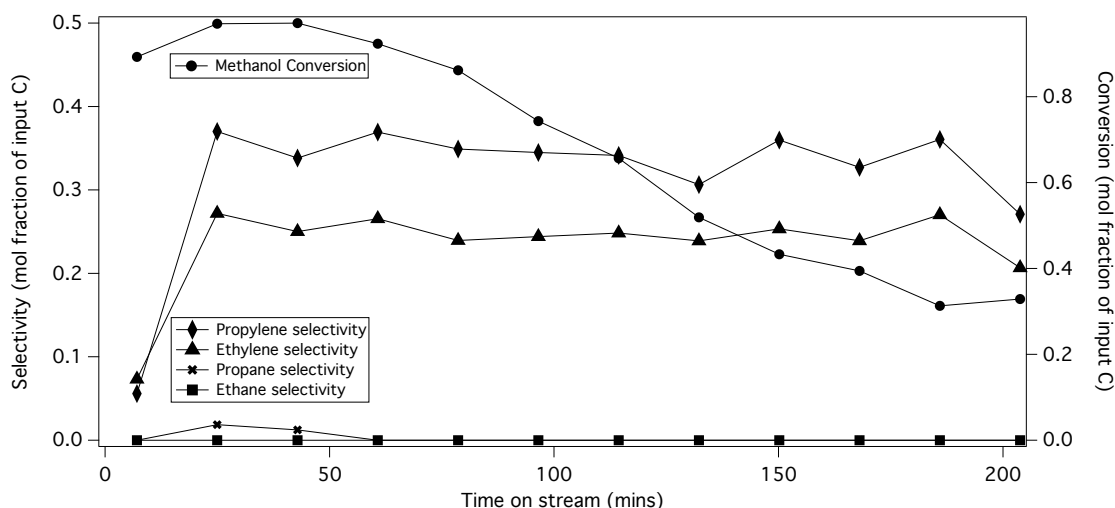


Figure 11-4 Reaction profile for Ga-CHA at 350°C

Figure 12-5 shows a summary of the change in $C_{3=}/C_{2=}$ ratio with temperature over the Ga-CHA catalyst. The catalyst could not be run at a temperature below 325°C, or above 400°C. The former case solely resulted in the dehydration of methanol to dimethyl ether while the latter case resulted in rapid deactivation and CO_2 production. The Ga-CHA does not show a smooth trend in the $C_{3=}/C_{2=}$ ratio as does the regular CHA material. The Ga-CHA does not show a marked improvement in the $C_{3=}/C_{2=}$ ratio at similar temperatures. At 350°C, the aluminosilicate CHA was able to produce a much higher $C_{3=}/C_{2=}$ ratio than the Ga-CHA. Thus, no marked improvement was noted by switching the catalyst composition from an aluminosilicate to a gallosilicate.

In addition to having a different acidity, gallosilicate materials are also known to promote other reaction pathways⁷. In particular these hydrocarbon processes are known to promote the formation of aromatic species over MFI type catalysts. Based on other studies⁸, both framework and extraframework Ga species are able to catalyze the cyclization process. In the case of CHA, this probably means that the alkylaromatic species that are part of the hydrocarbon pool mechanism for olefin formation. However, given that the pores are too small for the escape of these aromatic species, presumably there would not be a marked difference in

the product selectivity. This is in fact seen in the profile above, the hydrocarbon pool is rapidly formed, and a stable alkene production starts very early in the time profile.

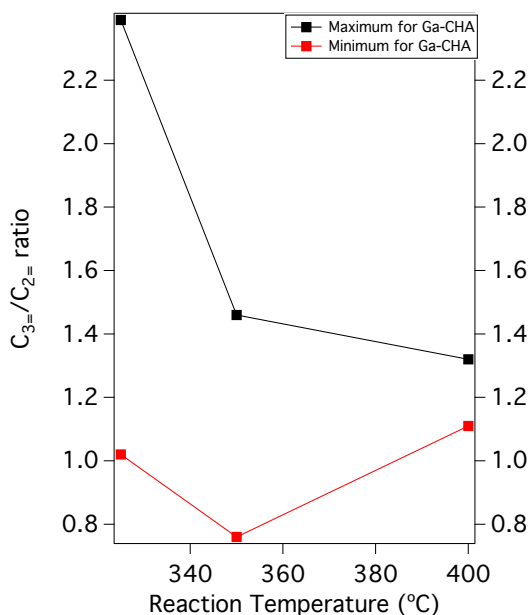


Figure 11-5 $C_{3=}/C_{2=}$ ratio for Ga-CHA at various reaction temperatures

In addition to the materials described here, several other heteroatom incorporations into the CHA structure were also tried. These attempts were not successful, and thus their data will not be presented here. However, before moving on to the next framework, a brief summary of the attempted structures, the reasoning behind trying these structures will be discussed.

One of the structures attempted was Zn-Al CHA. The hypothesis was to provide two kinds of sites in the zeolite structure. An acid site (provided by the aluminum) and an ion exchange site (provided by the Zn). It was shown in literature that the presence of a transition metal such as nickel^{9,10} in silicate structures allows oligomerization chemistry to occur on these metal sites. However, given the description in Chapter 9, the Brønsted acid sites are also critical for methanol-to-olefins chemistry. Thus, Zn-Al CHA was assumed to be a good route to try to obtain a material that showed both types of catalytic activity, and to understand whether this activity was tunable. The synthesis that was attempted was analogous to example 26 in the CIT-6 patent by Takewaki & Davis¹¹, with the substitution of N,N,N-

trimethyladamantanammonium hydroxide for tetraethylammonium hydroxide. The expectation was that since zinc is able to incorporate into a 4-ring rich structure such as *BEA, it should be able to incorporate into CHA (also rich in 4-rings). The synthesis yielded a material that had a powder XRD pattern consistent with CHA, with an additional peak at 5°. This peak was a layered lithium zinc silicate phase that had soaked up all the zinc in the synthesis gel. However, upon subjecting the as-made material to a dilute acid treatment, this peak, along with all the zinc in the solid material, had been removed. Several variations in the synthesis were attempted, including changing the alkali metal cation, using divalent ions to allow charge stabilization of zinc in the framework, but successful incorporation could not be confirmed.

Syntheses with tetrahedral atoms to reduce the effective cavity size were also attempted. The atoms attempted included atoms which were lewis acidic (such as Sn and Ti) to allow coordination of the pi-cloud electrons of the methylated benzene intermediates, and atoms such as Ge which would reduce the cavity size. The reason these atom replacements were attempted through direct synthesis was because all the cavities in CHA are bound by 8 membered rings, and thus due to the restricted pore size, no post-synthetic atom insertion or removal can be attempted. All of these syntheses were done by replacing some of the silicon content in the synthesis gel with the oxides of the atoms in question. All of the syntheses yielded pure-silica materials rich in defect sites. The remaining structures studied as part of this chapter were only made in the aluminosilicate and aluminosilicate forms.

11.3 LEV

In a similar vein to the first section of chapter 12.2, 12.3-12.5 will only focus on the comparisons between the aluminosilicate and the SAPO analogs of the LEV, AFX, AEI structures, respectively. The LEV structures compared were SSZ-17 and SAPO-35. The SSZ-17 synthesis was the same synthesis that was reported in chapter 11¹². The SAPO-35 synthesis that was used for this work was found in a work by the Kevan group¹³.

The SAPO-35 sample was worked up by calcining it in air, in situ in the reactor. The SSZ-17 sample was worked up in the same way as described in Chapter 11. The MTO reaction data was obtained at a range of temperatures. A summary of these data are shown below in figure 12-6. Unlike the temperature profile with the CHA or the Ga-CHA materials, the LEV structures (both the SAPO and the aluminosilicate) only show a weak temperature dependence. That is, the ratio of olefinic products cannot be controlled by changing the temperature of reactions.

Another key point from this figure is that this is the only structure where the SAPO material gave a higher $C_{3=}/C_{2=}$ ratio than the aluminosilicate for the temperatures studied. This was the only material studied where the minimum $C_{3=}/C_{2=}$ ratio for SAPO material was higher than the maximum $C_{3=}/C_{2=}$ ratio for the aluminosilicate material at all temperatures studied. In the studies conducted by Yuen et al.² and by Wilson and Barger¹⁴, on the aluminosilicate and aluminophosphate analogs of CHA, as well as the data reported above, typically the aluminosilicate has a higher $C_{3=}/C_{2=}$ ratio than the aluminophosphate. Given that this is only a slightly smaller cavity than the one associated with CHA, it is difficult to imagine why changing the size of the cavity would have as marked an effect on the reaction selectivity.

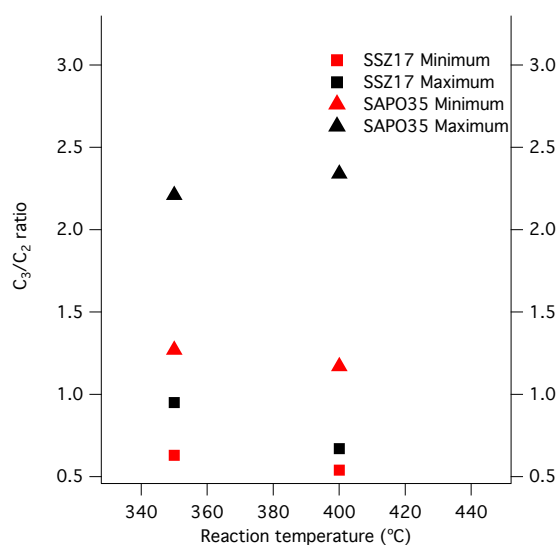


Figure 11-6 $C_{3=}/C_{2=}$ ratio for LEV at various reaction temperatures

11.4 AFX

The materials studied in this section are SSZ-16 and SAPO-56. SSZ-16 was made by the same protocol as described in chapter 11¹². SAPO-56 was made through a protocol described by S T Wilson¹⁵. It was found that the SAPO-56 crystals were particularly difficult to separate from the mother liquor, and so an acetone wash was required to induce phase separation. Both the materials yielded powder XRD patterns that were consistent with the AFX framework from the IZA Zeolites database¹⁶.

Once again, the material workup for the SAPO material was a simple in-situ calcination in medical grade air, while the aluminosilicate required a calcination, exchange, and activation procedure in order to activate it. Upon obtaining the material with Brønsted acid sites, the materials were then tested for Methanol-to-Olefins activity at the same range of temperatures, 350°C to 450°C. Unfortunately, the SAPO-56 material was not stable to the temperatures studied for an extended period of time. Only one reaction run at 400°C was attempted, and this yielded a minimum $C_{3=}/C_{2=}$ ratio of 0.77 and a maximum $C_{3=}/C_{2=}$ ratio of 1.04. This material had an (Al+P)/Si ratio of 27, with no estimate of the extent of islanding. However, the SSZ-16 material was stable to the various reaction conditions tested.

A summary of these data is presented in figure 12.7 below. There are some really interesting points with the SSZ-16 material. First, this is the only material synthesized and tested in this series that showed a positive relation in temperature and the $C_{3=}/C_{2=}$ ratio. While the minimum value for $C_{3=}/C_{2=}$ ratio on the SSZ-16 material does go through a maximum at 400 °C before reducing again at 350°C and 450°C, the maximum $C_{3=}/C_{2=}$ ratio shows a monotonic increase from 350°C to 450°C. The second interesting point from these data is that the maximum value for $C_{3=}/C_{2=}$ obtained is 4.1. The caveat with this piece of information is that this number was seen after the material had deactivated, that is, about 60% of the methanol

input was being dehydrated to dimethylether. While the oxygenate conversion was above 80%, the highest $C_{3=}/C_{2=}$ ratio observed was closer to 2.5.

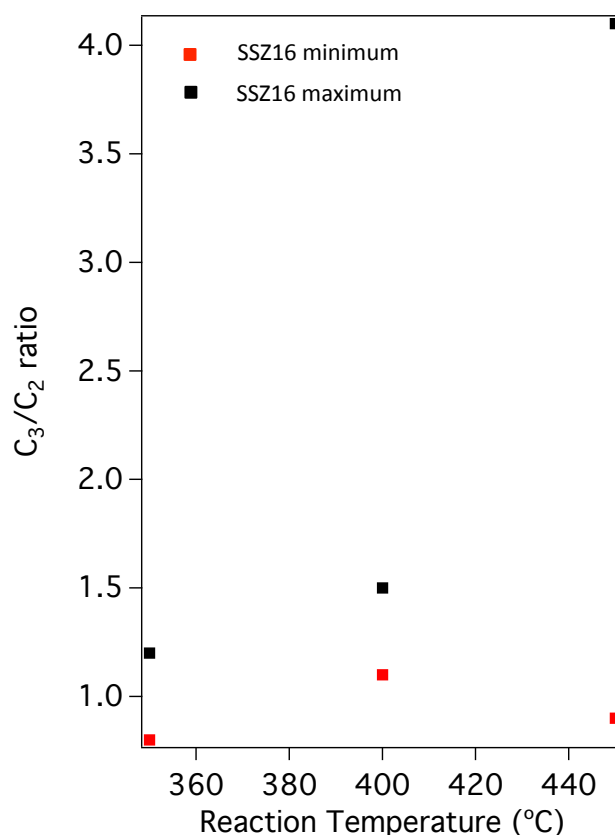


Figure 11-7 $C_{3=}/C_{2=}$ ratio for AFX at various reaction temperatures

This is of great interest as it provides one possible route to obtain a high propylene make in the product stream. However, the problem lies in the difficulty in synthesizing the AFX material. The synthetic difficulty lies in both the synthesis of the organic SDA, and the subsequent synthesis of a phase-pure crystalline product. If a more convenient method of synthesizing high – silica SSZ-16 can be found, this route to increasing the $C_{3=}/C_{2=}$ would be worth exploring further.

11.5 AEI

The final structure looked at as part of this composition variation study was the AEI structure. As this structure has not been looked at in the previous sections, figure 12-8 shows a caricature of the AEI cage. AEI is another member of the d6r family of zeolites. The cavity

pear shaped is bound by 6 8MR windows. The two materials used to study this structure are SSZ-39 and SAPO-18. The materials were synthesized based on literature procedures^{17,18}. The difficulty with synthesizing SSZ-39 lay in the formation of phase pure materials. Apart from the excess USY zeolite that was used as the aluminum source, there was often a phase impurity present. After obtaining a structure whose powder XRD pattern solely had the peaks associated with the desired AEI phase¹¹, and the unreacted USY, the solids formed were separated from the mother liquor, and were washed in a 0.01N HCl solution for 6 hours, with fresh the washing media being decanted off and fresh one being added every 2 hours. The acid wash mixture was held at 60°C. The solids obtained after this treatment showed only XRD peaks associated with the AEI structure. Both the SAPO-18 and the SSZ-39 were then worked up in a manner similar to the structures seen above.

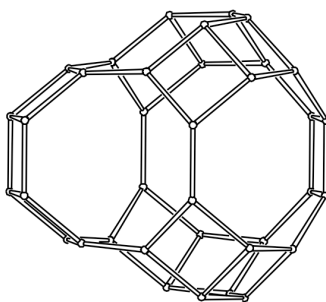


Figure 11-8 Caricature of AEI cage¹¹

Figure 12-9 shows a comparison of the MTO reaction of the two materials compared at different reaction temperatures. The first thing to note that is not presented in these data product mixture off of the SSZ-39 barely showed any aromatic products, thus supporting the assumption that there was not a significant amount of USY left at the end of the acid wash. Like CHA, and to a certain extent LEV, the AEI structure shows a negative gradient with temperature, for both the SAPO and the aluminosilicate. Apart from the highest temperature point over the AFX catalyst (which occurred after catalyst deactivation), the two low temperature points over the AEI material show the highest $C_{3=}/C_{2=}$ ratio of all the materials

tested. The AEI material is an easier structure to synthesize compared to AFX, and for these high $C_{3=}/C_{2=}$ ratios, it would be a preferable choice.

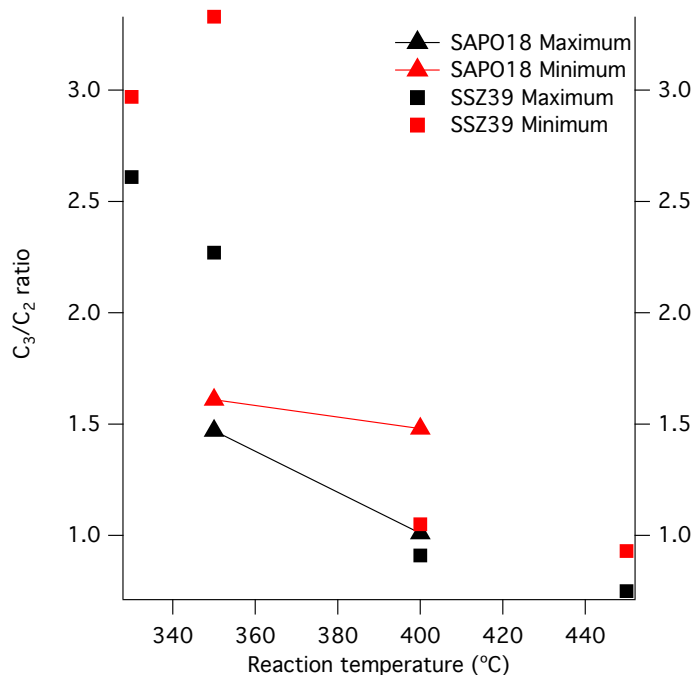


Figure 11-9 $C_{3=}/C_{2=}$ ratio for AEI at various reaction temperatures

11.6 Conclusions

This chapter contains a survey conducted of four cage-containing structures, and the effect of framework composition variations in these structures on the product selectivities in the methanol-to-olefins reaction. The general motif was the comparison of aluminosilicates and silicoaluminophosphates with the same frameworks. The most consistent trend seen for all three frameworks is that the temperature profile for the aluminosilicate follows the temperature profile for the silicoaluminophosphate. Apart from one framework (AFX) it was noted that all the frameworks showed the trend of reducing the $C_{3=}/C_{2=}$ ratio with an increase in reaction temperature. The highest $C_{3=}/C_{2=}$ ratio observed was with the AFX structure at 450°C. One possible hypothesis for this observation is a difference in activation energy of alkylation and cracking. Based on the reaction data, it could be that the rate of cracking increases relative to the rate of alkylation as the temperature increases. This would result in shorter branches being

formed on the aromatic species before they are cracked off, consequently resulting in a net lower selectivity towards propylene.

This could possibly suggest a lower activation energy for cracking than alkylation. However, given the overall reaction scheme consists of alkylation and cracking sequences on both the aliphatic and aromatic species. Since these 8-MR materials, in general open into larger spaces bound by 12-MR, or larger cavities, as an approximation, literature data on the alkylation and cracking rates in large pore zeolites can be studied. Work by Prof. Bhan's group¹⁹ shows that over H-*BEA, the activation energy for alkylating short olefins (up to C₄) is between 29 and 64 kJ/mol, and is inversely related to the length and degree of substitution of the alkyl chain. Based on data from experiments conducted over zeolite Y (thus, not providing an ideal comparison), the dealkylation of cumene has been shown by Best and Wojciechowski to have an activation barrier of 94 kJ/mol²⁰. Over H-*BEA, the activation energy for propylation of benzene by propylene has been reported to have an activation energy of 119 kJ/mol²¹. Thus, it would seem, that the conjecture that activation energy for cracking is lower than the activation energy for alkylation, is incorrect. This also holds with the observation that there is coke formation, but no alkenes detected in the MTO reaction over zeolites until 350°C, suggesting that a lower temperature is required for alkylation to proceed than is required for cracking to proceed. Further testing of potential alkylated benzenium species similar to what is done by the Bhan group is required to determine kinetic parameters to ascertain this.

The aluminosilicates in general gave a higher C₃₌/C₂₌ ratio than their corresponding silicoaluminophosphates. The only exception was the LEV structure, where the SAPO produced a higher C₃₌/C₂₌ ratio than the aluminosilicate.

The only caveat to all the data that have been presented in this section thus far is that these are all data from runs on "fresh" samples. The effect of calcination and regeneration on these samples is unclear, and thus it is critical to take these data with a grain of salt, as the

reaction profiles and the difference in selectivities may change through successive regenerations.

11.7 Bibliography

- (1) Bleken, F.; et al. *Top Catal* **2009**, 52, 218–228.
- (2) Yuen, L.-T.; et al. *Microporous Materials* **1994**, 2, 105–117
- (3) Wu, X.; Anthony, R. G.; *Applied Catalysis A*, **2001**, 218, 241–250
- (4) Hill, I. M.; Hashimi, S. A.; Bhan, A. *Journal of Catalysis* **2012**, 285, 115–123.
- (5) Cejka, J.; Zones, S.; Corma, A. *Zeolites and Catalysis*, Wiley-VCH: Weinheim, **2010**, 17.2, 494–498
- (6) Zhu, Q.; et al. *Micropor Mesopor Mat* **2008**, 116, 253–257.
- (7) Guisnet, M.; Gnep N.S.; Alario F.; *Applied Catalysis A* **1992**, 89, 1–30
- (8) Bayense, C. R.; van der Pol, A. J. H. P.; van Hooff, J. H. C.; *Applied Catalysis*, 72, **1991**, 81–98
- (9) Iwamoto, M.; Kosugi, Y. *J Phys Chem C* **2007**, 111, 13–15.
- (10) Bonneviot, L.; Olivier, D.; Che, M. *Journal of Molecular Catalysis* **1993**, 21, 415–430.
- (11) Takewaki, T.; Davis, M. E. Molecular sieve CIT-6, US Patent 6,521,206 **2004**.
- (12) Bhawe, Y.; et al. *ACS Catal.* **2012**, 2, 2490–2495.
- (13) Prakash, A. M.; Hartmann, M.; Kevan, L. *Chemistry of Materials* **1998**, 10, 932–941.
- (14) Wilson, S.; Barger, P.; *Micropor Mesopor Mat* **1999**, 29, 117–126
- (15) Wilson, S. T.; et al. *Studies in surface science and catalysis* **1995**, 98, 9–10.
- (16) *Database of Zeolite Structures*; Baerlocher, C.; McCusker, L. B., Eds.
- (17) Zones, S. I.; Nakagawa, Y.; Evans, S. T.; Lee, G. S. Zeolite SSZ-39, US Patent 5,958,370 **1999**, 1–13.

- (18) Chen, J.; et al. *The Journal of Physical Chemistry* **1994**, 98, 10216–10224.
- (19) Hill, I. M.; Ng Y. S.; Bhan, A. *ACS Catal.* **2012**, 2, 1742-1748
- (20) Best, D. A.; Wojciechowski B. W.; *J Catal* **1977**, 47:3, 343-357
- (21) Sridevi, U; et al.; *J. Molec. Catal. A*, **2002**, 181, 257-262

Chapter 12 Summary of frameworks studied

12.1 Objective

As part of this study of molecular sieve frameworks and their effect on product selectivity in the methanol-to-olefins reaction, a number of frameworks were synthesized, characterized and tested for their activity in the MTO reaction. These materials do not follow a coherent classification in the same way as the materials shown previously. The general theme for the materials reported here was to look through the zeolite structures database for materials that have 8-MR openings. This would prevent the formation of large amounts of aromatics as undesired products. Some of the materials that were tested did not fit this restriction. Second, the materials that were tested needed to have acid site densities low enough that they would not deactivate rapidly.

This chapter presents a compilation of all of these data that were collected as part of the initial survey on this project as well as attempts to run the reaction on more unconventional materials for this reaction. Chapter 13.2 shows a summary of the frameworks that were studied, the structures bearing those frameworks that were studied, and their critical dimensions. Chapter 13.3 looks at some of the more interesting cage-containing materials studied as part of this thesis. Chapter 13.4 then provides a more extensive summary of some of the more relevant reaction runs that were done on the materials considered for this reaction.

12.2 Summary of materials Table

Framework	Structure	Cage Shape	Cage size (Å)	Channel size (Å)
MFI	ZSM 5	Channel intersect	5.3*5.6 X 5.1*5.5	
CHA	SAPO 34 SAPO 44 SSZ - 13 SSZ - 62 Ga-SSZ-13	Ellipsoidal	6.7 X 10	3.8*3.8
RTH ITE-RTH	[B]-RUB-13 [Al]-TTZ1 SSZ - 50 SSZ - 36	Spherical	8.2*13.07*10.48	3*5 and 4
AEI	SAPO 18 SSZ - 39	Spherical	12.6*11.5*10.6	3.8
AFX	SSZ - 16 SAPO 56	Ellipsoidal	16.6*11.9*10.6	3.4*3.6
DDR	DD3R SSZ 28	Spherical+Ellipsoidal	8.9*8.3*8.6 (sp) 11.6*9.98*10.1 (ep)	4.4*3.6
ITW	ITQ 12	Ellipsoidal	7.4*10.5*11.96	5.4*2.4 and 3.9*4.2
SAS	SSZ - 73	Spherical	11.2*11.2*10.4	4.2
MER	MER	Ellipsoidal	6.87*12.33	7.48
LEV	LEV	Ellipsoidal	9.75*10.12	7.69
MWW	SSZ-25	Elongated with bulge (16.6)	22.18*10.46	9.05 and 9.45
STF	SSZ-35	Ellipsoidal	15.01*7.48	10.03
STI	SSZ-75	Channel Intersect	9.0*9.0 X 7.0*5.3	
LTA	ITQ-29 SAPO	Spherical	11.92*11.92*11.92	7.57*7.57
MTW	ZSM-12	Channel Only	5.6*6	
MTT	ZSM-23	Channel Only	4.5*5.2	
TON	ZSM-22	Channel Only	4.6*5.7	
IFR	SSZ-42	Channel Only	6.2*7.2	
*MRE	ZSM-48	Channel Only	5.5*5.5	
VET	SSZ-41	Channel Only	5.9*5.9	

12.3 Excerpts from study of structures

In this section, some of the more interesting structures will be explored for their product selectivities in the methanol-to-olefins reaction before proceeding to present a summary of the MTO data. The first material presented here is of the RTH framework, SSZ-50¹. The Tatsumi

group published results over a similar framework material that was synthesized through a template free media².

12.3.1 RTH

The synthesis was carried out with 1,2,2,6,6-pentamethylpiperidine as the template. The borosilicate molecular sieve was synthesized first, and the borosilicate material was used as seed material for the aluminosilicate, template free synthesis. The ratio of 0.87 SiO₂ : 0.11B₂O₃ : 1.73 Ethylenediamine : 0.55 pentamethylpiperidine : 105 H₂O was used for the synthesis of the seeds. The synthesis took 70 days at 160°C without agitation. These seeds were then used as 5% of the silicon source for the aluminosilicate synthesis. The aluminosilicate synthesis had the gel composition of 1 SiO₂ : 0.125 Al₂O₃ : 0.2 NaOH : 200 H₂O. This synthesis was conducted at 170°C. The resultant powder XRD pattern for the material is shown below in figure 13-1.

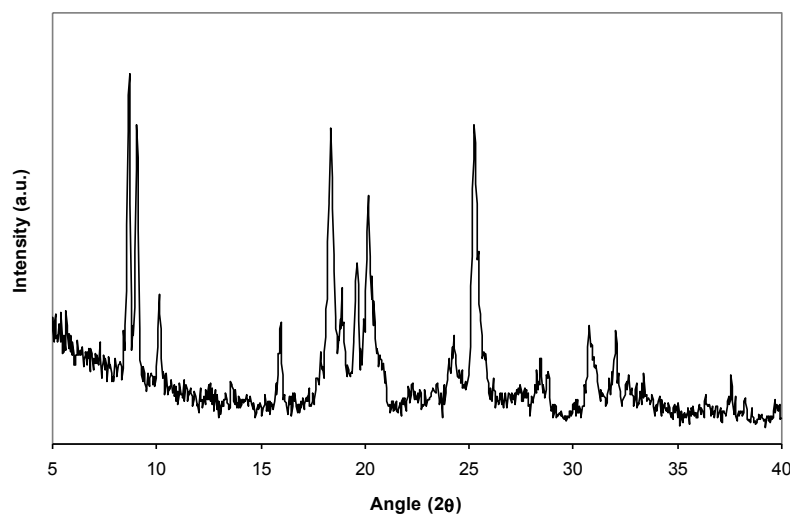


Figure 12-1 Powder XRD pattern for RTH material

The material was worked up in the same manner as the aluminosilicates presented in this thesis. The material was calcined in air to 580°C, then exchanged to the ammonium form with 1.0M NH₄NO₃ before being activated in-situ, in Ar. This material was then run on the MTO reaction. The time profile for the reaction at 400°C is shown below in figure 13-2.

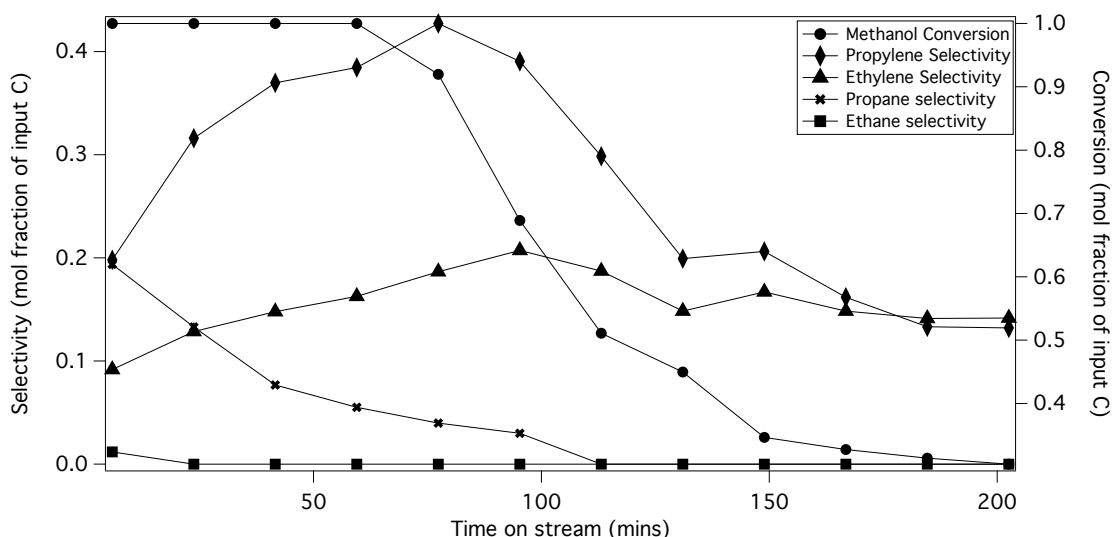


Figure 12-2 Reaction profile over RTH material at 400°C

In spite of the significant difficulties in obtaining this material, this material provides no significant advantage in terms of product selectivity. The maximum propylene selectivity observed is 42%, and the maximum ethylene selectivity observed is 21%. The reaction run at 350°C also did not improve the selectivities towards light olefins than some of the more conventional materials tested, such as SSZ-13 and SAPO-34.

12.3.2 ITE-RTH

The material chosen for this structure was SSZ-36. The material crystallizes as an intergrowth of the two related d6r frameworks, ITE and RTH. This material was synthesized using the protocol described by Wagner et al.³. This material had a Si/Al ratio that was in the desired range for activity in the MTO reaction. The reaction data from running the MTO reaction over this material at 400°C are shown below in figure 13-3. The main advantage seen in this catalyst was the high $C_{3=}/C_{2=}$ ratio at high conversion that was observed during the reaction. The reaction was able to yield a $C_{3=}/C_{2=}$ ratio as high as 4.3 at high conversion. The carbon balance was poor (< 60%) with most of the unaccounted products being dimethyl ether.

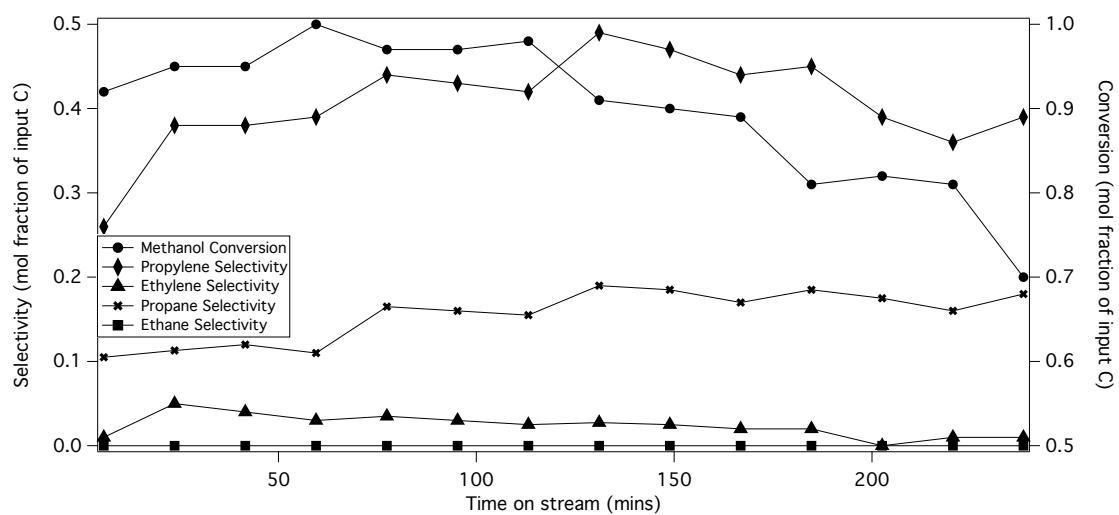


Figure 12-3 Time profile of MTO reaction over SSZ-36 at 400°C

12.4 Summary of Reaction Data

Material	Frame work	Si/ Al	Temp (°C)	Crystal Size (µm)	WHSV (1/h)	Conc (mol/ mol)	Conversion	Maximum C2 selectivity	Maximum C3 selectivity
SAPO-34	CHA		350	1	1.3	0.1	100	31	43
SAPO-34	CHA		400	1	1.3	0.1	100	42	41
SAPO-34	CHA		450	1	1.3	0.1	100	53	37
SAPO-44	CHA		350	5	1.3	0.1	50	8	8
SAPO-44	CHA		400	5	1.3	0.1	40	11	9
SSZ-13	CHA	15	300	5	1.3	0.1	100	20	42
SSZ-13	CHA	15	325	5	1.3	0.1	100	25	40
SSZ-13	CHA	15	350	5	1.3	0.1	100	38	52
SSZ-13	CHA	15	400	5	1.3	0.1	100	46	42
SSZ-13	CHA	15	450	5	1.3	0.1	100	51	39
SSZ-13	CHA	15	400	60	1.3	0.1	100	41	37
SSZ-62	CHA	14	350	1	1.3	0.1	100	34	47
SSZ-62	CHA	14	400	1	1.3	0.1	100	31	37
SSZ-13	CHA	20	400	5	1.3	0.1	70	30	39
SSZ-13	CHA	30	400	5	1.3	0.1	70	38	40
SSZ-13	CHA	80	400	5	1.3	0.1	70	31	37
SSZ-13	CHA	15	350	5	0.325	0.1	100	35	41
SSZ-13	CHA	5	400	5	1.3	0.1	100	21	31
SSZ-13	CHA	5	350	5	1.3	0.1	100	20	35
Ga-SSZ-13	CHA	15	300	1	1.3	0.1	0	0	0
Ga-SSZ-13	CHA	15	350	1	1.3	0.1	95	31	37
Ga-SSZ-13	CHA	15	400	1	1.3	0.1	65	10	12
Ga-SSZ-13	CHA	30	350	1	1.3	0.1	65	18	24
SSZ-16	AFX	4	400	5	1.3	0.1	100	18	21
SSZ-16	AFX	14	350	10	1.3	0.1	100	26	32
SSZ-16	AFX	14	400	10	1.3	0.1	100	22	31
SSZ-25	MWW	28	350	5	1.3	0.1	95	9	15
SSZ-25	MWW	28	400	5	1.3	0.1	100	11	14
SSZ-35	STF	75	350	5	1.3	0.1	100	1	13
SSZ-35	STF	75	400	5	1.3	0.1	100	2	23
SSZ-35	STF	75	450	5	1.3	0.1	100	4	19
SSZ-36	ITE-RTH	14	350	10	1.3	0.1	86	10	13
SSZ-36	ITE-RTH	14	400	10	1.3	0.1	100	23	45
SSZ-36	ITE-RTH	14	450	10	1.3	0.1	95	20	25
SSZ-36	ITE-RTH	14	350	10	0.65	0.1	95	15	26
SSZ-50	RTH	14	350	1	1.3	0.1	50	10	12.4
SSZ-50	RTH	14	400	1	1.3	0.1	92	32	40.8
SSZ-75	STI	38	350	10	1.3	0.1	0	0	0
SSZ-75	STI	38	400	10	1.3	0.1	100	3	26
SSZ-75	STI	38	450	10	1.3	0.1	0	0	0
SSZ-17	LEV	14	285	5	0.325	0.1	90	2	10
SSZ-17	LEV	14	300	5	0.65	0.1	90	20	20

SSZ-17	LEV	14	350	5	0.325	0.1	99	28	36
SSZ-17	LEV	14	350	5	1.3	0.1	90	41	36
SSZ-17	LEV	14	400	5	1.3	0.1	100	38	32
SSZ-17	LEV	14	400	5	0.325	0.1	93	15	10
		28.							
ZSM-5	MFI	3	450	5	1.3	0.1	100	10	25.6
ZSM-5	MFI	560	350	5	1.3	0.1	100	8	40.7
ZSM-5	MFI	560	400	5	1.3	0.1	100	12	38.4
		21.							
ZSM-5	MFI	2	400	5	1.3	0.1	100	6	14.9
ZSM-22	TON	51	325	5	1.3	0.1	0	0	0
ZSM-22	TON	51	350	5	1.3	0.1	100	2	24
SSZ-41	VET	50	400	5	1.3	0.1	0	0	0
SSZ-42	IFR	24	350	1	1.3	0.1	0	0	0
SSZ-42	IFR	24	400	1	1.3	0.1	82	4	11
SSZ-42	IFR	24	450	1	1.3	0.1	67	0	9
ZSM-23	MTT	35	350	1	1.3	0.1	95	2	19
ZSM-23	MTT	35	400	1	1.3	0.1	100	4	20
ZSM-23	MTT	35	450	1	1.3	0.1	100	0	0
ZSM-12	MTW	39	350	5	1.3	0.1	100	4	26
ZSM-12	MTW	39	400	5	1.3	0.1	98	3	25
ZSM-12	MTW	39	450	5	1.3	0.1	100	0	0
ZSM-48	*MRE	80	350	5	1.3	0.1	0	0	0
ZSM-48	*MRE	80	400	5	1.3	0.1	65	0	9
SAPO-18	AEI		325		1.3	0.1	100	0	0
SAPO-18	AEI		350		1.3	0.1	100	26	39
SAPO-18	AEI		400		1.3	0.1	100	30	32
SAPO-18	AEI		450		1.3	0.1	100	26	40
SSZ-39	AEI	11	325	5	1.3	0.1	100	10	31
SSZ-39	AEI	11	350	5	1.3	0.1	100	13	40
SSZ-39	AEI	11	400	5	1.3	0.1	100	41	41
SSZ-39	AEI	11	450	5	1.3	0.1	69	12	11
SAPO-35	LEV		350	5	1.3	0.1	97	18	26
SAPO-35	LEV		400	5	1.3	0.1	99	19	24
SAPO-56	AFX		400	5	1.3	0.1	100	39	34
SAPO LTA	LTA		350	20	1.3	0.1	0	0	0
SAPO LTA	LTA		400	20	1.3	0.1	89	4	5

12.5 Ideal Cage

Given all the data that had been collected as part of this project, an attempt was made to calculate an “ideal cage”. The procedure followed was as follows. The dependent variables that were selected were the averages of the maximum and minimum $C_{3=}/C_{2=}$ ratios for each material.

The independent variables selected were parameters associated with the structure being studied, along with the reaction conditions. In an effort to simplify the model, the only reaction condition considered was the temperature of the reaction, since, as seen in chapter 12, this parameter had proven to have an influence on the $C_{3=}/C_{2=}$ ratios. The structure parameters studied were the 3 radii associated with each cage, the eccentricities of the ellipses formed by the cross section of each cage, the concentration of acid sites, the number of cages bound by each individual cage (seen as in indication of extent of sharing of acid sites between multiple cages), and the number of tetrahedral atoms in each cage.

As with the other data presented thus far in this thesis, there are several caveats to the data set that was selected to try to build a model from. First, the acid site concentration was given by the fraction of the T-atoms that generate acid sites, as measured by EDS measurements. These bulk measurements may not portray the true acid site count in the solid sample. Second, the effect of structure on solely the aluminosilicate materials is considered, as the measurements required to determine acid strength differences between SAPO, aluminosilicate and Gallosilicate materials were not taken, and thus the picture presented here only shows the aluminosilicate behavior. Third, and most importantly, the several models shown here are not exhaustive, as the search for the best fit was conducted manually. A more accurate model could be determined should more computationally intensive tools be used.

The numerical fitting of a number of expressions was manually attempted. The structures considered were the aluminosilicate analogs of the AEI, AFX, CHA, LEV and RTH structures. The best fit was obtained by plotting the average $C_{3=}/C_{2=}$ ratio against the following expression:

$$\frac{C_{acid\ sites}}{\left(\exp\left(\frac{1}{T_R}\right)-1\right)*T_{atoms}*N_{Shared\ cages}} \quad (13-1)$$

The plot is shown below in figure 13-4. Excluding the 3 outliers yields a fit with an R^2 value of 0.83. In the expression above, T_R refers to the reaction temperature, in °K, $C_{acid\ sites}$

refers to the fraction of T atoms that are acidic (in the case of aluminosilicates, this is $1/(1+\text{Si}/\text{Al})$). T_{atoms} refers to the fraction of tetrahedral atoms in the key cage in the structure, and $N_{\text{shared cages}}$ refers to the number of smallest cages that share atoms with the cage in consideration.

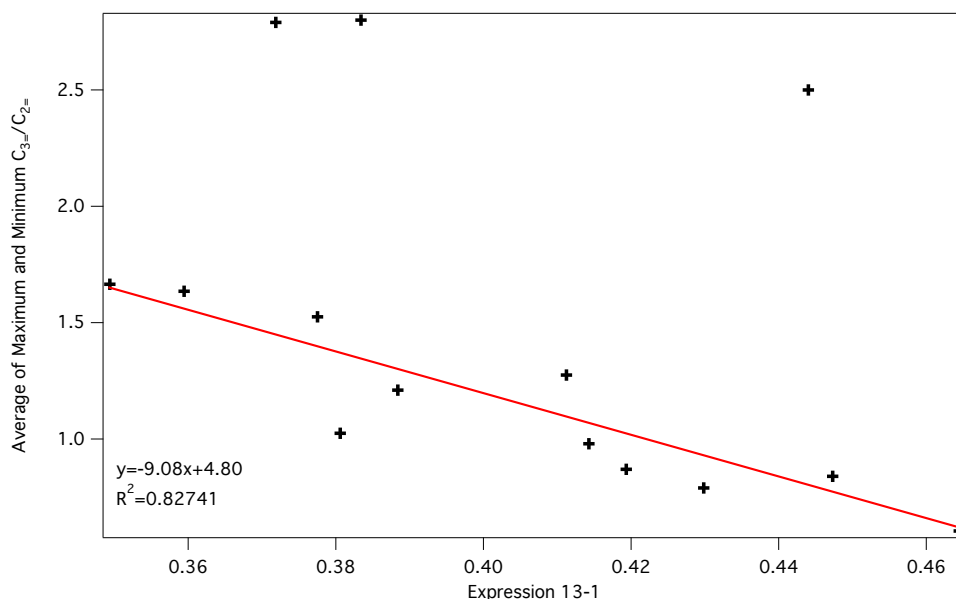


Figure 12-4: Best fit found for C_3/C_2 ratio against reaction and structure parameters

The most interesting point from this graph is that the trend is independent of the shape of the cavity. That is, the eccentricities, or the radii of the various cage structures studied would worsen this fit, and are probably not critical parameters. The key parameters turn out to be the reaction temperature, the number of acid sites in each cage, and the number of cages that these acid sites are shared between. The term for the number of T-atoms in the cage cancels with the definition of acid site concentration as used in this exercise, and thus it appears that the size of the cage is also immaterial based on this fit.

What these data also suggest, therefore, is that in order to increase the selectivity towards propylene, the number of acid sites in a single cage must be reduced, and the number of acid sites shared between multiple cages must be reduced. Further, this could be plausible because as the number of acid sites in a cage increases rapidly, the coking activity increases, and selectivities decrease. Further, as acid sites are shared between multiple cages, they can

generate more net acidic regions (as the proton can hop between the 4 oxygen atoms bound to the acidic aluminum) than when acid sites are solely dedicated to a single cage.

12.6 Conclusion

In conclusion, there was no consistent trend observed across all the materials that were studied. A large library of materials was tested for their activity in the MTO reaction. This chapter provides a summary of some of the more interesting materials tested, and the conditions under which these materials were tested.

A numerical analysis was conducted on all the aluminosilicate materials with 8-MR openings. The best fit data for this analysis showed that the eccentricities and radii of the cages did not affect the ratio of selectivities as much as the concentration of the acid sites did and the sharing of these acid sites between multiple cages did. In conclusion, in order to promote a higher $C_{3=}/C_{2=}$ ratio, a cage with very few acid sites per cage, and very few tetrahedral atoms shared with other similar cages must be generated.

12.7 Bibliography

- (1) Lee, G. S.; Zones, S. I. Zeolite SSZ-50, US Patent 6,605,267, **2003**.
- (2) Yokoi, T.; et al. *Angew. Chem. Int. Ed.* **2009**, 48, 9884–9887.
- (3) Wagner, P.; et al. *J Am Chem Soc* **2000**, 122, 263–273.

Chapter 13 Conclusions & future directions for structure effects on MTO reaction

13.1 Conclusions

This part of the thesis looked at the methanol to olefins reaction and how structures within the zeolite framework affect the product selectivity in the reaction. As a starting point, some of the frameworks known in the literature to perform this reaction were synthesized, characterized, and tested for their activity in the methanol-to-olefins reaction. Once it was confirmed that I was able to reproduce the data available in the literature, and that the reaction system setup was working as desired, several series of structures were synthesized to try to understand how certain aspects of zeolite structures can affect the product selectivity in the reaction.

It was noted that in order to promote selectivity towards light olefins, cavities with 8MR openings are desired. These cavities prevent the release of aromatic compounds as products but rather, trap them as reactive intermediates. In light of this, the effect of the cavity shape on product selectivity was investigated. The size and the eccentricity of the channel did not have a strong influence on the product selectivity. It was noted that the smaller the semi-minor radius of the ellipse formed by the cavity channel is, the higher the selectivity towards propylene. The eccentricity as a whole seemed to have an inconclusive effect on the product selectivities.

The product selectivity was greatly affected by the length of the cavity occluded behind 8-MR windows. As evidenced by the trend in product selectivity going from the LEV to CHA to AFX structures while maintaining other catalyst parameters constant, the $C_{2=}$ selectivity decreased with increasing cavity size, while the $C_{3=}$ selectivity had a maximum with the CHA structure.

Comparing product selectivities for the same structures but with varying compositions also proved inconclusive. Apart from one framework (AFX) it was noted that all the frameworks showed the trend of reducing the $C_{3=}/C_{2=}$ ratio with an increase in reaction temperature. The highest $C_{3=}/C_{2=}$ ratio observed was with the AFX structure at 450°C. The aluminosilicates in general gave a higher $C_{3=}/C_{2=}$ ratio than their corresponding silicoaluminophosphates. The only exception was the LEV structure, where the SAPO produced a higher $C_{3=}/C_{2=}$ ratio than the aluminosilicate.

Finally, a large number of readily accessible frameworks (detailed in chapter 13) were synthesized and tested for their activity in the MTO reaction. A key difficulty was in obtaining structures that had 8-MR openings while having a catalytically interesting acid site concentration. Only a small number of small pore zeolites can be synthesized with high Si/Al ratios that allow for meaningful catalytic testing for the MTO reaction. A variety of these were tested as part of this thesis work, and it was determined that the best structure across the board was the aluminosilicate CHA material with a Si/Al ratio of 13-15. This material can be run at various temperature conditions to achieve different maxima for ethylene and propylene selectivities. This material yields its highest $C_{3=}$ selectivity at 350°C, and highest $C_{2=}$ selectivity at 450°C.

13.2 Future Work

This thesis work on the methanol-to-olefins reaction provides a basis upon which further work can be done on particular areas in order to understand the chemistry of the reaction better so that catalysts with more desirable properties can be designed and made. As mentioned in the conclusion above, a large blanket survey of materials was conducted as part of this thesis work in order to obtain a library of materials whose reaction data are known.

As alluded to in the previous section in this chapter, a large number of 8-MR structures were tested as part of this thesis work. In order to explore the MTO reaction further, structures

with high Si/Al must be synthesized while still being small pores zeolites. This would provide insight into a potentially larger array of structures for the understanding of the activity of the MTO reaction. Further, this would allow for the exploration of the effects of other framework parameters on the product selectivity in the MTO reaction. One other possible area of understanding structure property relations is to understand the impact of the difference in the local catalyst surface on the reaction product selectivity. As seen in the early section of this thesis, for the same catalyst framework, SSZ-13 (a aluminosilicate) and SAPO-34 (a silicoaluminophosphate) have vastly different product selectivities. In order to be able to synthesize structures that yield a higher selectivity towards a particular light olefin, it is desirable to understand what causes these selectivities to differ.

One possible approach is to understand the kinetics of the individual alkylation and cracking steps involved. This is most conveniently done (due to the narrow 8-MR openings on most MTO catalysts) through the use of 1-D channel structures as proxies for the cavities that are present in the catalysts. However, a better approach would be to understand the interaction of these reactive intermediates with the actual structures used in the reaction, and to understand how the confinement or solvation effects would affect these intermediates and promote or hinder the MTO reaction.